University of Southampton

Faculty of Environmental and Life Sciences

Ocean and Earth Science

Thermohaline drivers of the Arctic Ocean circulation

by

Nicola Jane Brown

Thesis for the degree of Doctor of Philosophy

October 2019

University of Southampton

Abstract

Faculty of Environmental and Life Sciences
Ocean and Earth Science

Doctor of Philosophy

Thermohaline Drivers of the Arctic Ocean Circulation

by Nicola Jane Brown

The Arctic Ocean has a significant effect on global ocean circulation because it provides sources of both dense and light waters to the North Atlantic. The processes affecting formation of water masses within the Arctic, however, remain poorly understood because of the sparsity of measurements available for the region. Here, we use data derived from quasi-synoptic hydrographic observations across the main Arctic gateways to diagnose water mass transformations in the Arctic interior. We see a double overturning circulation in density space. The lower cell involves the densification of approximately 1.5 Sv of Atlantic Water (1 Sv $\equiv 10^6$ m^3 s^{-1}). This is accounted for by surface buoyancy fluxes driven by heat loss on the Barents Shelf, which we quantify using ERA-Interim reanalysis data. In the upper cell, a further 1.8 Sv of inflowing Atlantic Water experiences lightening through turbulent diapycnal mixing with fresher Arctic surface waters. Turbulent diapycnal diffusivities of order 10^{-5} m^2 s^{-1} are implied by the water mass transformations when averaged over the Arctic Basin. These are an order of magnitude larger than values documented by microstructure observations made around the Siberian shelf. However, observationally-based estimates of tidal energy conversion indicate the existence of highly-localised areas of enhanced turbulence. We find that sufficient energy is converted from the barotropic tide in these locations to account for the mixing inferred for the upper limb of the overturning.

We assess the effects on the fresh surface layer of increasing freshwater input, using simulations from a coupled ice-ocean general circulation model. We find that, to the lowest order, the response of ocean freshwater content is linear, with an adjustment timescale of approximately 10 years. However, the details of the ocean response are seen to depend on the source of freshwater input. The response to a change in precipitation is subject to greater complexity than that to increasing river runoff because of more complex interactions with sea ice. The results presented here suggest that future increases in Arctic Ocean freshwater input in the form of precipitation are more likely to be associated with variability in the storage and release of excess freshwater than are increases in freshwater input from river runoff.

Contents

List of Figures

List of Tables

Acknowledgements

The research described in this thesis has been funded by the Natural Environment Research Council through the SPITFIRE doctoral training partnership. I am grateful to my supervisors, Alberto Naveira Garabato and Sheldon Bacon, for their guidance, patience and inspiration over the course of the project. I am glad to acknowledge the support and encouragement of Johan Nilsson in the work described in Chapter 4. I thank Taka Tsubouchi for supplying the velocity estimates used in Chapter 2, Ben Lincoln for the microstructure data and Mattias Green for the tidal conversion estimates used in Chapter 3, and am grateful to Per Pemberton for running the GCM simulations used in Chapter 4. Chapter 2 benefited from helpful discussions with George Nurser. Alex Forryan, Jenny Mecking, Jeff Blundell and Clément Vic provided technical and computing advice, and I thank them for their assistance.

Chapter 1

Introduction

With a surface area of 9.5 million km^2, the Arctic Ocean is the smallest of the world's oceans. Nevertheless, although constituting only 2.6 % of the global ocean by area, and 1.0 % by volume (Jakobsson, 2002), it has a significant effect on global ocean circulation for several reasons. It acts both as a gateway for relatively fresh water to pass from the Pacific Ocean to the Atlantic Ocean and as a reservoir for storage and release of freshwater in response to variation in inflows and atmospheric conditions (Proshutinsky et al., 2009). It also provides dense waters, formed from heat loss and brine rejection on the continental shelves (Arthun et al., 2011), to supply deep convection in the Nordic and Labrador Seas (Yang et al., 2016). In addition, Arctic sea ice, with its high albedo, reflects incoming solar radiation in the summer, thus playing an important role in the global energy balance.

Despite its importance, however, the Arctic Ocean is still not well understood. The surface is poorly sampled compared to other regions (Cowtan and Way, 2014) because extensive ice cover hinders both physical access and visibility by satellite. Current understanding of Arctic Ocean circulation is derived mainly from limited coverage by ship-borne and mooring-based observations (e.g. Rudels and Friedrich (2000)), although measurements made using ice-tethered profilers (e.g. Timmermans et al. (2008); Zhao et al. (2014); Timmermans et al. (2014)) and gliders (Beszczynska-Möller et al., 2011) are increasingly available.

Because of extensive ice cover, which inhibits the transfer of momentum from wind to ocean, mixing rates in the Arctic Ocean are low compared to other regions and circulation is comparatively sluggish. The traditional picture of a quiescent ocean has been challenged by some (e.g. Rainville and Woodgate (2009)). Nevertheless, the Arctic Ocean is still characterised by stable stratification throughout much of the water column. At the temperatures prevalent in this region, variation in density is governed mainly by salinity. A core of relatively warm ($\sim$2 °C), salty ($\sim$35.0 psu) water of origin in the Atlantic Ocean occupies depths between around 200 m and 1000 m. This

Atlantic Water (AW) has entered the Arctic through the Fram Strait or across the Barents Sea (Aksenov et al., 2010). It is estimated that the AW layer contains sufficient heat to melt Arctic sea ice within four years (Turner, 2010; Rudels et al., 2004). However, across most of the region, a cooler, fresher surface layer overlies the AW core and this presents a barrier preventing heat from the AW layer from being mixed to the surface and coming into contact with the sea ice. Depths below the AW are occupied by cold ($\sim -1\,^{\circ}\mathrm{C}$), relatively saline (34.9 psu) deep water formed on the continental shelves by deep convection (Aksenov et al., 2010) or brine rejection from ice formation.

The main paths of Arctic circulation (see Figure 1.1) are believed to be a series of cyclonic boundary currents which are topographically steered around the edges of the continental shelves and along the ridges separating the ocean basins. Around 7 Sv of water enters from the North Atlantic through the Fram Strait as the West Spitsbergen Current and encounters the Yermak Plateau, an area characterised by enhanced tidal velocities which contribute to elevated rates of diapycnal mixing (Fer et al., 2015). Here, the West Spitsbergen Current splits (Bourke et al., 1988): perhaps half follows the Yermak Plateau northwestwards, before turning to the west and leaving through the Fram Strait once more, having given up some of its heat and salt through mixing on the Plateau. The remainder tracks across the Plateau closer to the north of

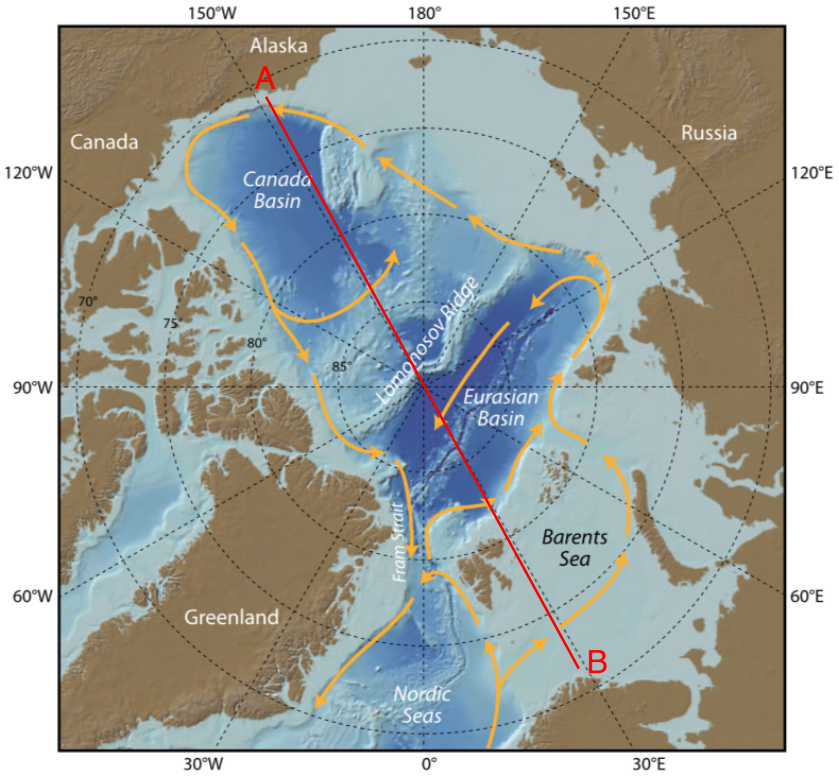

FIGURE 1.1: Schematic circulation of Atlantic Water within the Arctic Basin. (Figure reproduced from Spall (2013).) The red line AB marks the location of the section shown in Figure 1.2.

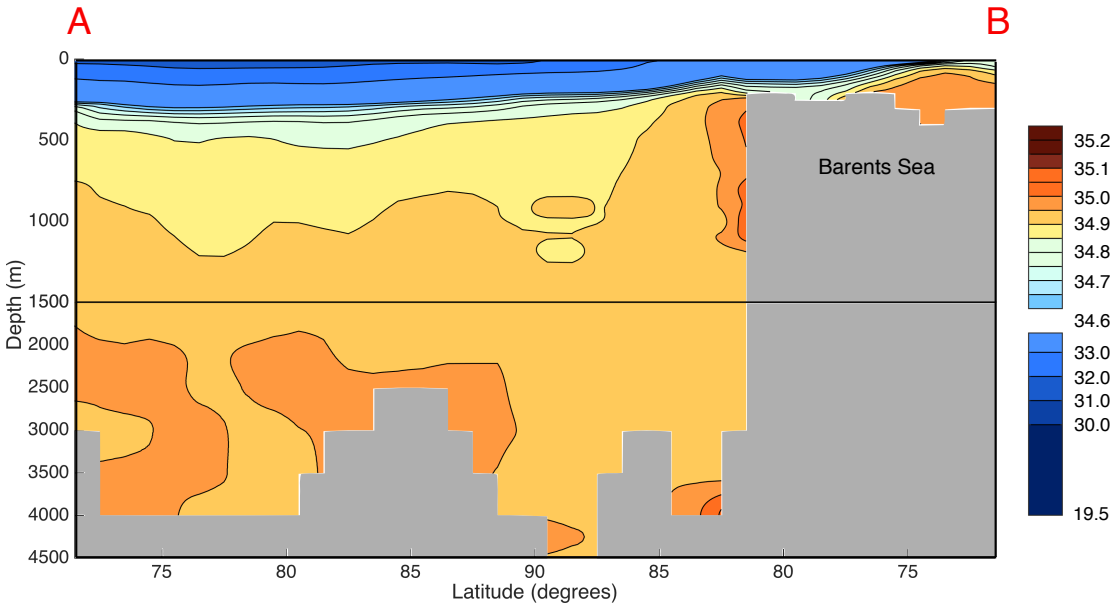

FIGURE 1.2: Summer salinity from the Polar Science Center Hydrographic Climatology 3.0 (Steele et al., 2001) along the section marked from A to B on Figure 1.1.

Svalbard to enter the Nansen Basin (von Appen et al., 2016). A further 1-3 Sv (varying seasonally) flows in through the Barents Sea. The signature of inflowing Atlantic Water is apparent in Figure 1.2, which shows salinity along the section from the north coast of Alaska to the north coast of Norway marked in red in Figure 1.1. Elevated salinities can be seen in the southern part of the Barents Sea, at the right of the figure, and along the shelf break just to the north. Modelling studies by Aksenov et al. (2010) and Aksenov et al. (2011) indicate that the Barents Sea branch either loses heat through surface cooling at shallow convective sites in the northern Barents Sea and is transported through the St. Anna Trough to become halocline water, or is transformed into bottom water through full-depth convection and mixing in the south-eastern Barents Sea. A substantial fraction of inflowing AW is transformed into less dense water: the Fram Strait branch encounters and melts sea ice, while some of the Barents Sea inflow remains on the shelf and absorbs runoff from the Siberian rivers before leaving the shelf at the Kara Sea (Rudels et al., 2004).

The currents of Atlantic origin are joined by 0.8 Sv of Pacific Water flowing in through the Bering Strait, this again being subject to significant seasonal variability (Woodgate et al., 2005). Around a third of this moves along the Beaufort Slope, exiting through the Canadian Archipelago. The path of the remainder is not well known; some may accumulate in the Beaufort Gyre, the rest transiting the Canada Basin before ultimately exiting through the Canadian Archipelago or Fram Strait. Overall, outflows from the Arctic Ocean comprise around 9 Sv through the west side of the Fram Strait (Fahrbach et al., 2001) and 1-2 Sv through the Canadian Archipelago. Ultimately, the

circulation of AW is thought to be driven by the salinity contrast between the AW and freshwater advected off the shelves: vertical mixing converts this to potential energy, which then drives the horizontal circulation (Spall, 2013).

The main sources of freshwater in the surface layer are illustrated in Figure 1.3. The largest is runoff from rivers around the continental margins of Siberia and North America, which is estimated to amount to $\sim$0.13 Sv ($1\,\mathrm{Sv} \equiv 10^6\,\mathrm{m^3 s^{-1}}$) (Haine et al., 2015). (There is uncertainty attached to this estimate, however, because a significant proportion of runoff comes from rivers which are ungauged.) Net precipitation contributes a further $\sim$0.06 Sv of freshwater (Haine et al., 2015). The inflow of Pacific Water through the Bering Strait also serves as a source of freshwater - $\sim$0.07 Sv - since its salinity is lower than that of Atlantic Water (Haine et al., 2015; Woodgate et al., 2005). Seasonal sea ice melt also contributes liquid freshwater to the surface layer and serves to strengthen stratification in summer (Randelhoff et al., 2017), and indeed in the Nansen Basin ice melt from sea ice advected into the area may be the main contributor of freshwater (Rudels, 2016).

Sources and sinks of freshwater are not typically in constant balance, and the proportion of freshwater input retained within the Arctic Ocean rather than being exported directly varies on timescales of O(1-10) years (Proshutinsky et al., 2009). This periodic storage and release has been linked to variation in circulation driven by cyclical changes in wind patterns both in the Beaufort Sea region and across the Siberian shelves (Polyakov et al., 2008; Morison et al., 2012; Haine et al., 2015). More generally, Johnson et al. (2018) find that the variability of Arctic freshwater content (FWC) in recent years can be explained chiefly by the influence of sea level pressure variations on sources, sinks and storage of freshwater. Proshutinsky et al. (2009) note that the range of variation of freshwater storage has increased since 2003 and suggest that it could continue to do so as climate change intensifies.

The net effect of the Arctic is to cool and freshen relatively warm, saline water flowing in via the Fram Strait or Barents Sea from the Atlantic (Rudels et al., 2013), before it returns southwards either through the Fram Strait or the Canadian Arctic Archipelago. This influence is clearly seen in Figure 1.4, taken from Tsubouchi et al. (2012), which contrasts the temperature and salinity characteristics of water flowing into the Arctic basin, in red, with those of water flowing out, in blue. Some water returns denser than it entered, some lighter, a two-fold influence that has been described as driving a double estuarine circulation (Stigebrandt, 1985; Carmack, 2007; Rudels, 2010; Eldevik and Nilsen, 2013; Lambert et al., 2016). Some authors, e.g. Pemberton et al. (2015), have used model studies to attempt to constrain the underlying temperature (T) and salinity (S) transformations, but **the existence and strength of the inferred double overturning have not so far been confirmed by any investigation benefiting from observationally-based evidence. Such an investigation is the first objective of this thesis**.

Although, as we have noted above, the Arctic Ocean is relatively quiescent, mixing in the ocean interior does play an important role in driving water mass transformations (Pemberton et al., 2015). Across much of the Arctic Basin, double diffusion is the dominant mechanism for mixing (Timmermans et al., 2008; Lenn et al., 2009), with rates of dissipation of turbulent kinetic energy (TKE) rarely seen to rise above $O(10^{-6})$ W m^{-3}. Elevated dissipation rates ($\sim 10^{-4}$ W m^{-3}), indicative of mechanical drivers, have, however, been observed over rough topography (Padman and Dillon, 1991; Rainville and Winsor, 2008; Fer et al., 2010; Lenn et al., 2011; Rippeth et al., 2015). TKE dissipation is also seen to vary temporally (Lenn et al., 2011; Guthrie et al., 2017). Nevertheless, the incidence of mechanical mixing is limited by sea ice cover, which inhibits the transfer of momentum from atmosphere to ocean (Rainville and Woodgate, 2009) and also leads to the dissipation of internal wave energy in the under-ice boundary layer (Guthrie et al., 2013), and by the fact that most of the Arctic basin lies to the north of the critical latitude above which internal tides are

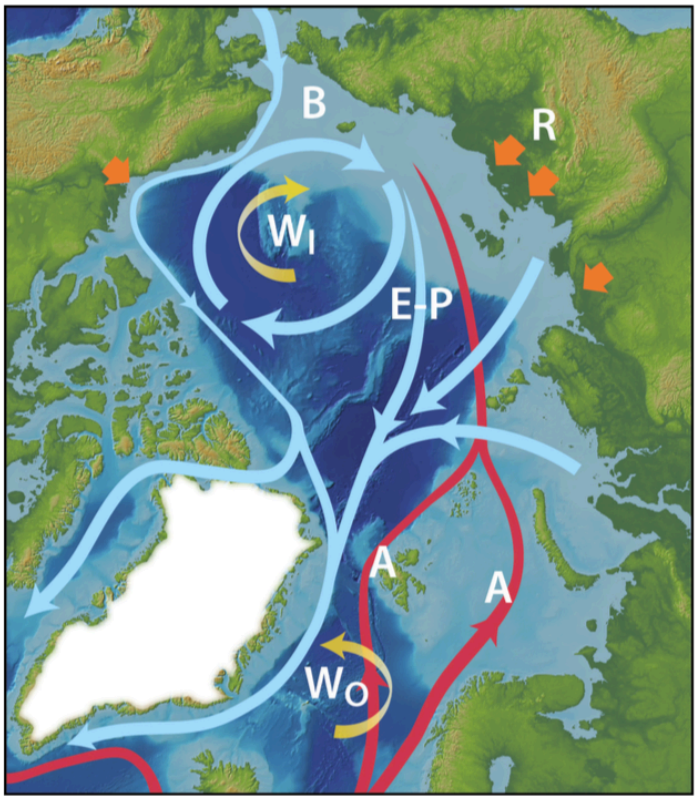

FIGURE 1.3: A schematic depicting the main circulation pathways of Arctic surface waters and sea ice drift (blue arrows) and key factors affecting them. The yellow arrows indicate winds within the Arctic region (W_I) and outside (W_O). Freshwater enters the Arctic Ocean as river runoff (R and short orange arrows), net precipitation (E-P) and inflow of relatively fresh Pacific Water (B). The red arrows labelled A show inflow of Atlantic Water. (Figure reproduced from Marshall et al. (2017).

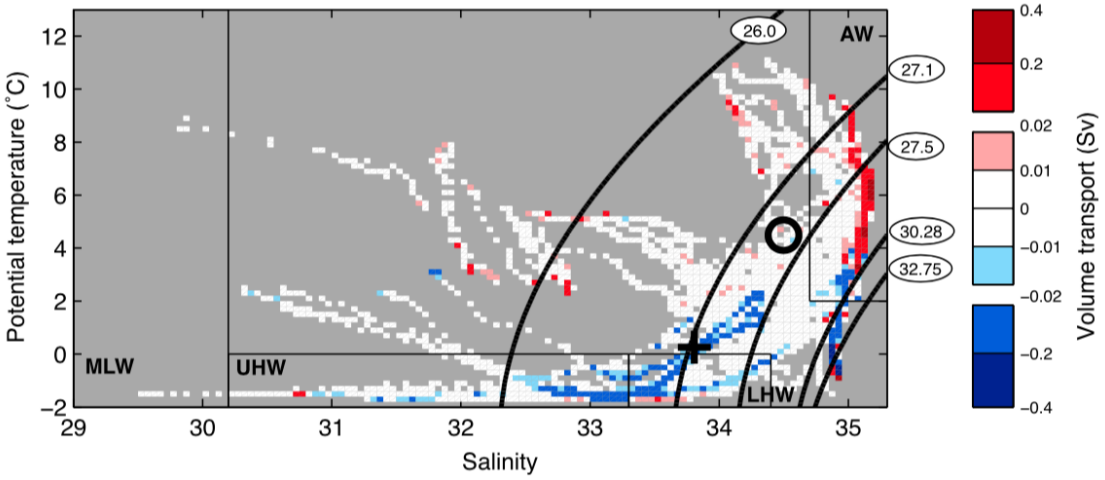

FIGURE 1.4: Volumetric θ-S plot of inflows to (red) and outflows from (blue) the Arctic Ocean, derived from ship-borne and mooring-based observations made over the period September 2004 to August 2005. (Figure reproduced from Tsubouchi et al. (2012).)

unable to propagate freely. Further discussion of our current understanding of the role of tidal energy in driving mixing is given in Chapter 3.

The strong downward trend in Arctic sea ice extent and area (Comiso, 2011), which is illustrated by Figure 1.5, has led to speculation (Giles et al., 2012) that upper ocean mixing might increase in the future as a greater proportion of the ocean surface comes into direct contact with the atmosphere. However, Guthrie et al. (2013) found no evidence of a trend in observations of internal wave energy and deep mixing in recent decades, a result they attribute to increased stratification due to increased liquid freshwater content enhancing the boundary layer dissipation of internal wave energy. Their conclusions were supported by Lincoln et al. (2016), who likewise found that stratification prevented the penetration of energy from wind-driven mixing in the Canada Basin to levels below the halocline.

The warming global climate is also driving increasing freshwater input to the Arctic Ocean (Vavrus et al., 2012; Bintanja and Selten, 2014). River runoff is projected to reach 5500 km^3 yr^{-1} and net precipitation 2500 km^3 yr^{-1} by 2100 (Haine et al., 2015), and increases in Pacific Water inflow are also expected. While the influence of wind patterns on freshwater storage has benefited from much recent investigation, the role of freshwater as a modifier of ocean circulation in its own right, rather than as a passive tracer of wind-driven currents, has received less attention. As Morison et al. (2012) observed, variation in the wind-driven Ekman pumping over the Beaufort Gyre region might be the main factor controlling the freshwater storage in the Gyre, but additional processes such as baroclinic eddies and mechanical ice-ocean feedbacks (Manucharyan and Spall, 2016; Meneghello et al., 2017; Dewey et al., 2018) influence the freshwater content of the Gyre. A steady state modelling study by Nummelin et al. (2016) showed

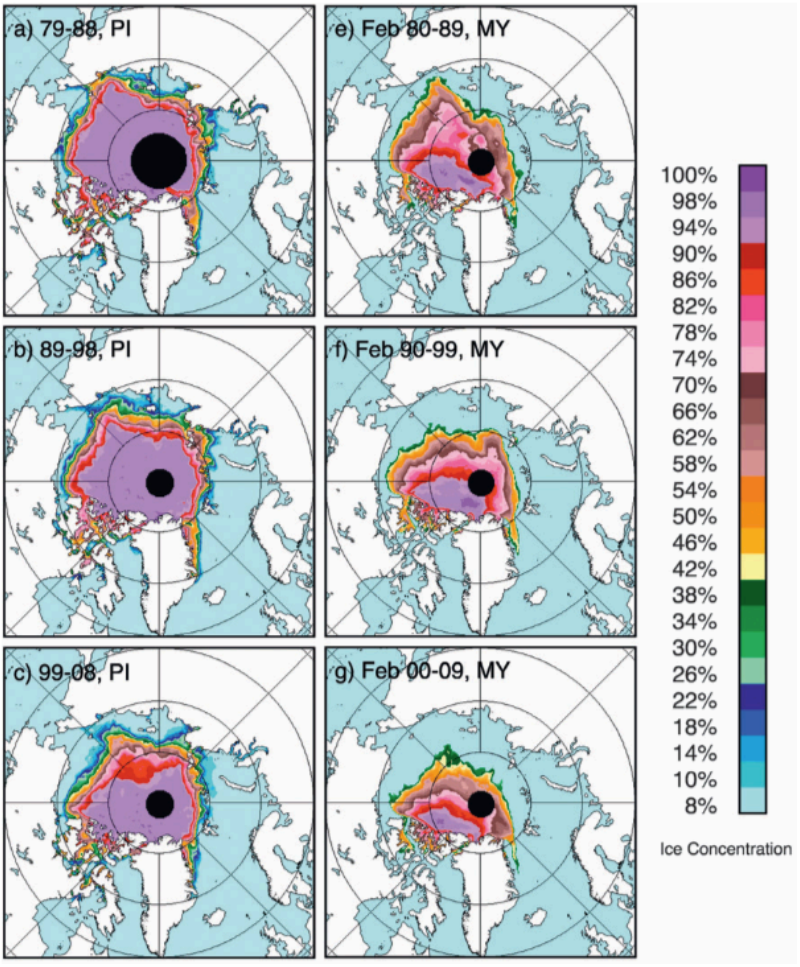

FIGURE 1.5: 10-year averages of, (a) to (c), perennial and, (e) to (g), multi-year ice cover from satellite data. (Figure reproduced from Comiso (2011).)

that increasing river runoff leads to strengthened stratification and spin up of the cyclonic circulation within the Arctic Ocean, while Pemberton and Nilsson (2016) found in similar model experiments that increased freshwater supply from runoff and precipitation results in a weakening of the Beaufort Gyre and a redirection of some freshwater export from the Canadian Arctic Archipelago (CAA) to the Fram Strait.

Given the link between ocean stratification and surface-driven mixing mentioned above, as well as the influence that increasing freshwater input appears to have on circulation patterns, there is a need for an improved understanding of the effect that enhanced freshwater input is likely to have on Arctic storage of freshwater and its release to the North Atlantic. **This leads us to address a further key question. What is the relationship between changing freshwater input to the ocean and the response of the ocean in terms of storage and export of freshwater?**

The remainder of this thesis is structured as follows. In Chapter 2 we investigate whether observational data support the existence of a double overturning circulation in

the Arctic Ocean. We quantify the respective contributions made by surface buoyancy fluxes and interior mixing in driving the circulation. In Chapter 3 we compare the implied mixing rates to previous direct observations of ocean turbulence and explore the plausibility of tidal energy conversion as a possible source of energy to support turbulent buoyancy fluxes at the levels estimated in Chapter 2. In Chapter 4, we consider the effect of changing freshwater input on Arctic Ocean stratification, using simulations from a numerical model to investigate the transient response of ocean freshwater content to changing freshwater input, and discuss what the simulations tell us about the processes underlying the ocean response. Finally, in Chapter 5 we summarise the findings of the research presented here, and consider their implications for future work.

Chapter 2

An Arctic Ocean Double Overturning

2.1 Introduction

As discussed in Chapter 1, previous studies (e.g. Stigebrandt (1985); Eldevik and Nilsen (2013)) have hinted at the existence of a double overturning in the Arctic Ocean. The transformations of inflowing Atlantic Water (AW) by heat loss to the atmosphere and freshwater (FW) input separately have been described by several authors (e.g. Mauritzen (1996) and Rudels et al. (1999)). Eldevik and Nilsen (2013) presented a theoretical framework to combine the two degrees of freedom, heat and salt, of the thermohaline circulation in the so-called Arctic Mediterranean – their domain included the Nordic Seas – in an attempt to assess its sensitivity to changes in surface heat and FW forcing. They found that the strength of AW inflow is related primarily to the heat budget, while the partition into dense outflow and surface outflow depends on the simultaneous change in the FW budget. In a similar analytical study aimed inter alia at defining a salinity of inflow water separating the surface and deep water components of the Arctic Ocean circulation, Rudels (2010) concluded that salinity at this point of bifurcation depends on the salinity and temperature of the AW at the point that it encounters sea ice.

No study has, however, so far confirmed or quantified the overturning in terms of diapycnal transformations. In this chapter we investigate whether observations support its existence. We make use of estimates of boundary volume and density fluxes derived from hydrographic observations and surface flux data from reanalyses to diagnose water mass transformations and hence diapycnal mixing rates within the Arctic basin. We thus aim to provide, for the first time, an integrated view of the surface and interior drivers of the diapycnal circulation. In summary, the objectives of this chapter are to confirm the existence of a double overturning in the Arctic Ocean and to assess

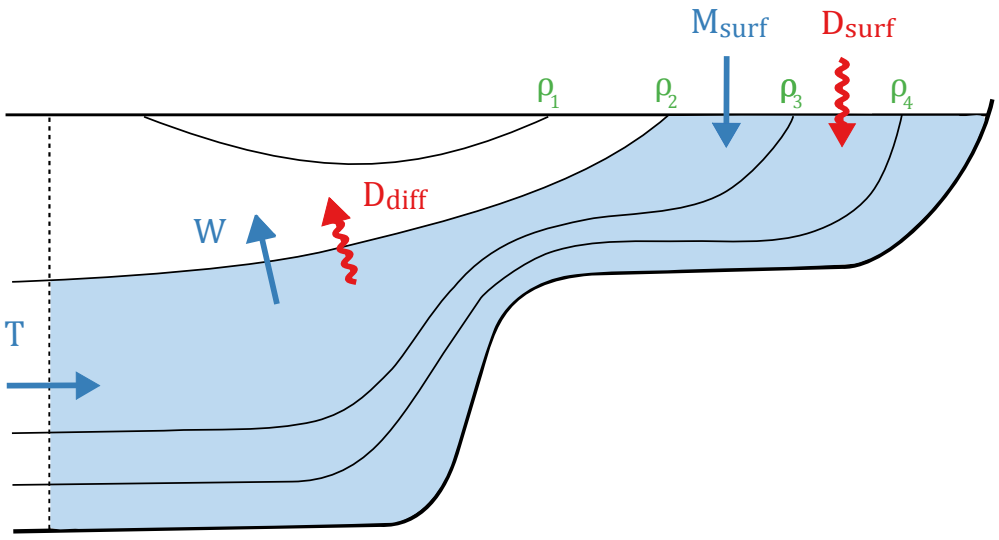

FIGURE 2.1: Schematic illustration of the box model. Thin black lines represent isopycnals, blue arrows advective volume fluxes and red arrows diffusive fluxes of density.

the relative importance of surface buoyancy fluxes and interior mixing as drivers for the overturning.

2.2 Methods and data

2.2.1 Box model

The semi-enclosed nature of the Arctic Ocean, bounded as it is around most of its circumference by land, lends itself to a control volume approach in which we may use knowledge of the ocean state at its boundary to infer its state in the interior. We adopt an approach similar to that described by Huussen et al. (2012). A simple box model is constructed, as shown in Figure 2.1, to represent the Arctic Ocean. The model incorporates 31 layers defined by potential density (listed in Table 2.1). Its vertical boundaries comprise the four major gateways to the Arctic Ocean: the Davis, Fram and Bering Straits and the Barents Sea Opening, shown in Figure 2.2 and described in more detail in Tsubouchi et al. (2012), and their surrounding land masses.

Consider the volume budget for a layer bounded at its upper surface by a defined isopycnal and at its lower surface by the seafloor, as signified by the shaded region in Figure 2.1. By continuity, the advective volume flux, W, through the upper bounding isopycnal is given by:

$$W = T + M_{surf} \tag{2.1}$$

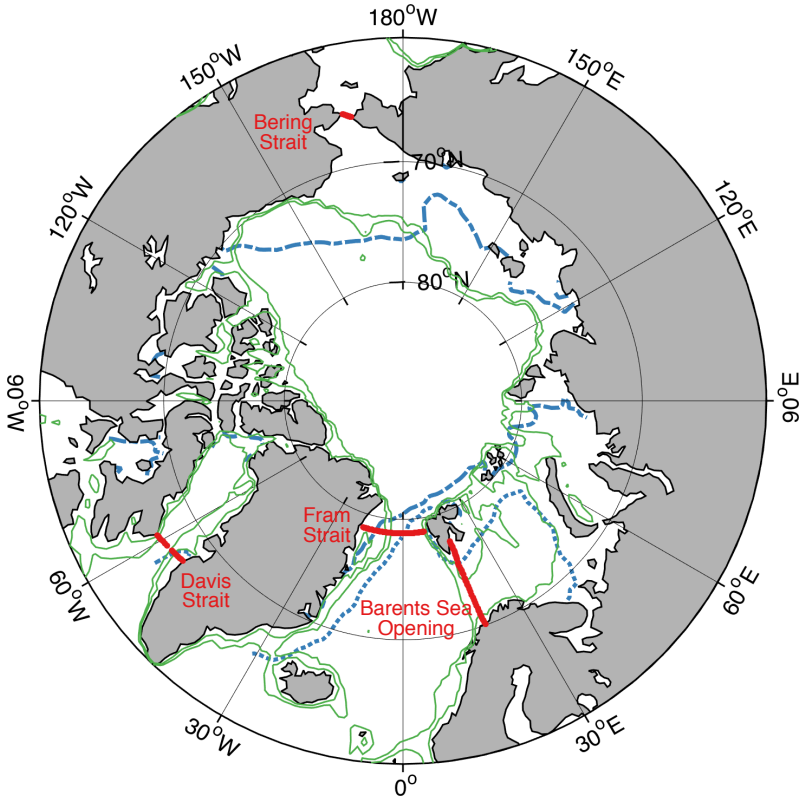

FIGURE 2.2: Map of the model domain showing, in red, the locations of the bounding straits. The 200 m and 500 m depth contours are shown in green. The dashed and dotted blue lines show mean sea ice extent (defined as the limit of 15% ice cover) taken from ERA-Interim for the months of September 2004 and April 2005 respectively.

where T is the volume flux into the layer through the side boundary and M_{surf} is the net surface volume flux from input of freshwater. The sign convention that we adopt throughout is that flows into the box at the side boundary and surface are positive, and diapycnal flows from denser to less dense water are positive.

Diapycnal volume fluxes in the interior may thus be diagnosed layer by layer from estimates of boundary and surface fluxes. T is calculated from a gridded velocity field derived from observations and described in Section 2.2.3:

$$T = \iint v \, \mathrm{d}x \, \mathrm{d}z \tag{2.2}$$

where v is velocity normal to the boundary, x is horizontal distance along the boundary and z is depth. For M_{surf} we take the annual mean of reanalysis fluxes and river runoff estimates, described in Section 2.2.4, integrated month by month over the outcropping area of each density layer.

Note that in omitting a mass storage term from Equation 2.1 we are assuming steady state. In reality, mass storage does occur on the timescales over which the hydrographic observations underlying the boundary velocity estimates were collected.

TABLE 2.1: Definition of model layers by potential density (σ_0) of upper interface.

Layer	**Upper interface**	**Mean depth of interface(m)**	**Layer group**[1]
1	Surface		Surface Water
2	24.700	20	
3	25.100	27	
4	25.500	37	
5	26.000	53	Subsurface Water
6	26.400	71	
7	26.700	83	
8	26.900	93	
9	27.000	98	
10	27.100	106	Upper Atlantic Water
11	27.300	121	
12	27.500	145	Atlantic Water
13	27.550	153	
14	27.580	158	
15	27.600	161	
16	27.700	196	
17	27.800	194	
18	27.840	213	
19	27.880	239	
20	27.900	259	
21	27.921	284	Intermediate Water
22	27.948	337	
23	27.962	382	Deep Water
24	27.986	493	
25	28.010	630	
26	28.037	863	
27	28.050	1067	
28	28.060	1262	
29	28.070	1490	
30	28.076	1580	
31	28.087	1958	

[1] Layer groupings as given by Tsubouchi et al. (2012)

This will give rise to errors in the diapycnal fluxes calculated using Equation 2.1, but insufficient numbers of observations exist to allow us to quantify them.

2.2.2 Advection-diffusion balance

We seek next to understand the respective contributions made by surface buoyancy forcing and interior mixing as drivers of the Arctic overturning. Taking as our starting point the assumption that, averaged over the course of the year, advective fluxes of density are balanced by buoyancy fluxes at the surface and turbulent diffusion of density in the interior, we use the formulation of Walin (1982) as adapted for density transformations by Large and Nurser (2001) to calculate density budgets for each isopycnal layer and thus to infer the diapycnal mixing rates needed to maintain the Arctic stratification. Again assuming stationarity, the density budget for the layer is given by:

$$D_{diff(\rho)} = \overline{\rho}_{bdy} T - \rho W_{(\rho)} + \rho_{surf} M_{surf} + D_{surf} + \text{interior sources} \tag{2.3}$$

where $D_{diff(\rho)}$ is the diffusive flux of density through the upper surface of a layer defined by potential density ρ, $\overline{\rho}_{bdy}$ the transport-weighted mean density on the side boundary of the layer, ρ_{surf} the mean sea surface density weighted by surface freshwater input across the outcropping area of the layer and D_{surf} the net diffusive surface flux of density. Once again, fluxes of density into a layer at the boundary and surface, and upward through isopycnals, are positive. Interior sources of density such as that caused by nonlinearities in the equation of state are expected to be of secondary importance in high-latitude dense water production regions (Isachsen et al., 2007): we do not therefore include them in the calculations here, but discuss their potential significance in Section 2.4 below.

The diffusive flux of density may be expressed as a basin-mean diffusivity, K:

$$K_{(\rho)} = \frac{-D_{diff(\rho)}}{A \frac{\partial \rho}{\partial z}} \tag{2.4}$$

with A as the surface area of the respective isopycnal surface forming the layer boundary and $\frac{\partial \rho}{\partial z}$ the mean gradient of density across the surface.

2.2.3 Boundary fluxes

The boundary velocities used in the calculation of boundary volume and density fluxes are the velocity estimates presented by Tsubouchi et al. (2012), which they derive using an inverse model from quasi-synoptic observations made across the four main gateways to the Arctic Ocean: the Bering, Davis and Fram Straits and the Barents Sea Opening. The utility of the dataset has been demonstrated in a number of previous studies (MacGilchrist et al., 2014; Torres-Valdes et al., 2013, 2016; Tsubouchi et al., 2018). Measurements were collected by ship-borne and mooring-based CTD instruments over the period 9 August to 10 September 2005. To fill in short distances across the Barents

Sea Opening where observational data were not available, these were supplemented with output from a high-resolution coupled ice-ocean general circulation model, NEMO. The model was formulated with 15 layers defined by isopycnal surfaces, and constrained to conserve volume and salinity anomaly in each of the layers and across the full model depth. The velocities calculated from the model for each of the 15 layers have been interpolated onto a 10 dBar vertical grid using the Akima method.

A notable difference between the inverse model used to derive the velocity estimates and the box model adopted in the current study is the treatment of surface volume fluxes. The inverse model assumed that these applied only to the uppermost layer, and calculated them as an output by constraining the model to conserve salinity anomaly. In contrast, because we are concerned here with the quantification of the effect of surface buoyancy forcing on all outcropping density layers, we have instead used the estimates of surface volume fluxes described in Section 2.2.4 in the conservation equations. Nevertheless, as we discuss further in Section 2.3.2, because the surface input of freshwater is confined largely to the shelf areas, the inconsistency between data for boundary and surface volume fluxes is expected only to affect the volume budgets for the uppermost layers.

A further source of potential uncertainty relates to the extent to which the volume conservation constraint on the inverse model continues to apply to the resulting velocity estimates once interpolated onto the pressure grid. Cumulative volume transport around the boundary calculated from the pressure-gridded velocities is quantified by Tsubouchi (2016, personal communication) to be -16.3 mSv, and by the current author to be 23.3 mSv (the difference potentially relating to different treatment of bottom triangles).

For the current study we apply an adjustment to the gridded velocities to take account of the surface fluxes used here and the discrepancies in transports described above, such that cumulative full-depth volume transport is reduced to zero. The resulting velocity field and cumulative transports are shown in Figure 2.3. We lack a means of identifying where around the domain boundary the discrepancies arise, and thus have applied a uniform barotropic adjustment of 1.5×10^{-4} m s^{-1} to all velocities. The effect of this is discussed in Section 2.3.1.

2.2.4 Surface buoyancy fluxes

For estimates of surface fluxes of heat and for evaporation and precipitation, we use the ERA-Interim reanalysis product provided by the European Centre for Medium-Range Weather Forecasts (ECMWF), one of three reanalysis products identified by Lindsay et al. (2014) as being most consistent with independent observations (the others being the Modern-Era Retrospective Analysis for Research

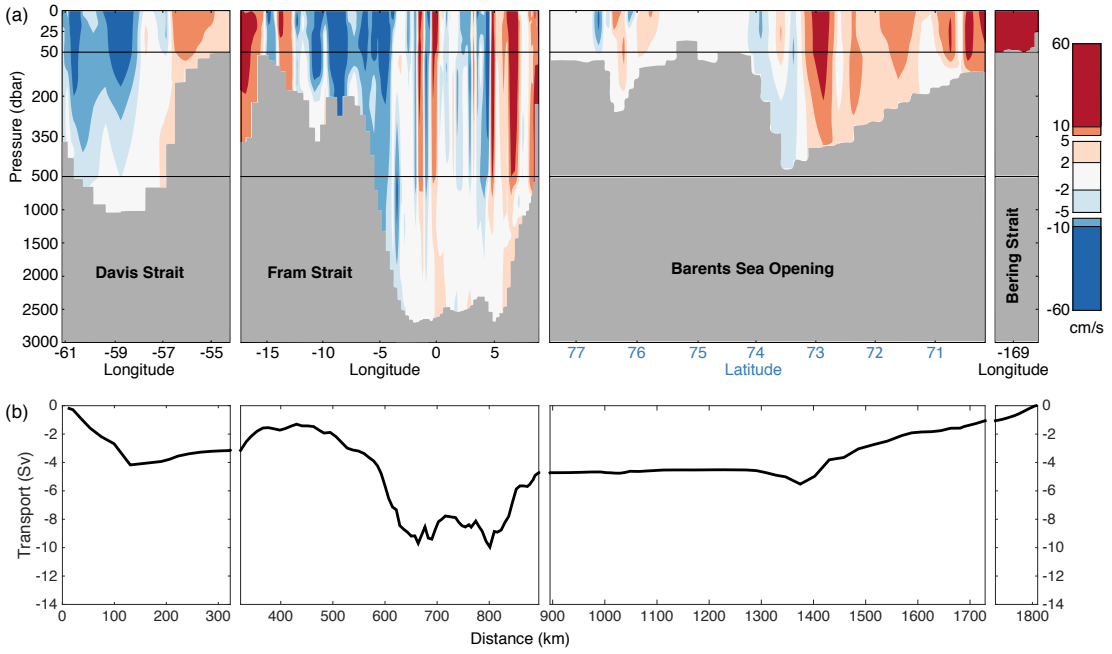

FIGURE 2.3: (a) Boundary velocities adjusted to conserve volume. Red colouring represents flow into the Arctic Ocean, and blue outward flow. (b) Cumulative full-depth volume transports around the boundary. Figure based on Tsubouchi et al. (2012) Figure 9.

and Applications (MERRA) dataset from NASA and the Climate Forecast System Reanalysis (CFSR)). Monthly average fields for surface net solar radiation, surface net thermal radiation, surface latent heat flux and surface sensible heat flux at 1.0° resolution are summed to obtain estimates of total heat flux per unit area. Monthly fields for evaporation (E) and total precipitation (P) are combined to give the P-E component of freshwater flux. In each case fluxes are scaled by the ERA-Interim field for proportion of ice-free water, although it is acknowledged that this might lead to some under-counting of freshwater input to the upper layers if precipitation that is not included in the flux estimates because it falls over ice-covered ocean subsequently thaws and enters the ocean during the late summer melt period.

For the principal calculations we use data relating to the months from September 2004 to August 2005, that is, the year leading up to the period in which the boundary observations used for the derivation of the velocity estimates were made. To test the effect of inter-annual variability in heat fluxes, the calculations are repeated with data for the previous year, September 2003 to August 2004. A further sensitivity test is conducted using MERRA reanalysis data in place of ERA-Interim 2004-05 data, although we concede that the two data sets are not completely independent since in many cases they are based on the assimilation of the same observations.

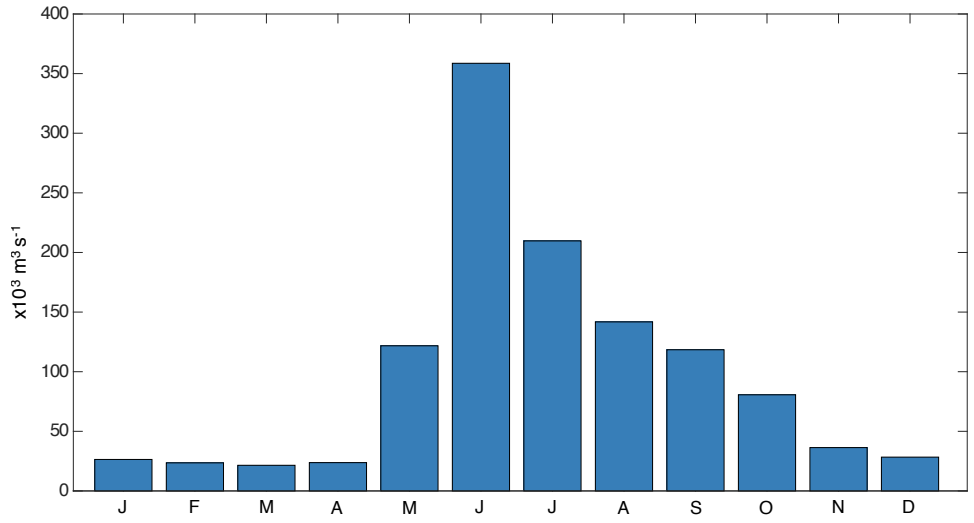

FIGURE 2.4: Total (gauged + ungauged) river runoff volume flux from the AOMIP forcing dataset.

To complete our calculation of surface freshwater fluxes, we do not use the runoff data offered by either of the reanalysis datasets, preferring the river-runoff forcing dataset provided by the Arctic Ocean Model Intercomparison Project (AOMIP) which appears to offer a more realistic representation of runoff from the main Siberian rivers. Specifically, we use the monthly total (gauged and ungauged) runoff figures from the climatology. Figure 2.4 shows total runoff fluxes: their strong seasonal cycle is readily apparent. We assume that outflow from the rivers is distributed by advection across the continental shelves (defined as having water depth less than 400m) adjacent to the mouths of the major Arctic rivers. In our model we distribute the total monthly average fluxes from AOMIP evenly by area only to those surface grid cells on the Canadian shelf west of 120°W and the Siberian shelf east of Novaya Zemlya.

Using a form of the formulation adopted by Jullion et al. (2010) (modified slightly to perform the integration across a density layer in place of a density interval centred on density ρ), the diffusive surface flux of density, D_{surf}, included in Equation 2.3 is then given by

$$D_{surf}(\rho) = \frac{1}{12} \sum_{months} \int_{A_{surf}} \left(\frac{\alpha H}{C_p} - \rho \beta Q S \right) \mathrm{d}A \tag{2.5}$$

where $A_{surf}(\rho)$ is the outcropping area of the density layer below isopycnal ρ; $\alpha(T, S)$ is the thermal expansion coefficient for seawater; $H(x, y, t)$ is the air-sea net heat flux per unit area (+ve into the ocean); $C_p(T, S)$ is the specific heat capacity of seawater; $\beta(T, S)$ is the haline contraction coefficient for seawater; $Q(x, y, t)$ is the surface freshwater flux per unit area (+ve into the ocean) arising from net precipitation and runoff from rivers; and $S(x, y, t)$ is surface salinity.

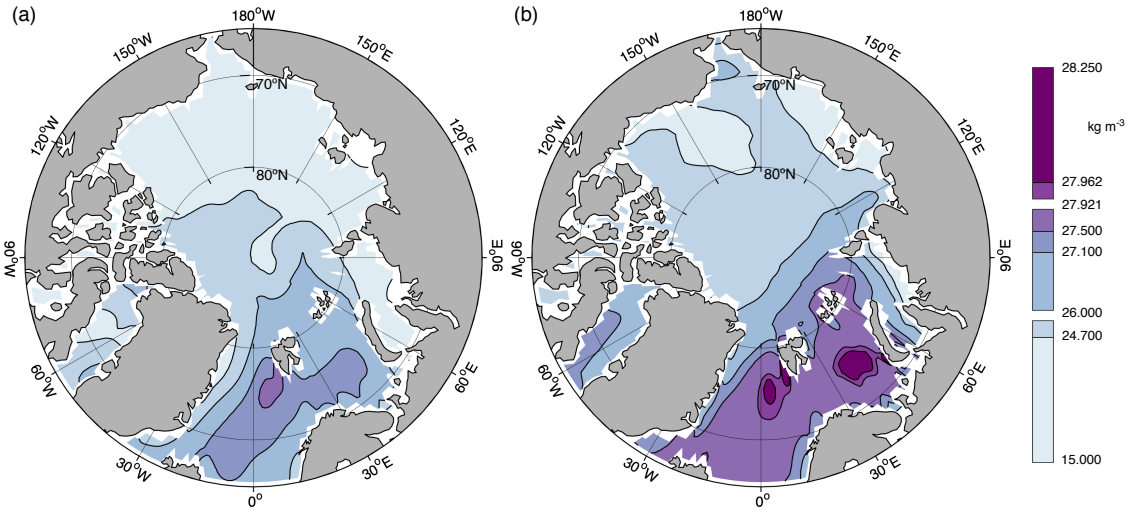

FIGURE 2.5: Sea surface densities calculated from PHC 3.0 temperature and salinity fields for (a) September and (b) March.

2.2.5 Climatological densities

The monthly sea surface densities used to define the areas of integration of surface fluxes in Equation 2.5 are calculated from the monthly temperature and salinity fields of the Polar Science Center Hydrographic Climatology (PHC) v. 3.0 (updated from Steele et al. (2001)), which combines the 1998 version of the World Ocean Atlas with the regional Arctic Ocean Atlas. Surface densities for summer (September) and winter (March) are shown in Figure 2.5. PHC data are available only at 1.0° resolution. Consequently, some areas up to a distance of approximately 110 km from the coast are excluded from the integration by the unavailability of density data. As can be seen from Figure 2.5, however, with the exception of coastal waters to the north and west of Svalbard and around Franz Josef Land, these are limited to regions where only the surface water classes outcrop.

Monthly PHC 3.0 fields are available only for depths down to 1500 m. For the calculation of the areas of isopycnal surfaces and density gradients required for Equation 2.4, therefore, we use summer (July, August, September) seasonal mean fields of temperature and salinity, which span the full basin depth to 5500 m.

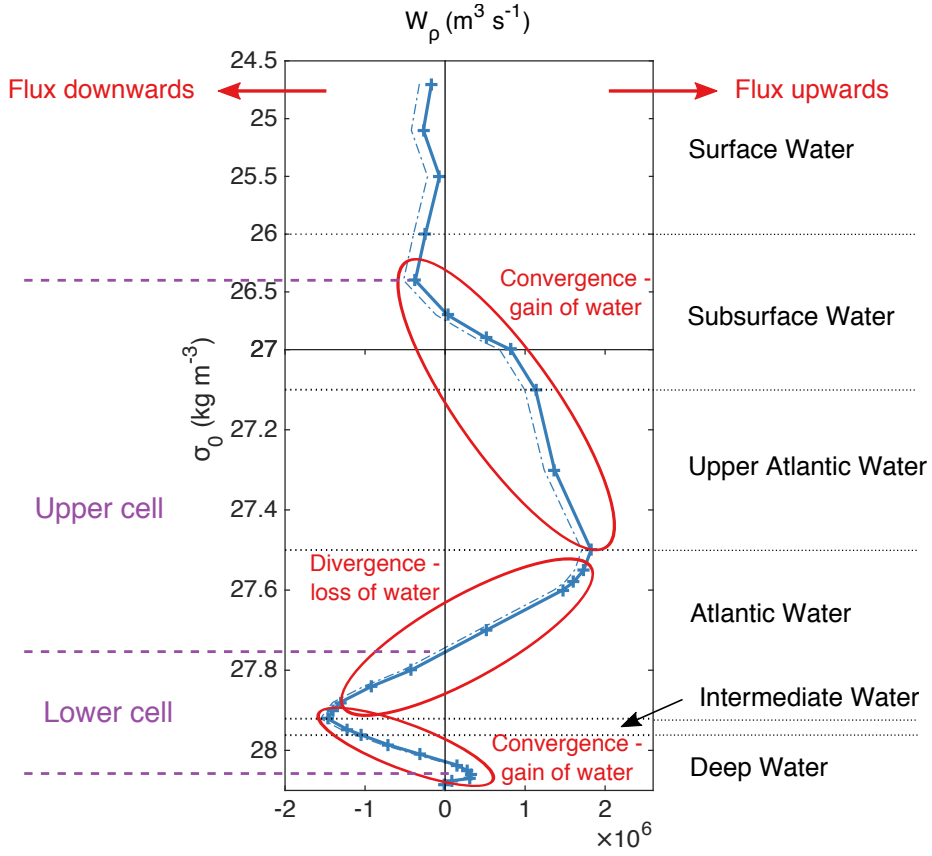

FIGURE 2.6: Diapycnal volume transports across each isopycnal layer boundary. Positive values indicate transports from denser to less dense layers. The solid blue line shows transports calculated from corrected velocities and the dashed line results using uncorrected velocities. (Note the change in density scale between the upper and lower sections of the figure.)

2.3 Results

2.3.1 Overturning quantified from volume budgets

Diapycnal volume transports, W, calculated according to Equation 2.1 are shown in Figure 2.6. Positive values indicate transports from denser to less dense layers. Basin-wide transports are of the order of 1 Sv. At densities between $\sigma_0 = 27.500$ kg m^{-3} and 27.921 kg m^{-3} diapycnal transports are divergent, indicating that net transports into the basin at the boundary are positive, and water is lost from these water classes in the interior. The strongest upward transport, 1.8 Sv, occurs across the $\sigma_0 = 27.500$ kg m^{-3} isopycnal, which represents the boundary between Atlantic Water and Upper Atlantic Water, and the strongest downward transport, 1.5 Sv, across the 27.921 kg m^{-3} isopycnal marking the base of the Atlantic Water layer. Above the Atlantic Water layer, between the 26.400 kg m^{-3} and 27.500 kg m^{-3} isopycnals, transports are convergent. Water is formed in these classes and there is net export from the Arctic. The same is true between the 27.921 kg m^{-3} and 28.060 kg m^{-3}

isopycnals, that is, for water in the Intermediate and upper Deep Water classes. In other words, the inflowing Atlantic Water mass is split and portions transformed into both lighter and denser water, confirming the existence of an overturning circulation with both an upper and a lower cell. The potential density at which the bifurcation occurs is 27.75 kg m^{-3}. In the Surface Water and lighter Subsurface Water classes, transports are small and no significant net import or export is seen. There is a small (~ 0.3 Sv) net import of the densest water, which probably enters the Arctic Basin from the dense water formation region in the Nordic Seas just beyond the Fram Strait.

Figure 2.6 also shows, in the fine, dashed, blue line, volume transports calculated without making the adjustment to boundary velocities to ensure conservation of volume described in Section 2.2.3. These values give an indication of the uncertainty in the results due to errors in the boundary data introduced by the regridding process. In surface waters, the difference between transports calculated from adjusted and unadjusted velocities is 0.15 Sv, which is of the same order as the transports themselves. Of greater interest, since we seek to quantify the strength of the Arctic overturning, are the differences at the upper and lower surfaces of the Atlantic Water layer, which are 0.1 Sv or 6% in each case.

A further sensitivity test was run to determine the effect of using surface volume fluxes calculated from the inverse model, as described in Section 2.2.3, rather than those derived from reanalysis data. The results of this test are not shown in Figure 2.6 because they are visually nearly indistinguishable from the transports already described. As expected, only the layers closest to the surface are affected. The transport across the 24.700 kg m^{-3} isopycnal is 0.015 Sv, or 9%, smaller when calculated using reanalysis surface fluxes. At the upper surface of the Atlantic Water layer the difference is only 0.006%.

2.3.2 Surface buoyancy fluxes driven by heat and freshwater exchanges

Figure 2.7 shows annual mean surface buoyancy fluxes for the period September 2004 to August 2005, calculated as described in Section 2.2.4. Fluxes due to heat and freshwater are shown separately. As expected, densification due to heat loss is concentrated in the south-western section of the Barents Sea where warm, inflowing Atlantic Water is present at the surface. Note that the region of maximum heat loss is not quite coincident with the area of highest March sea surface density (see Figure 2.5(b)), probably because water in that area has already lost heat during its passage across the Barents Sea, reducing the temperature differential between ocean and atmosphere, and because heat loss in that area is inhibited by winter sea ice cover (Figure 2.2). Annual mean buoyancy gain due to warming is limited to small areas

north of the Bering Strait, at the southern end of Novaya Zemlya and in the north west of Baffin Bay.

Buoyancy gain due to net freshwater input largely reflects the distribution adopted for river runoff on the Siberian shelves and offshore of the Mackenzie River outflow. We note, however, a region of reduced freshening along the Siberian coast which follows the line of summer sea ice extent and is presumably subject to enhanced evaporation in summer. Although the Barents Sea generally receives relatively high levels of precipitation, this is not apparent in these results.

Variation of surface buoyancy flux with ocean density is shown in Figure 2.8, where the seasonal cycle is apparent in contributions due both to heat and to freshwater flux. In September 2004, heat loss affects only Surface and Subsurface Waters, but as the winter progresses heat is lost and density gained in increasingly dense layers as they begin to outcrop. The densest waters, with density anomaly of approximately 28.0 kg m^{-3}, are exposed and undergo density gain in March 2005. From January until the end of winter, the Surface and Subsurface Water classes experience very limited surface fluxes because they are ice-covered. From May through the remainder of the summer, heat is gained by the ocean and density lost, with the waters in contact with the atmosphere becoming progressively less dense. Averaged over the year, the bulk of the effect of surface heat fluxes is a densening of Atlantic Water, with some densification also affecting Upper Atlantic Water.

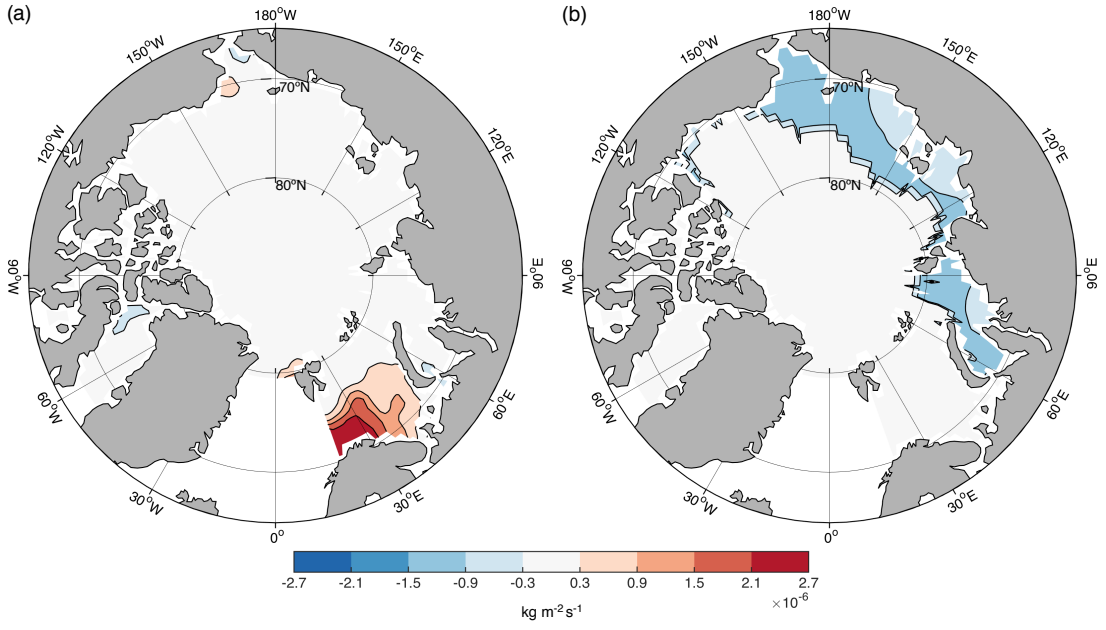

FIGURE 2.7: Annual mean buoyancy flux per unit area due to (a) net heat flux and (b) net freshwater flux. Positive values indicate addition of density to the ocean.

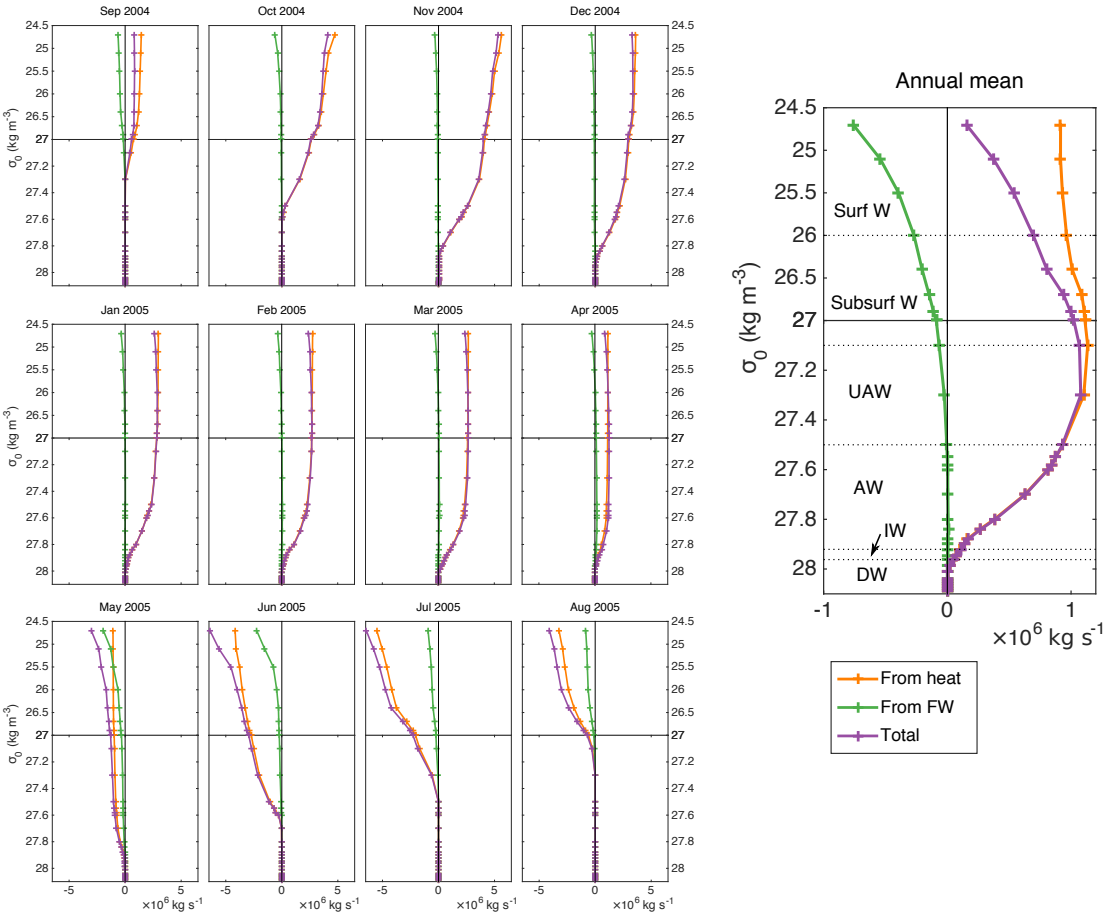

FIGURE 2.8: Monthly mean and annual area-integrated surface buoyancy fluxes, D_{surf}, for each isopycnal layer due to surface heat and freshwater fluxes.

The effect of freshwater flux is most apparent in May and June, when spring melting causes a strong increase in rates of river runoff. This is slightly earlier than the peak in runoff shown in Figure 2.4 because later in the summer the sea surface has freshened and a higher proportion of runoff enters water less dense than the lightest layer shown here. Monthly mean surface fluxes due to freshwater are consistently smaller in magnitude than those due to heat flux for all layers apart from the lightest surface water, but because their effect is almost always to add buoyancy to the ocean, averaged over the year they give rise to buoyancy fluxes of the same order of magnitude as those produced by heat flux in the Surface Water layer. For Atlantic and Upper Atlantic Water, however, the effect of freshwater fluxes is negligible.

Sensitivity of surface buoyancy fluxes to the choice of reanalysis data set is shown in Figure 2.9. The results described above are compared to those produced by repeating the buoyancy flux calculation using data from the same reanalysis product but a year earlier, and using a different reanalysis product, MERRA, for the same year. As

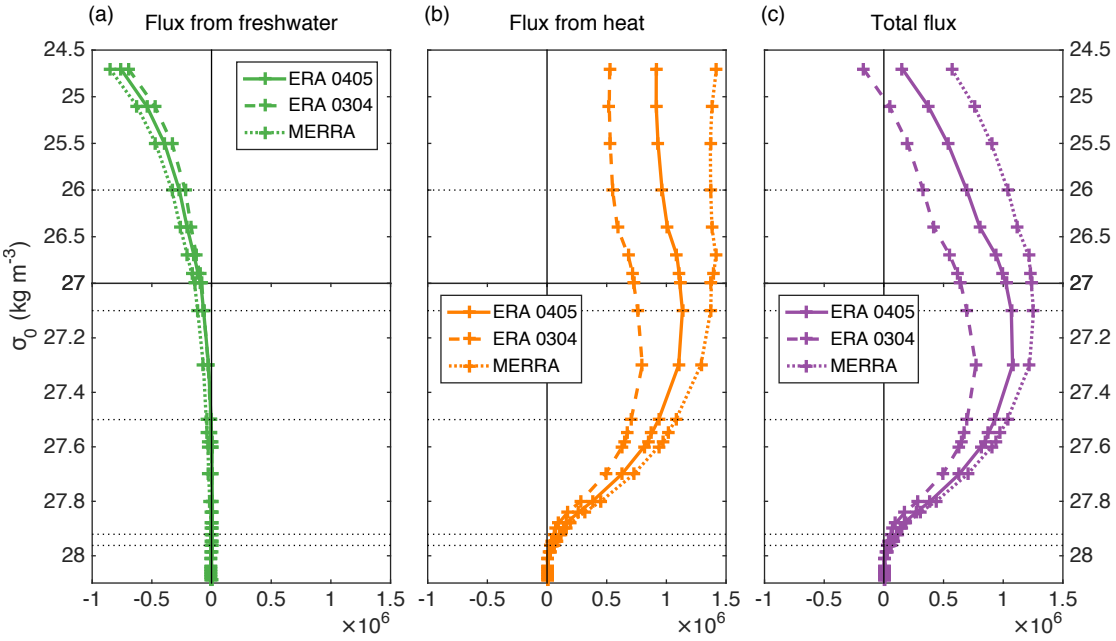

FIGURE 2.9: Comparison of surface buoyancy fluxes in kg s^{-1} calculated using ERA-Interim reanalysis data for the years September 2004 to August 2005 (solid line) and September 2003 to August 2004 (dashed line), and MERRA reanalysis data for the year September 2004 to August 2005 (dotted line).

expected, results for fluxes due to freshwater are changed only slightly, since only a small proportion of the freshwater input driving the buoyancy fluxes comes from net precipitation. Choice of data set has a greater impact on the calculation of density gain due to heat loss. Use of MERRA data in place of ERA-Interim results in a basin-wide buoyancy gain of 1.0 $\times$ 10^5 kg s^{-1} or 11% greater for the layer capped by the upper surface of Atlantic Water, and 1.9 $\times$ 10^5 kg s^{-1} or 18% greater for the layer which also includes Upper Atlantic Water. Use of ERA-Interim data for the year 2003 - 2004 rather than 2004 - 2005 leads to calculated buoyancy fluxes 2.3 $\times$ 10^5 kg s^{-1} or 25% smaller for the integration to the upper surface of Atlantic Water, and 3.7 $\times$ 10^5 kg s^{-1} or 35% smaller when Upper Atlantic Water is included.

2.3.3 Diffusive density fluxes implied by density budgets

A comparison of the cumulative fluxes calculated separately from boundary and surface data is given in Figure 2.10b. The blue results are the net advective density fluxes into each cumulative layer calculated from boundary flux data. The purple line shows the integrated surface fluxes calculated from ERA-Interim 2004-05 data and shown in Figure 2.9 (i.e. D_{surf} in Equation 2.3). The red values represent the residual diffusive fluxes required to maintain a balanced density budget when the two are combined.

With the exception of the very lightest surface layers - where seasonal changes in temperature and salinity can be expected to render the assumption of stationarity

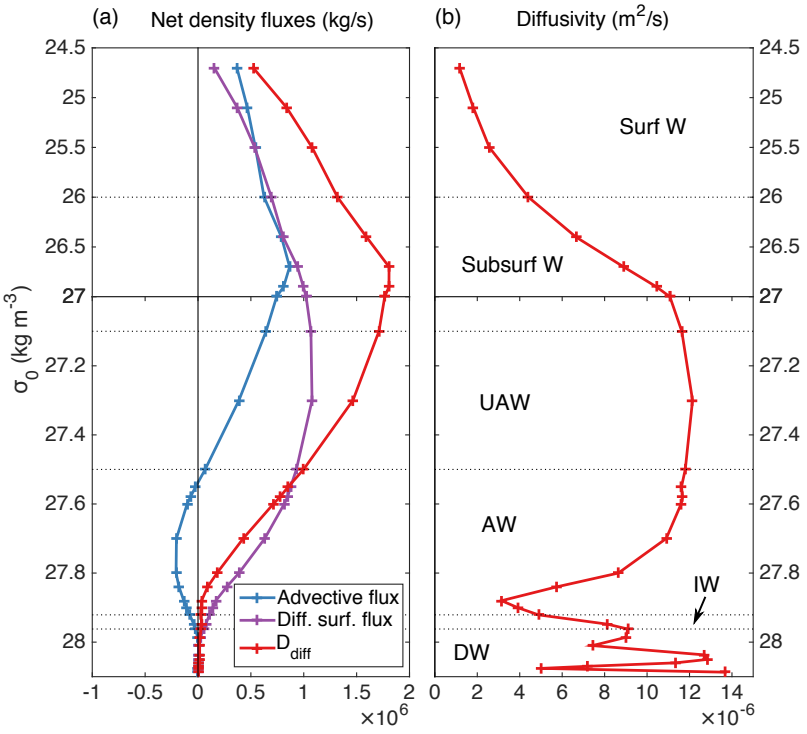

FIGURE 2.10: (a) In blue, the sum of advective density fluxes ($\overline{\rho}_{bdy}T - \rho W_{(\rho)} + \rho_{surf}M_{surf}$). In purple, diffusive surface density fluxes, as shown in Figure 2.8. In red, the interior diffusive flux of density, D_{diff}, required to balance advection and surface buoyancy fluxes. (b) Diffusivity, K, calculated from Equation 2.4.

invalid - the density budget requires a positive upward diffusive flux of density of order 1×10^6 kg s^{-1} in all parts of the water column. This reaches a maximum at around $\sigma_0 = 26.900$ kg m^{-3} in the Subsurface Water layer. Figure 2.10c shows the diffusivity implied by this density flux in accordance with Equation 2.4. Throughout most of the water column below the surface layers, diffusivities of approximately $1.0 - 1.2 \times 10^{-5}$ m^2 s^{-1} are seen. Some variation from layer to layer is seen in the Deep Water at potential densities greater than $\sigma_0 = 28.000$ kg m^{-3}, but density gradients and isopycnal surface areas are both small in this region (see Figure 2.11), as is the smoothing effect of integration of boundary fluxes up from the seafloor, so this is likely simply to be noise. In the surface layers above $\sigma_0 = 27.000$ kg m^{-3}, the implied diffusivity declines steadily towards the surface, reaching a value of 1.3×10^{-6} m^{2}s^{-1}, an order of magnitude smaller than the level below the halocline, at $\sigma_0 = 25.000$ kg m^{-3}.

2.3.4 Sources of uncertainty

We remark that there are large uncertainties associated with the boundary velocity estimates used in these calculations, which are described in detail by Tsubouchi et al.

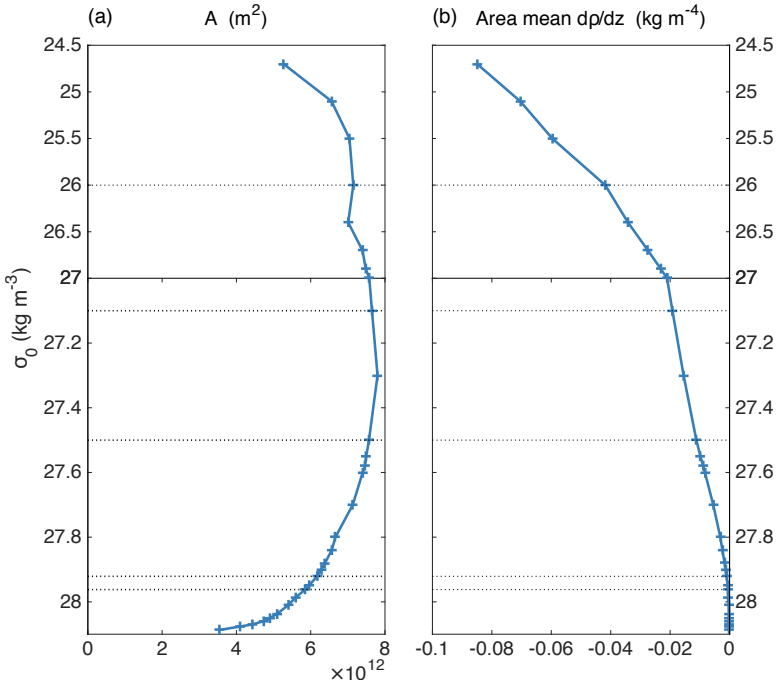

FIGURE 2.11: (a) Isopycnal surface areas and (b) basin-mean density gradients calculated from the PHC 3.0 climatology.

(2012). In particular, uncertainties in the model diapycnal transports from which the velocity field employed in the current study was derived are of the same order of magnitude or more as the volume transports themselves. It is also worth noting that the inverse model used to produce the estimates was not tuned to provide boundary velocities for the purpose for which we have used them here.

Although we have attempted to gain an understanding of the scale of errors potentially associated with the reanalysis surface flux data (see Figure 2.9), some further uncertainty remains because of the sparsity of measurements available to constrain the data in the Arctic compared to other parts of the world. A potentially larger source of error is associated with the extent to which the PHC climatology, which was used to map surface buoyancy fluxes to isopycnal layers, offers a good representation of the ocean state in the period to which the reanalysis data relate. Although PHC is probably still the best climatology available for the Arctic, it is based on sparse observations of the ocean interior, some of which were collected as long ago as the 1950s and are probably not representative of the Arctic Ocean of the mid 2000s, given the rate of change in the region over the late 20th and 21st centuries.

2.4 Discussion

The broad picture shown by our estimates of diapycnal transports (Figure 2.6) is one of a double-overturning cell, consistent with the model of the Arctic described in the literature (e.g. Eldevik and Nilsen (2013), Rudels (2010)). In the lower cell, slightly less than half of inflowing AW becomes more dense through surface heat loss (Figure 2.10). Turbulent mixing plays a secondary role in this cell. In the upper cell, the remainder of the influx of AW is transformed into lighter UAW through mixing with the surface-freshened water classes above. Heat is still lost to the atmosphere from this water, but upward flux of density by turbulence dominates.

There is reasonable agreement between our estimates of the rates of transformation of inflowing Atlantic Water and the volume transports for different density classes across the Fram Strait and Barents Sea Opening calculated using an inverse model by Isachsen et al. (2007) from climatological wind stresses and hydrographic data for the Nordic Seas. We see an inflow of Atlantic Water to the Arctic of 3.3 Sv, compared to their estimate of 2 Sv. Their estimate of the outflow of lighter water classes, at 1 Sv, is smaller than the 1.8 Sv of Atlantic Water that we calculate is lost to the Upper Atlantic Water and Subsurface Water classes, but does not include exports from the Arctic via the Davis Strait. The figure of 2 Sv that they give for denser water exiting the Arctic is larger than our estimate of 1.5 Sv, but still within the estimates of uncertainty given by Tsubouchi et al. (2012) for the volume transports used in the current study.

In contrast to the finding of Isachsen et al. (2007) for the Nordic Seas, we find that in the Arctic Ocean diffusive fluxes due to interior mixing appear to play as significant a role as surface buoyancy fluxes in controlling water mass transformations. Density budgets that include allowance both for advective fluxes and surface buoyancy fluxes produce realistic estimates for turbulent diffusivity throughout much of the water column of $\sim 1 \times 10^{-5}$ m^2 s^{-1}, averaged over the entire surface area of an isopycnal, which accords with values given by de Lavergne et al. (2016) for a diffusive regime that is transitional between buoyancy-controlled and energetic mixing. Rippeth et al. (2015) also estimated diffusivities of order 1×10^{-5} m^2 s^{-1} from microstructure measurements, but these were collected in relatively shallow water; a comparison of our results with their observations is given in Chapter 3. Enhanced mixing of around 2.5×10^{-4} m^2 s^{-1} was observed by Padman and Dillon (1991) in isolated areas on the slope of the Yermak Plateau. Away from the continental slopes, other authors including Lenn et al. (2009) and Guthrie et al. (2017) have found evidence of double diffusive effects, indicative of a less turbulent regime, with diffusivities of order 1×10^{-6} m^2 s^{-1} . Averaged across the Arctic basin, therefore, our results appear to be in line with those presented by others.

Note the apparent sharp drop in diffusivity at the base of the AW layer in Figure 2.10b. We attribute this to localised downwelling due to convection in the Barents Sea, which would have the effect of reduced the basin-mean values of diffusivity for these potential densities, but the scope of this control volume-based study does not extend to confirming this hypothesis.

There are other potential sources and sinks of density that we have not included in the calculations here because they are expected to be small in comparison with those driven by surface heat and freshwater fluxes. The first of these is the annual sea-ice freeze/melt cycle: this would not be expected to affect the overall input of density to the ocean, but it is generally accepted that over the course of a season it contributes to the production of dense water by brine rejection, which would manifest itself as a source of water in the denser layers. Nevertheless, the largest part of the freeze/melt cycle occurs over shelves where water is reasonably well mixed, so freshwater released during the melt phase would be expected to remix with the brine produced at the freeze stage in the spring. In practice, we expect that most of the dense water contributing to our deepest layers is formed on the Barents Shelf where the heavier water layers outcrop in winter, and that region is largely ice-free all year round.

Neither have we accounted for the latent heat of fusion released during the formation of sea ice, which would have the effect of reducing the density of surrounding seawater. To the extent that the sea ice formed is subsequently exported from the Arctic, the latent heat constitutes a net source of buoyancy. If we assume that the annual volume flux of sea ice through the Fram Strait, which carries nearly the entire sea ice export from the Arctic (Kwok et al., 2009) is 2600 km^3 yr^{-1} (Spreen et al., 2009), multiplying by a sea ice density of 900 kg m^{-3} and a latent heat of fusion of 3.34×10^5 J kg^{-1} gives a simple estimate of the heat input involved of 25 TW. For comparison, the net inflow of heat to the Barents Sea by advection of AW is approximately 73 TW (Smedsrud et al., 2010). At first sight, therefore, the contribution of latent heat might appear significant. Nevertheless, in practice much of the sea ice exported from the Arctic is formed in other parts of the region (Pavlov et al., 2004) from lighter surface waters than the water classes we focus on in this study.

A further, interior, source of density is that produced through the mixing of water masses of similar densities but differing temperatures and salinities because of the non-linearity of the equation of state of seawater. Marsh (2000) found cabelling significant, but highly localised and seasonal, in model representations of the North Atlantic. He noted that it was strongest in summer at the Sub-polar Front. Although the effect might be at play around the upper edge of the AW layer in the Arctic, where warmer, more saline AW encounters cooler, fresher subsurface waters, we would expect it to be less significant here because temperature variations are much smaller than those seen in the North Atlantic.

Timmermans and Garrett (2006) considered the effect of geothermal heat input - which would lead to a reduction in density of bottom waters - in the Makarov Basin. They concluded that it was insufficient to cause convective overturning, but might raise the temperature of inflowing water by around 0.01 °C. This would be equivalent to a heat flux of around 50 mW m^{-2}. In comparison, annual mean total net surface heat fluxes in the ice-free surface regions, with surface area totalling perhaps half of that over which geothermal heating might act, reach around 100 W m^{-2}, or three orders of magnitude greater.

2.5 Conclusions

The objectives of this chapter were to confirm the hypothesis that the Arctic Ocean hosts a double overturning and to assess the relative importance of surface buoyancy fluxes and interior mixing as drivers for the overturning. The results we present here support the existence of such a two-celled overturning. In the upper cell, slightly more than half of the 3.3 Sv of inflowing AW loses density through mixing with surface waters freshened by influx of runoff and precipitation, while densification of the remainder caused by heat loss on the Barents shelf drives the lower. The basin-mean turbulent diffusivities at the upper surface of the AW layer required to balance density budgets, of order 1×10^{-5} m^2 s^{-1}, are in line with those seen in observations, recognising that levels of turbulence vary markedly across the Arctic basin.

While the control volume approach that we have adopted here has allowed us to estimate levels of mixing, it provides no information about the drivers or spatial distribution of the mixing. We return to this subject in the next chapter.

Chapter 3

Is Arctic Ocean upwelling driven by tides?

3.1 Introduction

In the previous chapter we derived volume and density budgets for a control volume comprising the Arctic Ocean and Baffin Bay, and hence produced estimates of the strength of the overturning circulation in the Arctic and the associated level of turbulent mixing required to balance the budgets. Since the budgets were computed for the entire basin, however, they provide no information about where in the basin the mixing occurs or what the source of energy to driving it might be. In this chapter we compare the estimates of turbulence we have derived with observations of turbulent mixing made with microstructure profilers across the Arctic basin. We go on to consider a possible source of the energy required to support the level of turbulent buoyancy flux we have computed.

As discussed in Chapter 1, several previous studies have addressed the role of double diffusion in driving vertical heat fluxes in the Arctic Ocean. Double diffusion occurs at an interface between relatively cool, fresh water and warmer, saltier water. Here, the vertical gradients of salt and heat tend to oppose one another in contributing to the gravitational stability of the water column. The effect arises because the molecular diffusivity of heat is much greater than that of salt. It has two forms. If the cool, fresh water overlies the warm, salty water, water from the upper layer that is in contact with the lower layer will gain heat from its surroundings more quickly than it will gain salt, and will thus increase in buoyancy, whereas water from the lower layer will lose heat faster than it loses salt and will decrease in buoyancy. The consequence in this situation, known as diffusive layering, is convection within each layer and a net upward flux of heat. Diffusive layering is known to be widespread throughout the Arctic Ocean

(Polyakov et al., 2019), and has been implicated as a major contributor to the cooling of the Atlantic Water layer in the eastern Arctic Ocean.

The contrary case, where warm, salty water overlies cold, fresh water, leads to a phenomenon known as salt fingering. Here, a small intrusion from the upper layer to the lower loses heat and buoyancy and thus sinks further. Likewise, an intrusion from lower layer to the upper gains heat and buoyancy and continues to rise. Once again, the consequence is an up-gradient flux of buoyancy. Rudels et al. (2009) describe a mechanism by which the motion of water parcels in areas where double diffusion is occurring leads to small-scale mechanical mixing. They also note that at fronts, such as between the Fram Strait and Barents Sea branches of Atlantic Water inflow, where they meet north of Severnaya Zemlya, lateral gradients of heat and salt can lead to the interleaving of layers, such that conditions favourable to diffusive convection and salt fingering are present alternately between them. This can generate buoyancy forcing that promotes motion across the front and leads to lateral mixing between the water masses. In general, however, diapycnal diffusivities associated with double diffusion, typically $O(10^{-6})$ m^2 s^{-1} (Timmermans et al., 2008; Lenn et al., 2009), are an order of magnitude smaller than those we calculate for the upper part of the AW layer. Overall, the effect of double diffusion is to cool and thereby densify saline water. While it may contribute to the loss of heat from Atlantic Water in the lower limb of the overturning, for the upper limb we seek a cause of upwelling: we require a driver of mechanical mixing.

Input of kinetic energy to the ocean is commonly ascribed to one of two sources: winds or tides. Rippeth et al. (2015) considered the possible role of each of these in explaining elevated rates of turbulent kinetic energy (TKE) dissipation seen in microstructure observations (described below), and found that dissipation was enhanced over the continental slope regions but apparently insensitive to sea ice cover. Since sea ice could be expected to inhibit the transfer of momentum from the atmosphere to the ocean, they concluded that the enhanced dissipation they saw was not wind-driven, and that the interaction of tides with steep topography should be implicated instead. In this chapter we investigate the plausibility of tidal mixing as a driver for turbulent buoyancy flux.

3.1.1 Microstructure observations

The series of microstructure measurements presented by Rippeth et al. (2015) was collected over the period 2007 to 2013. Together, they cover much of the seasonally ice-free Arctic Ocean, including the shelf breaks north of Svalbard, north of Severnaya Zemlya, the Laptev Sea, East Siberian Sea and Canada Basin. Locations of the measurements are shown in Figure 3.1, along with some indicative profiles of TKE dissipation, ε. The grey shading on the profiles indicates potential density anomalies

(calculated from measured temperature and salinity values) of between 27.0 and 27.8 kg m^{-3}, the densities for which enhanced diffusivities were given by the density budgets described in Chapter 2.

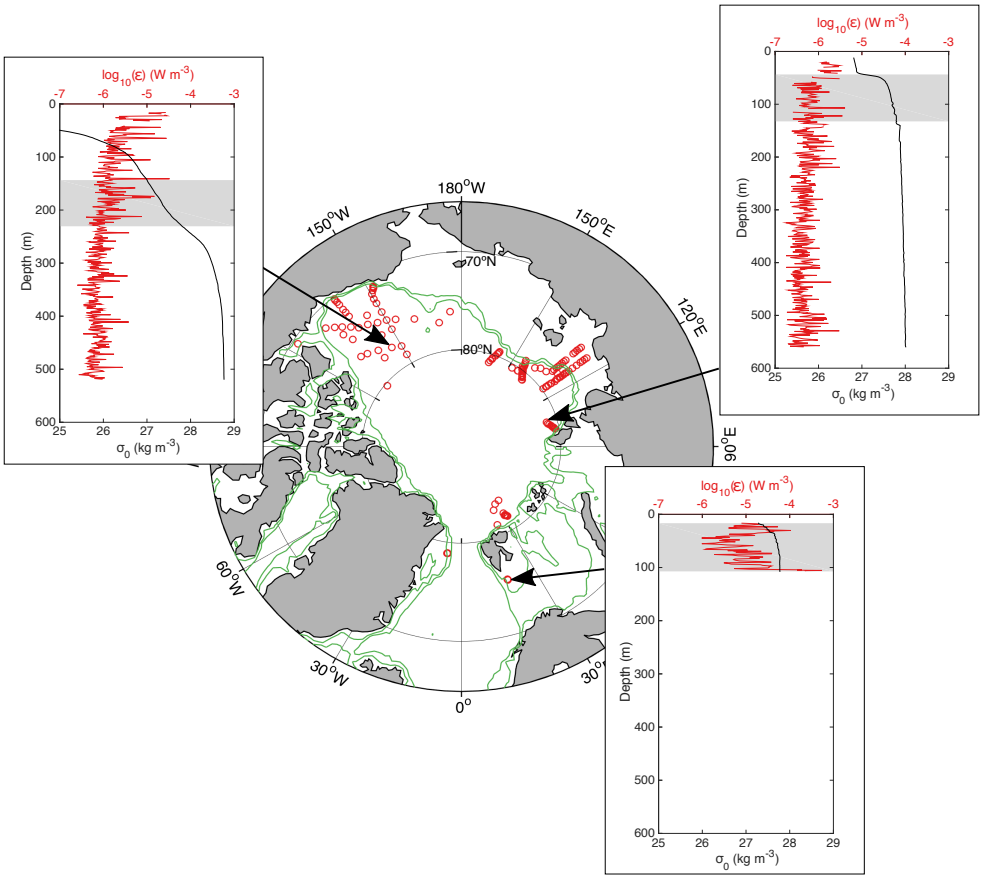

FIGURE 3.1: Locations of the microstructure observations presented by Rippeth et al. (2015). The 200 m and 500 m depth contours are shown in green. The insets show selected profiles of TKE dissipation (red) and potential density (black), with grey shading indicating values of σ_0 between 27.0 and 27.8 kg m^{-3}.

As would be expected given the variety of bathymetry underlying the locations where the measurements were made and the span of seasons, from spring through summer to autumn, in which the field campaigns took place, there is wide variation in levels of TKE dissipation measured. Away from the shelf areas, and on the shelf breaks of the Laptev Sea and East Siberian Sea, values of O(10^{-6}) W m^{-3}, equivalent to a diffusivity of O(10^{-7}) m^2 s^{-1}, are typical. Some of the profiles, notably from the Canada Basin, show TKE dissipation an order of magnitude higher near the surface. This surface intensification is, however, evidence of wind-driven mixing that will have little effect on the Atlantic Water layer beneath (Rippeth et al., 2015). Only in a few isolated profiles from the Barents Sea to the south of Svalbard and the deeper water to the north east of Svalbard is turbulence indicating diffusivities of O(10^{-5}) m^2 s^{-1} and higher seen in water of the density classes under consideration here. Of the 299 profiles collected from locations within the domain described in Chapter 2, only 105, or 35%, show mean ε

values consistent with the buoyancy fluxes across the UAW layer implied by the density budgets, assuming a mixing efficiency (see below) of 0.2. If the shelf areas, from which the AW and UAW water classes are largely absent (see Figure 3.2), are excluded, the proportion of profiles meeting the energy requirement falls to 20 out of 161, or 12%.

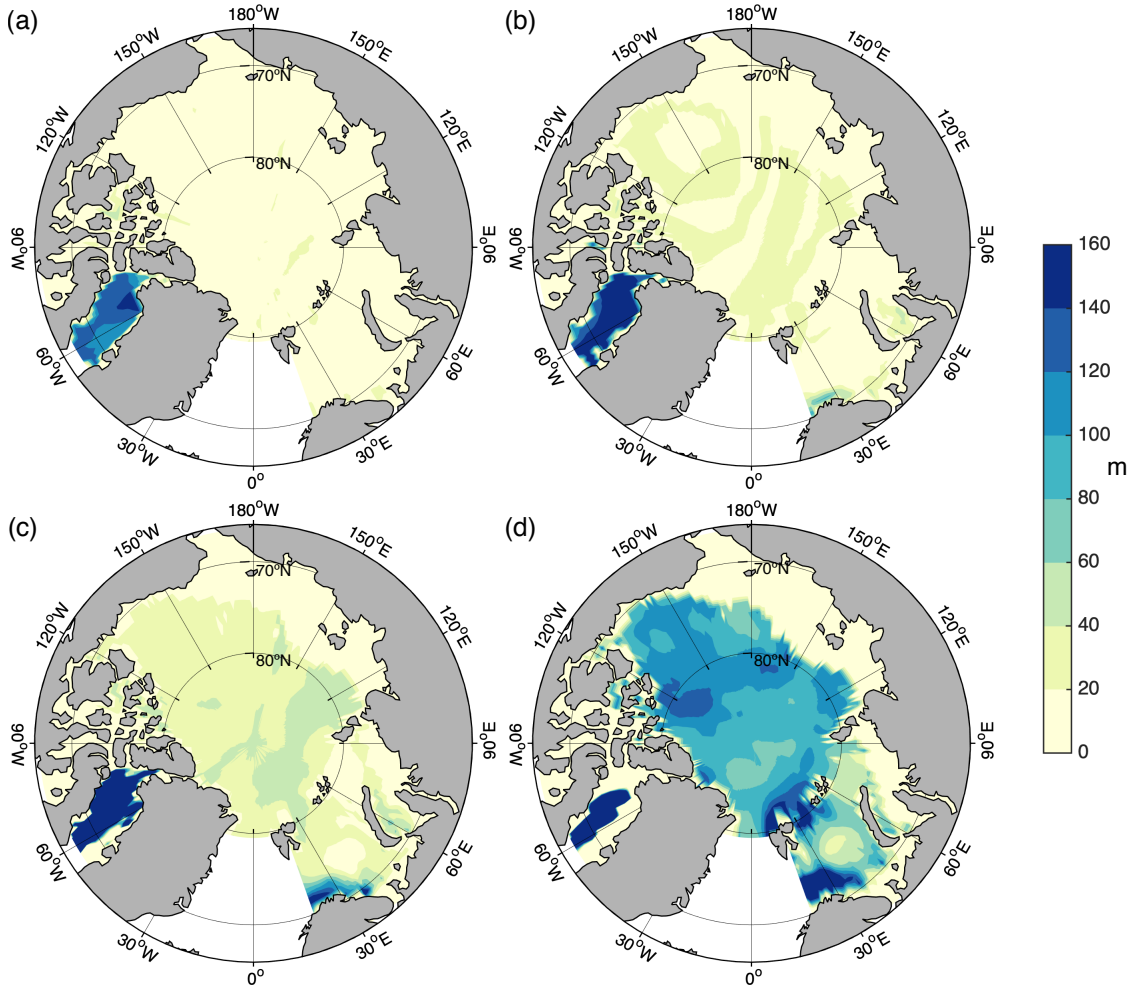

FIGURE 3.2: Annual mean thicknesses of density layers, as calculated from the Polar Science Center Hydrographic Climatology v.3.0: (a) water with σ_0 between 27.1 and 27.3 kg m^{-3} (less dense Upper Atlantic Water); (b) σ_0 between 27.3 and 27.5 kg m^{-3} (denser Upper Atlantic Water); (c) σ_0 between 27.5 and 27.7 kg m^{-3} (less dense Atlantic Water), σ_0 between 27.7 and 27.9 kg m^{-3} (denser Atlantic Water).

3.1.2 Tides as a potential energy source

At first sight, therefore, there would appear to be an inconsistency between the basin-mean diffusivities we have inferred from the density budgets described in the previous chapter and the values actually observed in the Arctic Ocean. If the diffusivities suggested by the microstructure measurements were averaged over the ensemble of profiles collected they would fall some way short of the basin means required to balance the budgets. A closer look, however, provides a clue to a potential

source of energy to drive the diapycnal mixing we infer. In common with other observational studies, e.g. d'Asaro and Morison (1992) and Fer et al. (2010), the observations show enhanced TKE dissipation in areas of rough topography. Rippeth et al. (2015) have also shown a tentative correlation between enhanced levels of ε over the continental shelf break and rate of conversion of barotropic tidal energy.

Although tidal currents have in some instances been associated with the production of internal waves in the Arctic Ocean (e.g. Padman et al. (1992)), tidal energy has hitherto received little attention as a potential driver of turbulent mixing within the Arctic Ocean both because tidal velocities there tend to be low (Padman and Erofeeva, 2004) and because most of the Ocean lies north of the critical latitude at which the local inertial period is equivalent to the period of the main semi-diurnal tidal constituents. Consequently, internal waves generated by the interaction of the tides with topography are not expected to propagate away from the generation site. Rippeth et al. (2017) have, however, proposed a mechanism for tidal conversion by which supercritical tidal flows over topography can cause short length-scale internal waves which are trapped initially but become free to propagate away when the tidal flow slows. These higher frequency internal waves may thus facilitate the conversion of energy from the barotropic tide.

The potential existence of a mechanism by which energy might be transferred from the barotropic tide into turbulence raises a question: is the rate of energy conversion sufficient to power the turbulent mixing that we have inferred is taking place? That is the question that we seek to address in this chapter. To do so, we use estimates of the tidal energy conversion rate introduced by Rippeth et al. (2015) and described in Section 3.2.1 below.

St. Laurent and Simmons (2006) give the steady state balance of TKE over a control volume (V) as

$$\int P \mathrm{d}V = \int \rho\varepsilon \mathrm{d}V + \int \rho\kappa_\nu N^2 \mathrm{d}V \tag{3.1}$$

where P is the mechanical power supplied to finestructure scales, ρ density and κ_ν turbulent diffusivity. The first term on the RHS represents the rate of dissipation of energy through the molecular viscosity of the seawater, and the second the rate of conversion to potential energy (PE) through turbulent diffusion. It is the quantity described by this latter term that we estimated in the previous chapter. With κ_ν given by Equation 2.4 as $\frac{-D_{diff(\rho)}}{A\frac{\partial\rho}{\partial z}}$ and N^2 defined as $\frac{-g}{\rho}\frac{\partial\rho}{\partial z}$, it may be expressed as $\int\int g\, D_{diff}\, \mathrm{d}z\, \mathrm{d}A$, and over the domain shown in Figure 2.2 amounts to 2.2 GW. For those water classes constituting the upper cell of the overturning only, as marked in Figure 2.6, the energy requirement is 1.3 GW.

Power input may come from any of several sources, including mesoscale eddies, interaction of the mean flow with topography or convection. We seek here to establish

whether input from the barotropic tide might be sufficient to make a significant contribution to the energy requirement. Integrating power input from the M2 and S2 tidal constituents, in which most of the tidal energy in the Arctic Ocean is contained, over the domain shown in Figure 2.2, gives a total power supply of 114 GW. In order to quantify what proportion of the energy supplied by the barotropic tide, the LHS of Equation 3.1, is available to drive turbulent mixing, the second term on the RHS, as opposed to being dissipated through molecular processes, the first term on the RHS, it is necessary to make some assumption about the ratio between these two sinks of energy, which is related to the so-called mixing efficiency. Adopting the widely used value of 1:5 would suggest that 19 GW is available for conversion into PE, or slightly less than 9 times the power required for the integrated turbulent buoyancy flux. Recalling, however, that the energy conversion mechanism proposed by Rippeth et al. (2017) involves tidal flow over rough topography, we might limit the area of integration to regions in which water depth is between 250 m and 1000 m as a proxy for the continental slope, giving a more conservative estimate of 3.2 GW, still more than sufficient in total to meet the energy requirement.

It is not enough, however, for sufficient energy to be available within the Arctic Ocean as a whole to drive turbulent mixing. The energy must be available to mix water in those density classes in which we have determined that mixing is occurring. Our aim, therefore, is to assess whether the spatial distribution of energy availability accords with the spatial distribution of those water masses we have identified as experiencing enhanced diapycnal mixing.

3.2 Methods and materials

3.2.1 Tidal model data

The estimates of rate of conversion of energy from the barotropic tide that we compare with the energy requirement to drive mixing were derived by the method of Egbert and Ray (2001). They were computed, as described by Rippeth et al. (2015), as the local difference between the mean rate of working by the tide-generating force and the divergence of the vertically integrated time-averaged horizontal flux of energy. The volume fluxes used to calculate these quantities were derived from tidal amplitudes and currents from the altimetry-constrained TPXO8 inverse solution (Egbert and Erofeeva, 2002; Padman and Erofeeva, 2004). The energy conversion estimates are gridded at $1/30^\circ$ resolution. Estimates of conversion from the M2 and S2 tidal constituents together are shown in Figure 3.3. To eliminate some unphysical values arising from the calculation, a ceiling of 1 W m^{-2} and a floor of 0 W m^{-2} have been applied to the data. The effect of these is to set to zero the 43% of data points which have negative values, and to set to 1 W m^{-2} the 0.3% of data points which are in excess of this

ceiling. It is apparent that the elevated conversion rates are highly localised, but there is some overlap between the areas where these occur and the presence of water of the classes for which the density budgets suggest higher turbulent diffusivities, as shown in Figure 3.2(a) - (c).

While the estimates give an indication of the horizontal distribution of available energy, they are depth-integrated and contain no information about the distribution of energy vertically in the water column. In each of the comparisons we present here, we have therefore assumed one of four profiles for vertical distribution: a uniform distribution, an exponential distribution with e-folding length 500 m decreasing with height above bottom (in line with that adopted by St. Laurent et al. (2002)), or an exponential distribution with e-folding length 200 m or 40 m. The form of each of these profiles is shown in Figure 3.4 for an illustrative water depth of 500 m, typical of the slope regions where many of the areas of enhanced energy conversion are located. Sensitivity of the results to choice of vertical profile is discussed in Section 3.3 below. Regardless of the vertical profile chosen, we have in each case excluded energy in the upper 30 m of the water column, since we assume that this water is well mixed by winds and that no turbulence in this region is driving diapycnal mixing.

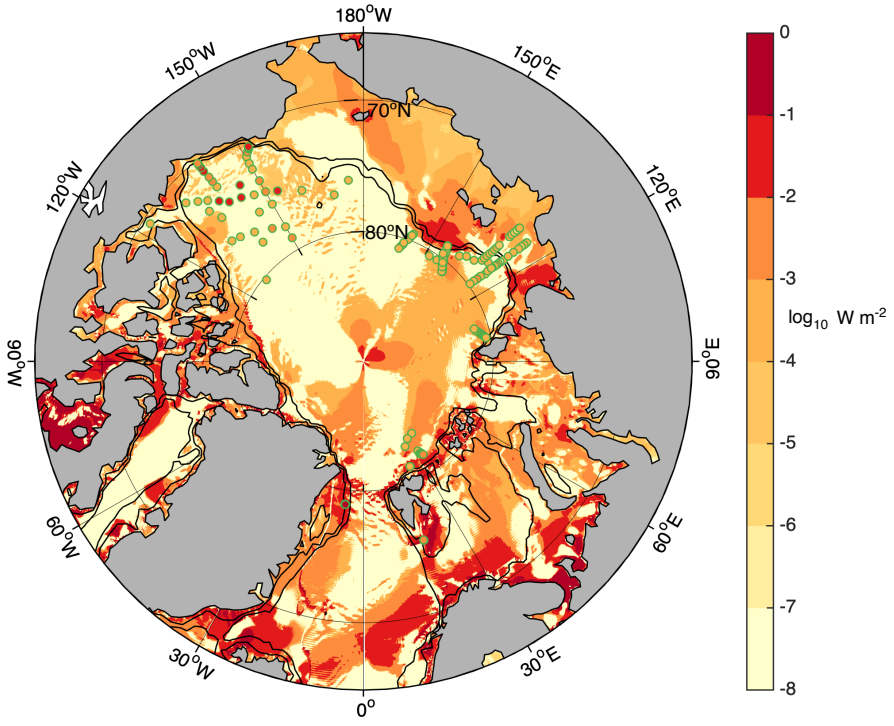

FIGURE 3.3: Rate of conversion of tidal energy, with depth-integrated TKE from the microstructure observations of Rippeth et al. (2015) superimposed.

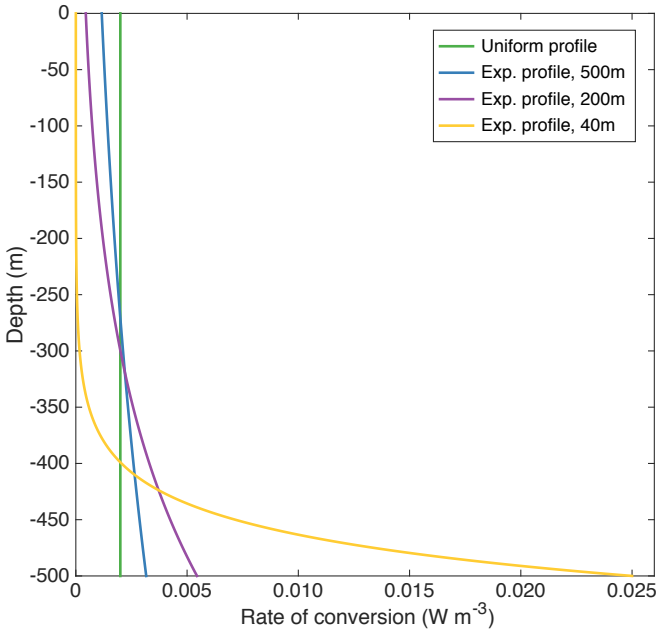

FIGURE 3.4: Illustrative profiles of the rate of conversion of tidal energy, assuming a unit depth-integrated conversion rate and a water depth of 500 m.

3.2.2 Attribution of tidal energy to density classes

To determine whether sufficient energy is available from tidal conversion to meet the requirement to drive mixing in each of the density classes discussed in the previous chapter, it is necessary to map tidal energy onto the density field. We once again use the PHC 3.0 climatology described in Section 2.2.5 to calculate potential densities, but because most of the areas of elevated tidal dissipation are found in the Barents Sea and the shelf break regions which experience strong seasonal variation in densities, we have run the calculations of energy availability month by month, before calculating annual means. Although PHC monthly data are available only for depths down to 1500 m, none of the water classes for which we wish to quantify energy availability extends much below that depth. In addition, little tidal dissipation is evident in deeper water, and so we do not expect the absence of densities for depths greater than 1500 m to have a significant effect on the comparisons.

Density fields were calculated from PHC temperature and salinity data available at 1° horizontal resolution using the SeaWater MATLAB library (version 3.3). These were then regridded onto the 1/30° grid used for the tidal conversion estimates using the SOSIE software package (https://sourceforge.net/projects/sosie/). Although the Akima interpolation method selected is intended to avoid the production of interpolated values that fall outside the range of values in the input data, a few unphysical density values resulted from the interpolation; the 9.9% of grid cells where

values lower than 1018 kg m^{-3} or higher than 1029 kg m^{-3} were generated have been excluded from the tidal energy comparisons.

Further, and potentially even more significant, a shortfall in the regridded density field arises from the resolution of PHC data in the vertical. At depths below 150 m, the spacing of PHC depth levels is 50 m or 100 m. For the core comparisons, we have not extrapolated density values below the lowest PHC values for which we have data since we lack a solid physical basis on which to do so, but this means that tidal energy in the lowest 100 m of each grid cell, where the highest levels of dissipation might be expected to occur, is potentially excluded from the basin-integrated totals we calculate. We discuss the potential extent of this undercounting in Section 3.3 below.

3.2.3 Mixing efficiency

Many authors have adopted a value of 1/6 for mixing efficiency, but some (see de Lavergne et al. (2016) for a summary) have suggested that mixing efficiency depends on the balance between the intensity of turbulence and the strength of damping stratification, and is lower than 1/6 in situations where turbulence is any more than moderately energetic. Here, we compare estimates of available energy calculated using the widely-adopted mixing efficiency of 1/6 with those derived instead using a parameterisation given by de Lavergne et al. (2016) in which mixing efficiency, R_f, is expressed in terms of a turbulence intensity parameter Re_b, which is a measure of the balance between destabilising forces as represented by TKE dissipation, and stabilising forces in the form of stratification:

$$R_f = 1/(1 + 0.25\sqrt{\mathrm{Re}_b}) \qquad \text{for } \mathrm{Re}_b \geq 400 \tag{3.2}$$

$$\mathrm{Re}_b = \varepsilon/\nu N^2, \tag{3.3}$$

where ν is the kinematic viscosity of seawater.

3.3 Results

A core set of calculations was performed in which the vertical distribution of tidal energy conversion was assumed to be either uniform or exponential with e-folding length 500 m and the mixing efficiency either 1/6 or varying as in Equation 3.2. Figure 3.5 shows the derivative with respect to potential density of the rate of energy conversion given by these assumptions. Also shown, for comparison, is the turbulent buoyancy flux given by the density budgets described in Chapter 2.

Figure 3.6 shows counts of the parameterised mixing efficiencies for each grid point and month for the exponential distribution. Although significant reductions from the

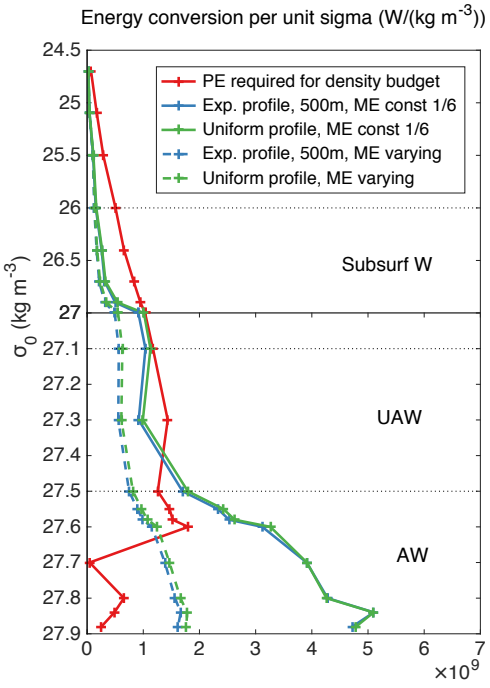

FIGURE 3.5: In red, the energy required to drive diapycnal mixing and overcome stratification, as calculated from density budgets. In blue, tidal energy available for mixing, assuming an exponential distribution in the vertical. In green, tidal energy available for mixing, assuming a uniform distribution in the vertical. The solid green and blue lines indicate a constant mixing efficiency of 1/6. For the calculations shown by the dashed lines, the mixing efficiency given by Equation 3.2 has been assumed. Dotted lines mark the boundaries between water classes: Subsurf W, Subsurface Water; UAW, Upper Atlantic Water; AW, Atlantic Water.

default value of 1/6 are seen in only a small proportion of cases – fewer than 9% – because these include those areas where mixing is particularly energetic, the overall effect on the calculated energy supply is a substantial reduction – by more than half in the denser water classes.

In comparison to the energy requirement calculated from the density budgets, all four combinations of core assumptions appear to deliver sufficient tidal energy across most of the AW layer. For the UAW and lower region of the Subsurface Water, which together constitute the bulk of the upper limb of the overturning, the picture is less clear. Although the tidal energy is the right order of magnitude, the results show a shortfall in these density classes, especially if the variable mixing efficiency is assumed. Nevertheless, given the uncertainties in the density budgets discussed in Section 2.3.4, as well as similar uncertainties associated with the use of PHC to determine the density field in the current calculations, there is almost complete overlap between energy supply and requirement within the margins of error.

It is readily apparent that this initial choice of vertical energy profile makes little difference, although given that the bulk of the mixing hotspots shown in Figure 3.3

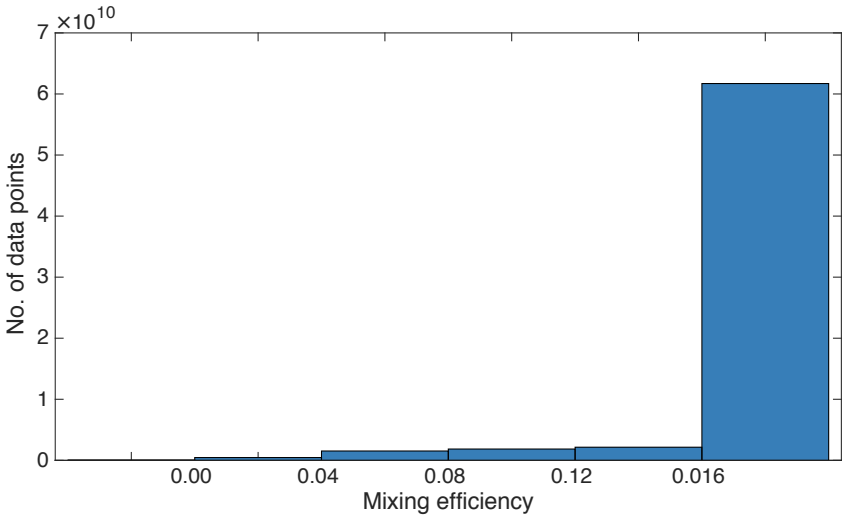

FIGURE 3.6: Counts of mixing efficiencies, R_f, calculated according to Equation 3.2, for each grid point and month, assuming an exponential distribution of energy conversion in the vertical, with e-folding length 500 m.

occur in water that is fairly shallow in comparison to the selected e-folding length of 500 m, the two profiles are rather similar. Nevertheless, 500 m was found by St. Laurent et al. (2001) to be an upper estimate of decay scale. Furthermore, their observations of enhanced dissipation were made above the Mid-Atlantic Ridge in the abyssal Brazil Basin, and are unlikely to be representative of conditions in the Arctic slope regions, where mechanical energy is expected to be concentrated in a bottom boundary layer only a few tens of metres thick. We have therefore tested the sensitivity of the results to choice of decay scale by rerunning the calculations with e-folding lengths of 200 m and 40 m. As seen from Figure 3.7, a decay scale of 40 m gives rise to a reduction in available energy of 20 – 30% in the UAW classes, compared to the core set of results.

The assumed mixing efficiency also has a notable effect on the results. We infer that because the mixing is concentrated so tightly in hotspots, nearly all of the converted energy contributing to the basin totals is in regions of comparatively strong (in Arctic Ocean terms) turbulence, and thus well within the regime of high turbulence intensity parameter.

As mentioned above, however, there are two factors that might lead to an undercounting of available energy. The first is that the 30 m assumed for the mixed layer depth, above which tidal energy is assumed not to drive diapycnal mixing, might be somewhat conservative. Examination of temperature and salinity data associated with the microstructure profiles described in Section 3.1.1 suggests that south of Svalbard the mixed layer depth was more like 25 m, and west of Svalbard closer to 12 m. On the other hand, if these observations of stratification were made under

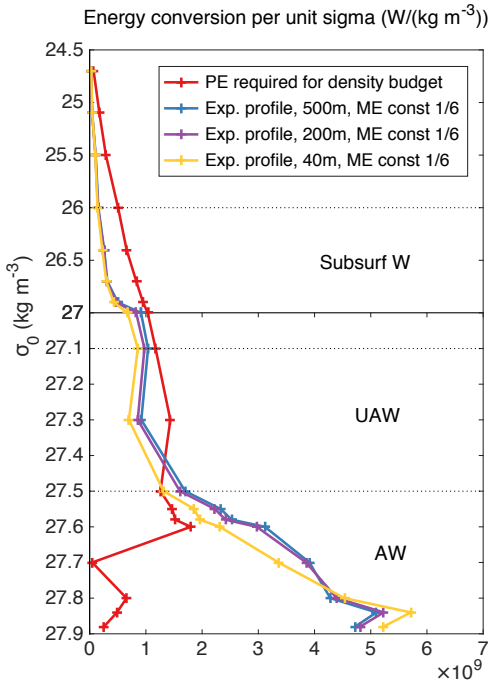

FIGURE 3.7: Sensitivity to e-folding length. In blue, energy availability as in Figure 3.5 for an e-folding length of 500 m. In purple, the same but for an e-folding length of 200 m, and in yellow, for a length of 40 m.

relatively benign conditions and strong stratification they might not be representative. To test the effect of choice of mixed layer depth, the calculation assuming a uniform profile and constant mixing efficiency was rerun, this time including energy in the top 30 m. (See Figure 3.8.) Including the mixed layer delivers up to an extra 70 % of energy in the middle of the UAW layer. In retrospect, it might have been more logical in this sensitivity test to use the variable mixing efficiency by which - to the extent that the PHC climatology is a reasonable reflection of the stratification the mixing actually sees - the effect of reduced stratification is accounted for in the parameterisation, but time did not permit. Nevertheless, the test does suggest that some tidally-driven mixing near the surface might be missed in the core calculations.

The other area where available energy is certainly uncounted is in the lowest part of the water column, below the depths in each grid cell for which PHC data are available. As a further sensitivity test we have rerun the 200 m e-folding calculation (in which the bottom-enhancement effect will be felt more strongly) with the deepest potential densities in the regridded 1/30° dataset extended to the seafloor; the results are shown in Figure 3.9. An additional 30 % or so of energy is available in the UAW class, and approximately 15 % more for AW. In reality, of course, stratification of the water column means that densities in the deeper water will often be higher than those assumed here, and so the distribution of additional energy might tend towards denser water than these calculations would suggest.

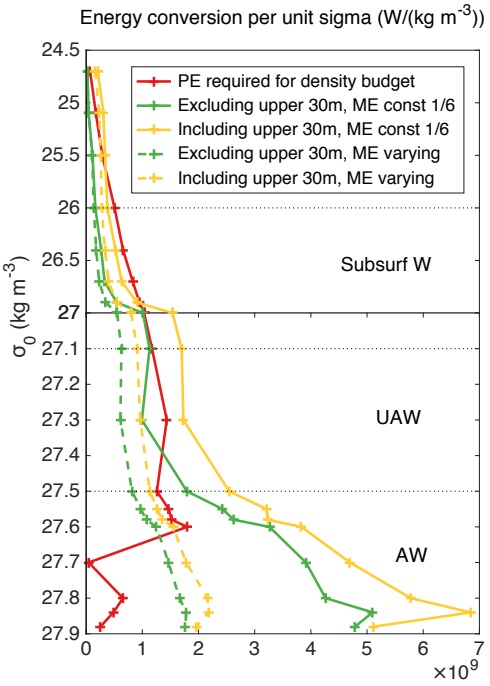

FIGURE 3.8: Effect of exclusion of energy in the mixed layer. In green, energy availability as in Figure 3.5, excluding the upper 30 m. In yellow, the same but including energy in the upper 30 m.

3.4 Discussion and Conclusions

The objective that we defined for this chapter was to establish whether sufficient energy was available from conversion of the barotropic tide to drive the diapycnal mixing we had quantified from density budgets in the last chapter. The results presented in Section 3.3 suggest that the rate of conversion is more than sufficient in the denser waters of the AW layer that form part of the lower limb of the overturning. In the upper part of the AW layer and above, the comparison between energy supply and requirement is more finely balanced. Sufficient energy appears to be available if the mixing efficiency is somewhat higher than that suggested by the parameterisation of de Lavergne et al. (2016) and/or a significant amount of tidal conversion is excluded from the calculations because it takes place at the margins - either horizontal or vertical - of the domain in areas not covered by the PHC-derived density field. (This might well be the case: several of the tidal hotspots seen in Figure 3.3 lie in coastal areas into which PHC does not extend.)

The conversion of energy from the barotropic tide does not imply that all such energy drives turbulent buoyancy flux. The mechanism that Rippeth et al. (2017) proposed by which energy is made available for mixing is not well studied, and it appears likely in any case to depend heavily on local topography, flow conditions and water stratification. Rippeth et al. (2017) also point out that their microstructure

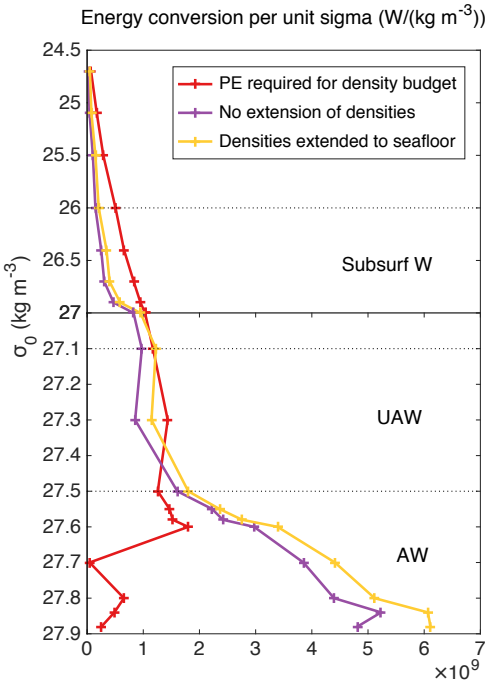

FIGURE 3.9: Effect of including mixing in water deeper than the lowest available PHC layer. In purple, energy availability assuming a constant mixing efficiency and e-folding length of 200 m, with the integration limited to depths within the PHC envelope, as in Figure 3.7. In yellow, the same but assuming that densities given by the deepest PHC data points extend to the seafloor.

observations suggest that a significant but not well-quantified proportion of the converted energy is dissipated in the well-mixed bottom boundary layer rather than contributing to mixing to overcome stratification.

Nevertheless, the results of the current study show that tidal energy is clearly a major contributor to diapycnal mixing. Why, therefore, was the mixing not apparent in the microstructure observations described at the beginning of this chapter? The answer lies in the highly localised nature of tidal mixing hotspots. A comparison of the locations of the observations with the spatial distribution of tidal conversion rates, Figure 3.3, shows that while the observations appear to give wide coverage of the Arctic basin, the vast majority of them lie outside areas of enhanced tidal conversion. In addition, the sparsity of temporal sampling at most stations probably means that even where measurements were made in locations where elevated conversion is predicted, the effect, which is expected to be highly temporally variable, was missed. In order to constrain more tightly the contribution that tidal energy makes to diapycnal mixing, longer time series of real mixing rates, and the water classes being mixed, in known tidal hotspots would be highly beneficial.

Given the highly localised nature of tidally-driven mixing revealed by this study, if future changes to the distribution of tidal mixing across water masses are to be

predicted, a good understanding of the likely response of ocean stratification to changing conditions is required. In the next chapter, we investigate the effect of changing freshwater input to the Arctic Ocean.

Chapter 4

Arctic Ocean freshwater: transient response to increasing inflows

4.1 Introduction

The earlier chapters have emphasised the importance of the stratification of the Arctic Ocean in determining the influence that the Ocean has in transforming the water masses that enter and then exit to rejoin the North Atlantic circulation once more. There is a need for an improved understanding of how it will be affected by the changing Arctic climate, not least because of its potential impact on the global circulation through increased freshening of waters exported to deep water formation areas such as the Labrador Sea (Kattsov and Walsh, 2000; Yang et al., 2016).

We recall from Chapter 1 that the influence of winds on freshwater storage and export has received much recent attention (e.g. Proshutinsky et al. (2009), Marshall et al. (2017), Johnson et al. (2018), Meneghello et al. (2017)), but the part played by freshwater input less so. Global warming, which amplifies the hydrological cycle and decreases the Arctic sea-ice export (Held and Soden, 2006; Haine et al., 2015), can increase the freshwater input to the Arctic Ocean essentially without any change in the time-mean atmospheric circulation. Model simulations (Vavrus et al., 2012) indicate that the Arctic is likely to become warmer and wetter over the Twenty-first Century, with sea ice volumes expected to decline considerably. Projections for increases in annual precipitation over the century range from somewhat over a third (Vavrus et al., 2012) to more than a half (Kattsov et al., 2007), although Bintanja and Selten (2014) find that the increases are due at least as much to increases in local evaporation caused by sea ice retreat as to enhanced atmospheric moisture transport from lower latitudes. Since the largest changes in precipitation are projected to occur over land rather than

sea (Vavrus et al., 2012), increases in freshwater input to the ocean from river runoff are likely to be important. We focus in this chapter, therefore, on the effect on Arctic Ocean stratification of the predicted increases in input of freshwater from river runoff and precipitation.

Previous studies (Pemberton et al., 2014; Pemberton and Nilsson, 2016; Nummelin et al., 2016) have considered the long-term response of the ocean to changes in forcing. For that reason, we focus here on the transient response: we draw on the "climate response function" (CRF) framework described by Marshall et al. (2017), using simulations from a coupled ice-ocean GCM to investigate the relationship between changes in freshwater input to the ocean and the response of the ocean in terms of storage and export of freshwater. The rationale for the CRF methodology is that if the transient response (the CRF) of an observable to a Heaviside step function forcing is known, the CRF may then be convolved with any more realistic time history of forcing to determine a predicted linear response for that observable. We take as our observables here the freshwater content (FWC) of the Arctic Ocean in liquid and sea ice form and the export of freshwater through key straits, and apply step change perturbations to the freshwater input from river runoff and precipitation to examine the timescales, pathways and mechanisms governing the likely response of the ocean to changes in freshwater input.

4.2 A conceptual model for rotationally-controlled export

Theoretical predictions of the ocean response to changes in freshwater forcing may be made through consideration of a simple conceptual model such as that described by Stigebrandt (1981), Nilsson and Walin (2010) and Rudels (2010). The version we adopt here represents the Arctic Ocean as stratified by salinity into two layers separated by a halocline at constant depth H: a fresher, upper layer of salinity S_1 above the halocline, and a layer of Atlantic Water with salinity S_A below.

Outflow from the upper layer of the basin is assumed to be geostrophically controlled, and is represented by a volume flux M. A flux F_{met} of freshwater enters the upper layer through river runoff or net precipitation (precipitation minus evaporation), and a flux M_B of Pacific Water of salinity S_B enters through the Bering Strait. A flux M_A of Atlantic Water is entrained into the upper layer from below by mixing. The horizontal surface area of the basin is A.

The volume budget for the upper layer is

$$A\frac{dH}{dt} = -M + M_A + M_B + F_{met} \tag{4.1}$$

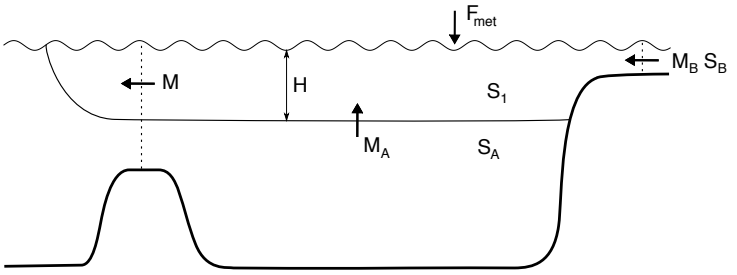

FIGURE 4.1: Sketch of the two-layer conceptual model. H is the depth of the halocline separating the two layers, S_A the salinity of the lower layer and S_1 the salinity of the upper layer. M_B is the volume flux of water entering through the Bering Strait, and S_B its salinity. F_{met} is the influx of meteoric freshwater from river runoff and net precipitation, M_A the volume flux of water entrained from the lower layer to the upper by mixing, and M the volume flux of outflow.

while the salinity budget is

$$A\frac{d(S_1 H)}{dt} = -MS_1 + M_A S_A + M_B S_B \tag{4.2}$$

By dividing Eq. 4.2 by S_A, which we assume to be constant, and subtracting from Eq. 4.1 we obtain

$$A\frac{dH_F}{dt} = -M\frac{\Delta S}{S_A} + M_B(1 - \frac{S_B}{S_A}) + F_{met} \tag{4.3}$$

where $\Delta S \equiv S_A - S_1$ and freshwater height is defined by analogy with Eq. 4.12 as $H_F \equiv (\frac{S_A - S_1}{S_A})H$.

Assuming that the outflow from the Arctic Ocean is in geostrophic balance (i.e., that the exit strait is wide compared to the first Rossby radius) allows us to use the relation for volume transport derived by Werenskiold (1935):

$$M = \frac{\beta \Delta S g H^2}{2f} \tag{4.4}$$

where β is the haline expansion coefficient, g the acceleration due to gravity and f the Coriolis parameter. Note that we have ignored any density difference due to difference in the temperatures of inflowing Atlantic Water and outflow water. Substituting into Eq. 4.3 and defining $F \equiv M_B(1 - \frac{S_B}{S_A}) + F_{met}$ yields

$$A\frac{dH_F}{dt} = -\frac{\beta g S_A {H_F}^2}{2f} + F \tag{4.5}$$

Now consider the effect of a perturbation, ΔF, in freshwater input, leading to an anomaly, ΔH_F, in freshwater height. Eq. 4.5 as applied to the perturbed state becomes

$$A\frac{d(H_F+\Delta H_F)}{dt} = -\frac{\beta g S_A (H_F+\Delta H_F)^2}{2f} + F + \Delta F \tag{4.6}$$

We assume that if the perturbation is small, the resultant anomaly will also be so: $H_F \gg \Delta H_F$, so that

$$(H_F+\Delta H_F)^2 \approx {H_F}^2 + 2H_F\Delta H_F \tag{4.7}$$

Linearising Eq. 4.6 accordingly, and subtracting Eq. 4.5, we have

$$\frac{d\Delta H_F}{dt} = -\frac{\beta g S_A H_F \Delta H_F}{Af} + \frac{\Delta F}{A} \tag{4.8}$$

which has solution

$$\Delta H_F = \frac{f\Delta F}{\beta g S_A H_F} + (const.) \times e^{-\frac{\beta g S_A H_F t}{Af}} \tag{4.9}$$

The prediction of the conceptual model is therefore an exponential evolution of response to perturbation of freshwater input with timescale

$$\tau = \frac{Af}{\beta g S_A H_F} \tag{4.10}$$

Inserting typical values for the Arctic
($\beta = 8\times10^{-4}\mathrm{m^{-1}s^{-1}}, f = 1.4\times10^{-4}$ s^{-1}, $A = 9\times10^{12}$ m^2, $g = 10$ m s^{-2}, $S_A = 35.0$)
into this expression, and estimating H_F by dividing a freshwater volume of
8×10^4 km^3 from Pemberton and Nilsson (2016) by A, gives a predicted timescale of 16 years. Note that in using the relation for geostrophic volume transport in Equation 4.4 in similar analyses, Stigebrandt (1981) and Rudels (2010) have included multiplication factors of between 2 and 3 to allow for the fact that more than one strait drains the Arctic Ocean. To do so here would reduce the calculated timescale proportionately.

Alternatively, from the steady state version of Eq. 4.5, the timescale in Eq. 4.10 may be written as

$$\tau = \frac{AH_F}{2F} = \frac{1}{2} \times \frac{FWC}{\text{Net freshwater supply}} \tag{4.11}$$

(The factor of a half derives from the assumption that outflow from the Arctic is governed by geostrophy.) An increase in H_F increases both the volume export and the salinity export anomaly, which yields a shorter adjustment timescale. Adopting estimates of net freshwater input from meteoric sources and from Bering Strait inflow from Pemberton and Nilsson (2016) leads to an alternative predicted timescale of 12 years.

We compare these predictions with the response seen in experiments performed using a general circulation model, and investigate factors that might lead to any departure from the predictions of the conceptual model.

4.3 Method

4.3.1 General circulation model

In this study we use a coupled ice-ocean model, the Massachusetts Institute of Technology general circulation model (MITgcm), in a regional configuration covering the Arctic Ocean and parts of the North Atlantic and North Pacific oceans north of ∼55°N. The horizontal grid spacing within the model domain, which is shown in Figure 4.2, is approximately 18 km, and the model grid has 50 vertical layers with thickness ranging from 10 m at the surface to approximately 450 m for the deepest layer. Further details of the model setup are given in Pemberton and Nilsson (2016), and the model parameters employed are as described in Nguyen et al. (2011).

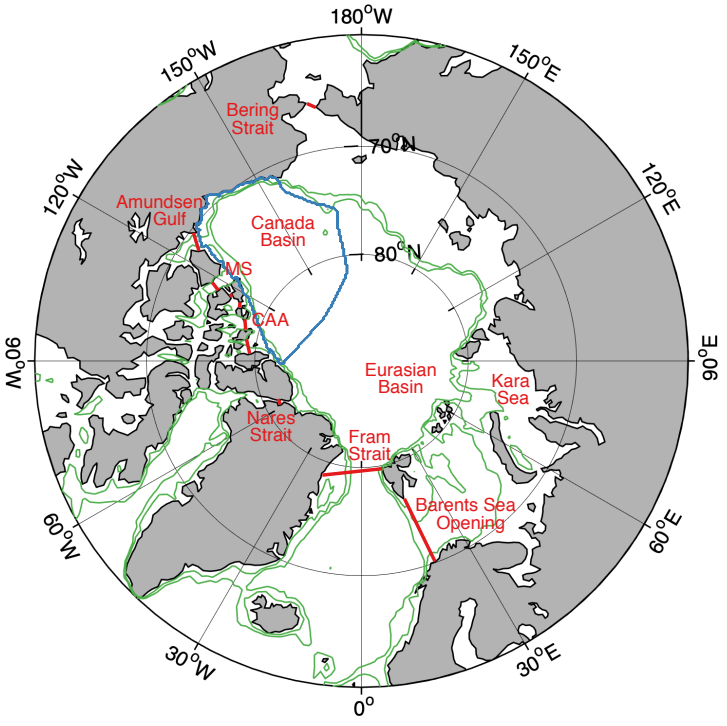

FIGURE 4.2: Map of the model domain showing, in red, the boundaries of the region within which perturbations of surface freshwater input were made (MS: McClure Strait, CAA: Canadian Arctic Archipelago, NS: Nares Strait). The 200 m and 500 m depth contours are shown in green. The blue line indicates the limitation of the Canada Basin area referred to in Figure 4.7.

4.3.2 Simulations

Ocean forcing for the majority of the simulations described here is provided by the Japanese 25-year Reanalysis (JRA-25) (Onogi et al., 2007), which covers the period 1979-2004, extended for a further nine years to 2013 using operational analysis from the same model system. For a small number of additional simulations the model was instead forced with a repeating annual cycle of atmospheric forcing (the Co-ordinated Ocean-Ice Reference Experiments (CORE) II corrected normal year forcing (Griffies et al., 2009)). For river runoff data we use a monthly climatology derived from Arctic Runoff Database raw data and adjusted to account for ungauged river flows, as described in Nguyen et al. (2011). The model was initialised for each simulation using sea ice conditions from the Polar Science Center's GIOMAS data set (Zhang and Rothrock, 2003) and ocean conditions from the World Ocean Atlas 2005.

The model was first run for 35 years in a control simulation, using the forcing described above to represent the current state of the Arctic. To test the response of the ocean to a step change in freshwater input, further simulations were then run in which river runoff or precipitation was increased or decreased by a fixed proportion[1] of the control forcing for the duration of the simulation. The larger increases are greater than those expected to be seen in the real future Arctic, but are included in the suite of simulations to test the linearity of the response. Evaporation and sea ice formation and melt were not perturbed directly through forcing, but evolved during the simulations in response to the perturbation of runoff or precipitation.

For each simulation, monthly means of freshwater height (H_F) and liquid freshwater content (FWC) were calculated:

$$H_F(x,y,t) = \int_{-H_0}^{0} \frac{S_{ref} - S(x,y,z,t)}{S_{ref}} \, \mathrm{d}z \tag{4.12}$$

$$FWC(t) = \int_A H_F(x,y,t) \, \mathrm{d}A \tag{4.13}$$

where z is depth, S salinity and A the horizontal area of the basin. The reference salinity, S_{ref}, was taken to be 35.0 g kg^{-1}. The integrations were performed to a depth $-H_0$ of –277 m, indicative of the upper surface of the Atlantic Water layer. Where storage of freshwater in sea ice is discussed, an equivalent FWC has been calculated from stored sea ice volumes assuming a sea ice density of 900 kg m^{-3} and salinity of 6.0 g kg^{-1}.

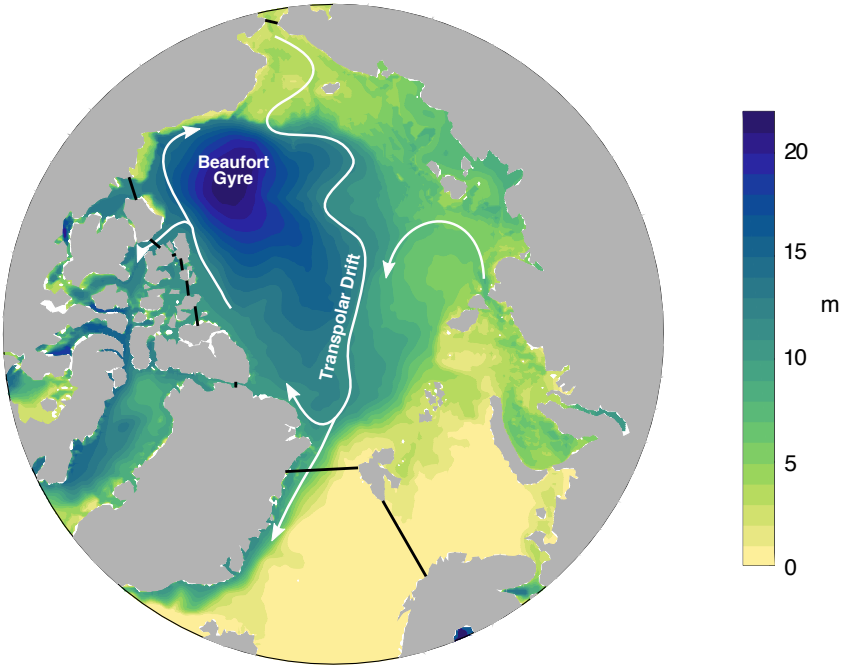

FIGURE 4.3: Time-mean freshwater height, H_F, in metres for the period 2004 to 2013 of the reference simulation, integrated to a depth of –277 m, with $S_{ref} = 35.0$ g kg^{-1}. White arrows indicate major currents in the upper 100 m.

4.4 Results

Typical spatial variability in FWC can be seen in Figure 4.3, which shows mean depth-integrated freshwater height, H_F, for the final ten years of the control simulation. Notably, the concentration of freshwater in the Canada Basin, and in particular in the region occupied by the Beaufort Gyre, is clearly visible.

4.4.1 Reference simulation

The evolution of liquid FWC for the reference simulation over the simulation period is shown in Figure 4.4. Annual mean volumes range from around 75 $\times$ 10^3 km^3 to around 85 $\times$ 10^3 km^3 over the 35 year period. There is a marked seasonal cycle of amplitude around 7 $\times$ 10^3 km^3, or about 9% of the mean volume, with liquid FWC reaching a seasonal maximum in September/October and minimum in May/June of each year; we attribute this to the seasonal storage of freshwater in sea ice.

As has been discussed briefly by Pemberton and Nilsson (2016), we also note significant variability in FWC over decadal scales. The annual mean volume is at the upper end of its range at the beginning of the simulation period and remains

[1] –30% to +100% for runoff, –30% or +30% for precipitation

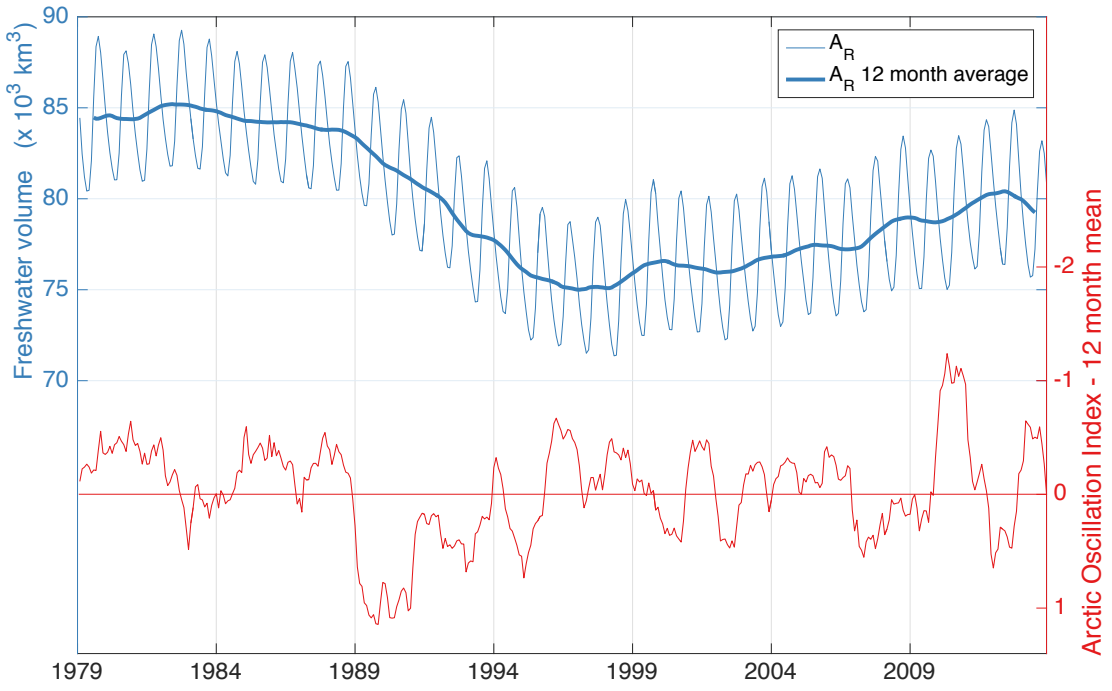

FIGURE 4.4: In blue, time evolution of FWC in the reference simulation; monthly mean FWC is shown by the thinner blue line, while the heavier line denotes a 12 month rolling mean. In red, 12 month rolling mean of the Arctic Oscillation Index. Note that the right hand axis is reversed.

reasonably steady for the first decade, then drops by around 10×10^3 km^3 between the years 1989 and 1997 before recovering somewhat towards the end of the period. The decline in volume from 1989 onwards coincides with a period in which the Arctic Oscillation Index (Thompson and Wallace, 1998) is positive, and is consistent with the observed release of freshwater from the Beaufort Gyre (e.g. Proshutinsky et al. (2009); Morison et al. (2012); Haine et al. (2015)), consequent on changing wind patterns. It is likely that a large proportion of the freshwater discharged from the Gyre in this period has subsequently been exported from the Arctic.

4.4.2 Runoff

Figure 4.5a shows the evolving anomaly in liquid freshwater content relative to the control for the series of simulations involving step-change perturbation of river runoff. Values for the anomalies are normalised by the sign and scale of perturbation to a 30% increase, that is to say, $\Delta FWC = (FWC_{\text{expt}} - FWC_{\text{control}}) \times (30\%/\text{percentage increase in runoff})$. As expected, a decrease in runoff results in a negative anomaly in freshwater content compared to the control, while increases generate positive anomalies. Although there is some asymmetry between negative and positive perturbation – the reduction in runoff gives rise to a larger proportionate anomaly,

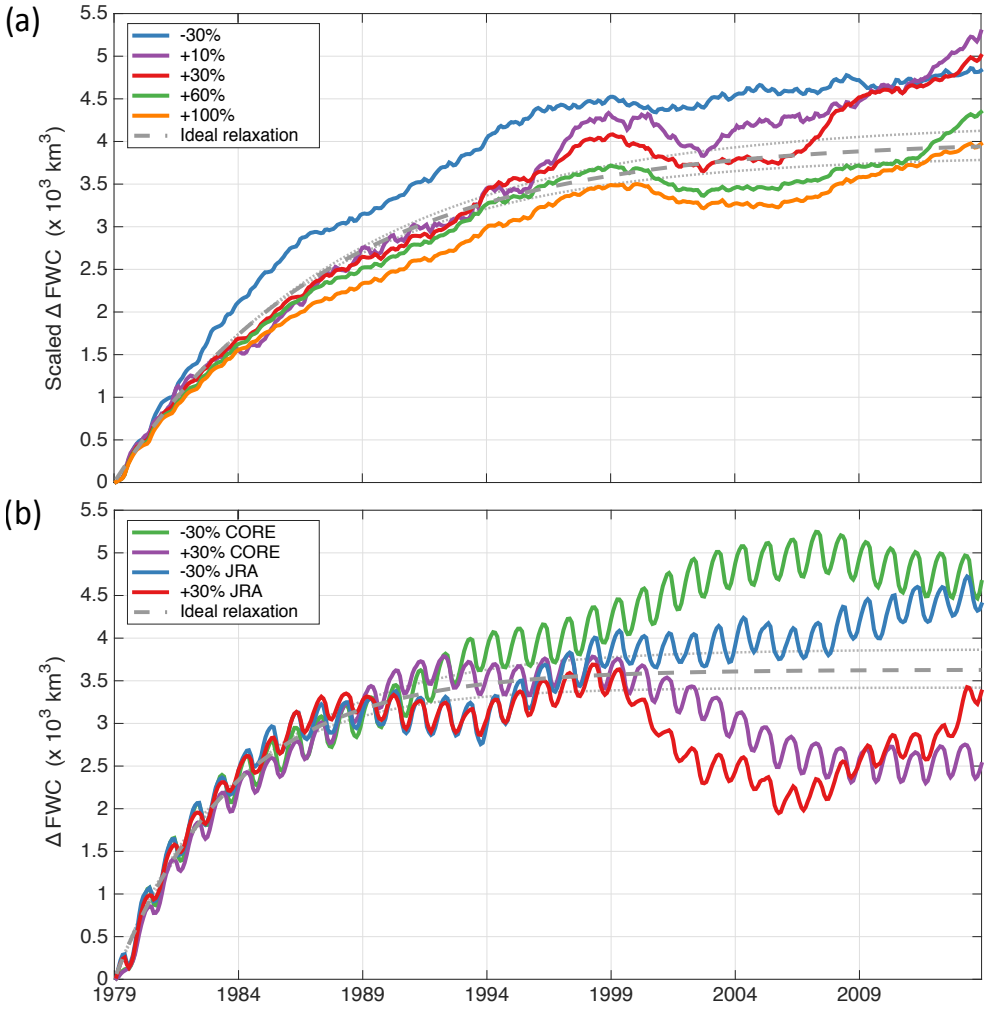

FIGURE 4.5: Time evolution of (a) anomaly of FWC with respect to the reference simulation in the simulations involving perturbation of river runoff; and (b) anomaly of FWC with respect to the reference simulation in the simulations involving perturbation of precipitation. In (a), the solid lines indicate FWC anomalies resulting from runoff perturbations as indicated in the panel, normalised by the proportionate size of the perturbation to be equivalent to a 30% increase. In (b), the blue and red solid lines relate to simulations forced, as with the runoff simulations, with JRA-25 data, while the green and purple lines relate to the equivalent simulations using CORE-II forcing. In each case, the dashed grey lines represent averaged ideal exponential evolutions fitted to the first eight years of the simulations, while the dotted lines indicate averages of the upper and lower bounds of 95% confidence for the fits. Note that for negative simulations the sign of the values has been reversed to allow for ease of comparison with the positive simulations.

especially in the early part of the simulation – for increases in runoff the anomaly is close to proportional in magnitude to the perturbation of freshwater input, even for comparatively large perturbations. This confirms that the response of the system is essentially linear, which is a necessary condition for the validity of the CRF framework. Except in the earliest years of the simulations, when a signal of the strongly seasonal river input can be detected, no annual cycle is apparent in the

anomalies, indicating that perturbation of freshwater input through river runoff has negligible effect on the seasonal storage of freshwater in sea ice.

The 35 year period of integration is not sufficiently long for a new equilibrium to be reached in each simulation, but we see that the adjustment is to first order exponential with mean timescale[2] of 8.9 ± 0.6 years, as shown by the grey dashed line in Figure 4.5a. We note that the exponential form of the response is apparent even in the first 5 years for the simulations involving increased runoff, suggesting that export of freshwater from the Arctic is enhanced sooner than would be implied purely by the advection of extra freshwater from river outflows to the main export straits; had advection been the only control mechanism, a linear increase in FWC anomaly would have been expected in the early years.

For the response to variation of freshwater input to exhibit the linearity predicted by the conceptual model of Stigebrandt (1981), Nilsson and Walin (2010) and Rudels (2010), we would expect to see direct proportionality between anomaly in FWC and anomaly in export of freshwater as well as proportionality between scale of perturbation of FW input and anomaly in FWC. A comparison for the runoff experiments is shown in Figure 4.6. Initially there is indeed a good linear fit between FWC and export anomalies in both the positive and negative simulations. Further into the experiments, however, the coupling becomes less pronounced and in the final decade especially we see a range of possible export anomalies for a given anomaly in FWC.

4.4.3 Precipitation

An underlying exponential form is also seen in the response to perturbation of precipitation, with simulations involving a decrease and an increase of precipitation by 30% shown by the blue and red lines in Figure 4.5b. The asymmetry between positive and negative perturbations that was seen in the case of river runoff is not present for the precipitation simulations, at least in the first 15 years of the simulation period. In the latter part of the period, however, some decadal-scale variability is seen that is more pronounced than that for runoff and affects the responses to increases and decreases in precipitation differentially. In Figure 4.7a, FWC is shown separately for the Canada Basin, which includes the Beaufort Gyre, and the remainder of the Arctic domain. While a small decrease in the scale of the Arctic-integrated anomalies between 1989 and 1994 is due to decreasing FWC in the Canada Basin, it is apparent that FWC in the remainder of the Arctic is responsible for the larger decline towards the end of the period. This is discussed further below.

[2]Calculated by fitting an exponential curve to anomalies for the first 8 years of the simulations, the period in which freshwater content in the control is relatively stable over interannual timescales and the anomaly signal is strongest.

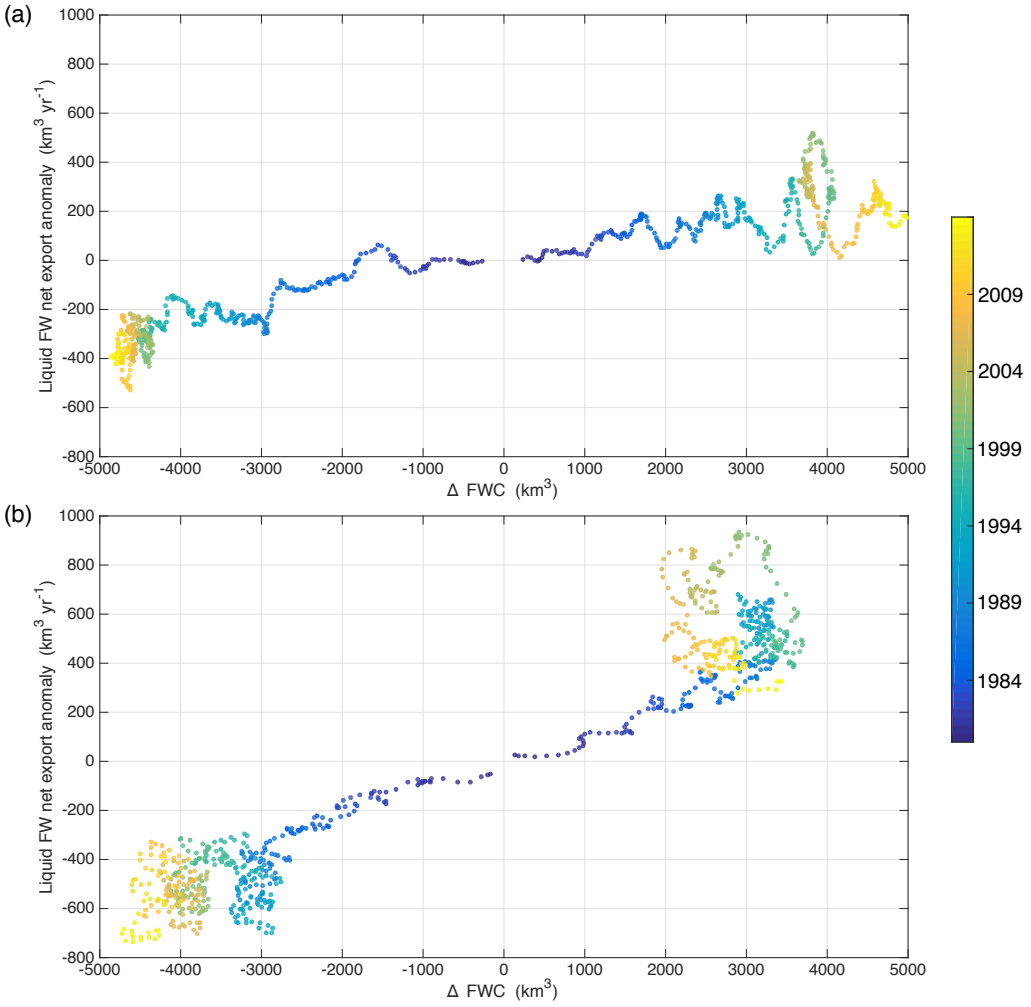

FIGURE 4.6: Anomaly in net export of freshwater as a function of anomaly in liquid FWC for simulations involving a 30% increase and decrease in river runoff. The colour coding shows the evolution of anomalies with time.

A comparison of the results for runoff and precipitation in Figure 4.5 suggests that ΔFWC increases faster in response to an increase in precipitation than to a similar increase in FW flux through river runoff, indicating that a greater proportion of the increased FW input from precipitation is retained in the Arctic, at least initially. A similar exponential fit to the evolution of the anomalies gives a mean adjustment timescale of 4.9 ± 0.5 years. In fact, FW input from runoff is slightly larger than that from precipitation, so we would expect a flatter curve still for precipitation if timescale were independent of source of FW input. A possible explanation is that a significant proportion of the increased precipitation falls in the Barents and Kara Seas, more remote from the major circulation pathways than is outflow from the major rivers of eastern Siberia, and so it takes longer to be advected out of the Arctic domain. We note, however, that the timescale associated with the response to perturbation of precipitation appears more in line with that for negative perturbation of river runoff.

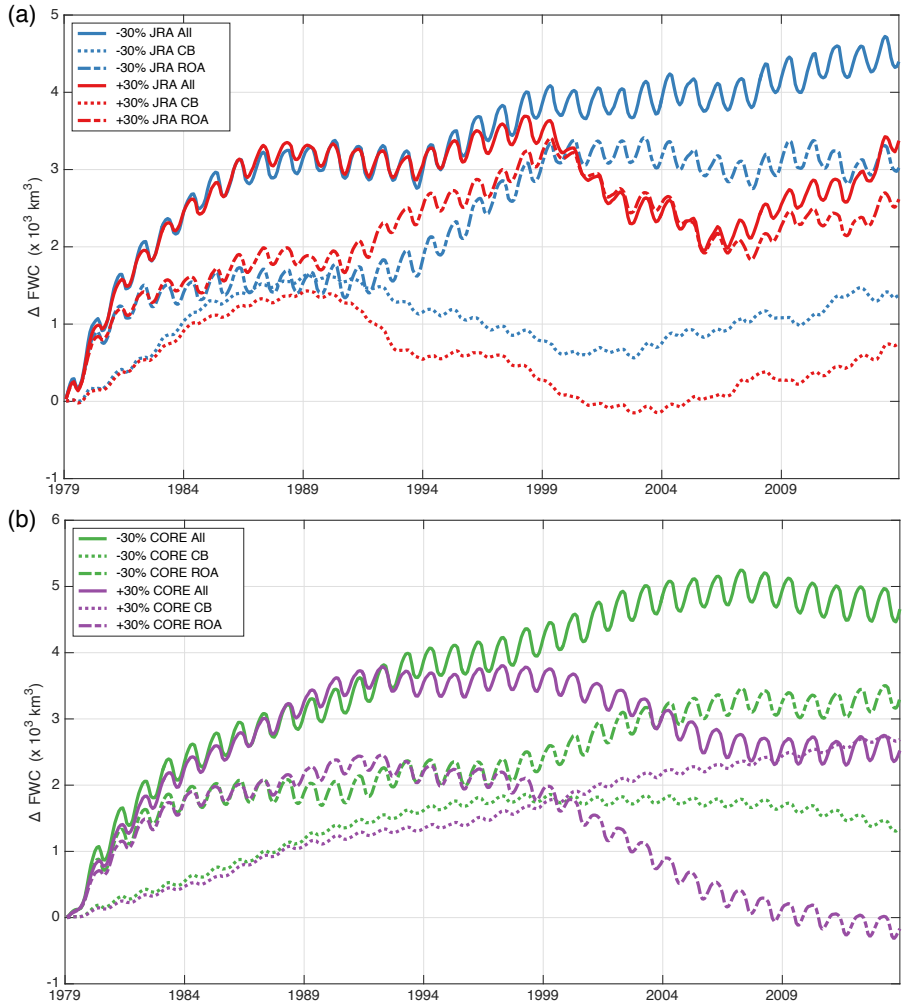

FIGURE 4.7: Anomaly in FWC by basin for the precipitation simulations forced by (a) JRA-25 reanalysis and (b) the CORE-II climatology. The dotted lines relate to the FWC of the Canada Basin (as marked in Figure 4.2 and the dashed lines to the remainder of the Arctic. The solid lines show the sum for the whole domain. The results for the negative simulations are reversed.

In contrast to the runoff experiments, some residual seasonal cycle is evident in the precipitation anomalies which is accompanied by compensating seasonality in anomalies in freshwater storage in sea ice (see Figure 4.8). The seasonal cycle in the anomalies in liquid FWC is in antiphase with the cycle in the absolute freshwater volumes in the reference case and experiments, indicating that increasing precipitation *depresses* the seasonal cycle, and vice versa, which is consistent with observations in the literature (Notz, 2009) that increasing snowfall over sea ice increases the thermal insulation provided by the ice, inhibiting the exchange of heat between ocean and atmosphere and thus the annual freeze and melt of sea ice. The amplitude of the residual seasonal cycle seen in the freshwater anomalies is slightly greater for negative perturbation of precipitation than for positive - of the order of 500 km^3 as opposed to 400 km^3 - as we would expect to see if changing snow cover is the cause, since a

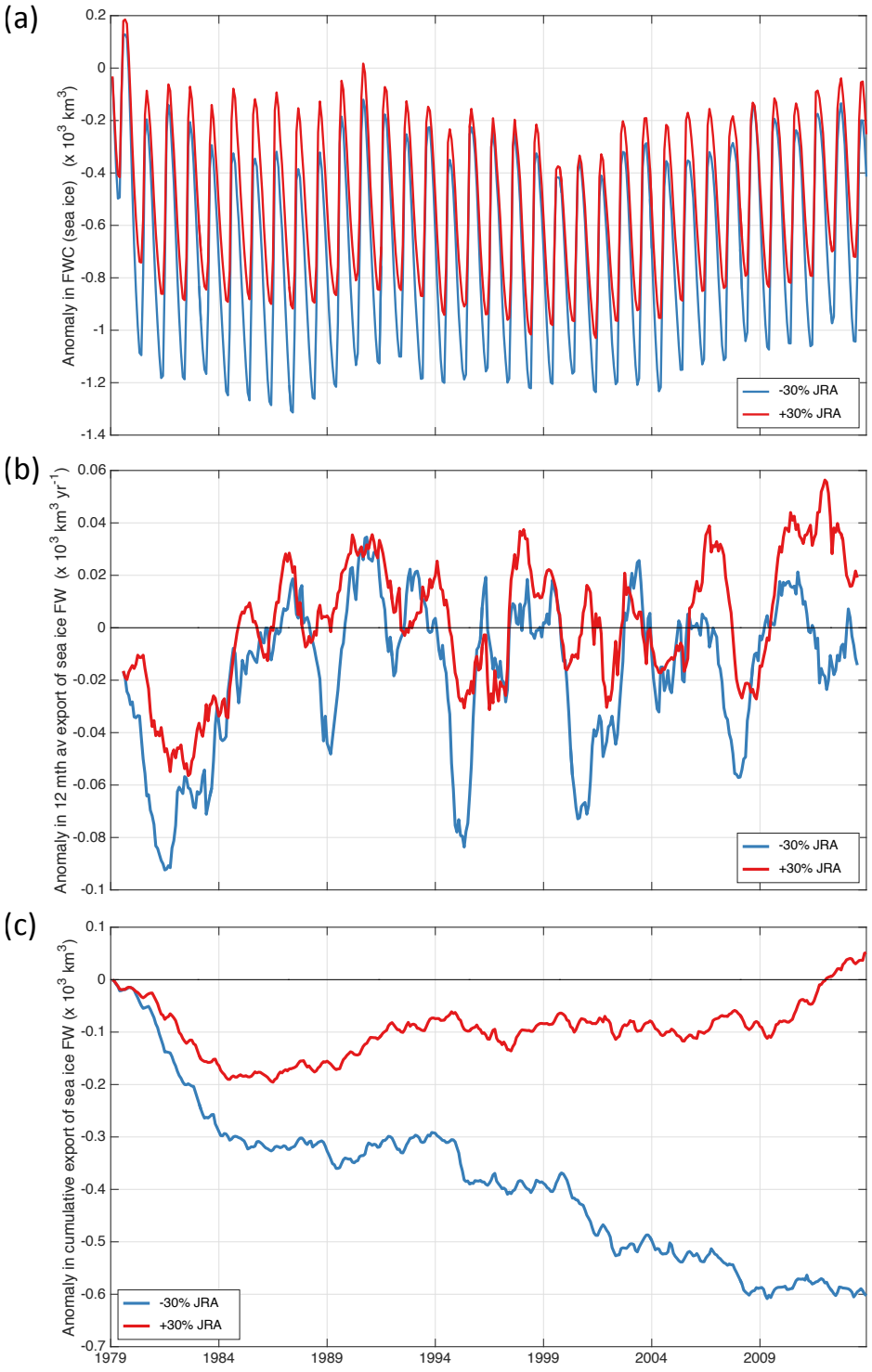

FIGURE 4.8: (a) Anomaly in equivalent FWC of sea ice for the JRA-forced precipitation simulations. (b) 12 month rolling mean of anomaly in net export of sea ice FWC equivalent through those straits marked in Figure 4.2. (c) As (b), but time-integrated. Results for the negative simulations are reversed in all cases.

reduction in snowfall would be expected to produce a greater proportionate change in overall snow thickness than an increase of the same magnitude.

In the latter half of the period, as mentioned above, the response to perturbation of precipitation is less clean than that to changing runoff. We note that the more pronounced variability over interannual and decadal timescales apparent in the evolution of anomaly in liquid FWC is only in small part accounted for by variation in annual mean sea ice freshwater storage. Since changes in the storage of freshwater in the Beaufort Gyre are known to be associated with variation in atmospheric circulation over these timescales [several authors, summarised by Haine et al. (2015)], we have investigated whether the variability might derive from variability in the wind forcing by re-running the precipitation simulations with a climatological forcing in place of the more realistic JRA-25 reanalysis to eliminate the effects of changing wind patterns. Anomalies in FWC from these further simulations are shown in green and purple in Figures 4.5b and 4.7b. Some of the variability is now absent, but a notable divergence in behaviour in the positive and negative simulations is still apparent over the period 1998 to 2002. This is concentrated in the Eurasian Basin. It reflects enhanced export of freshwater through the Fram Strait in the simulation involving increased precipitation, and coincides with the appearance of a region of enhanced freshwater height, H_F, to the north of Greenland and just upstream of the Fram Strait that is not reproduced as a strong reduction in H_F in the corresponding freshwater decrease experiments.

4.5 Discussion

A necessary condition for the applicability of the CRF methodology is a linear relationship between applied forcing and observed response. The results of the simulations presented in Section 4.4 demonstrate that this condition is well met, at least for the runoff simulations. We find that the CRF for the response of Arctic Ocean freshwater content to a perturbation of river runoff approximates to an exponential equilibration with a timescale of around 10 years. This figure accords with the bulk residence time ($\tau = FWC/F$) for Eurasian runoff of 10 years determined by Pemberton et al. (2014) using tracer simulations, and is in line with the comparator studies they quote, including Jahn et al. (2010).

The first-order exponential nature of the response is also in agreement with the prediction of the two-layer geostrophically-controlled model described in Section 4.2, and the 10 year timescale of the CRF calculated from our simulations corresponds reasonably well to the 16 year estimate implied by the conceptual model. Haine et al. (2015) found that such a model had only limited skill in explaining observed changes in Arctic Ocean FWC. Nevertheless, their results - and those we report here (see Figure 4.4) - suggest that the observed changes were driven by wind patterns rather than by

changes to freshwater input. Consequently, the observations could be expected to reflect the forcing history of winds over the Arctic and their associated CRFs in addition to any effects of changing freshwater forcing represented by the conceptual model, which would explain why the model, which does not include wind effects, was found not to offer a good representation of observed FWC. The current simulations focus on isolating CRFs for freshwater input.

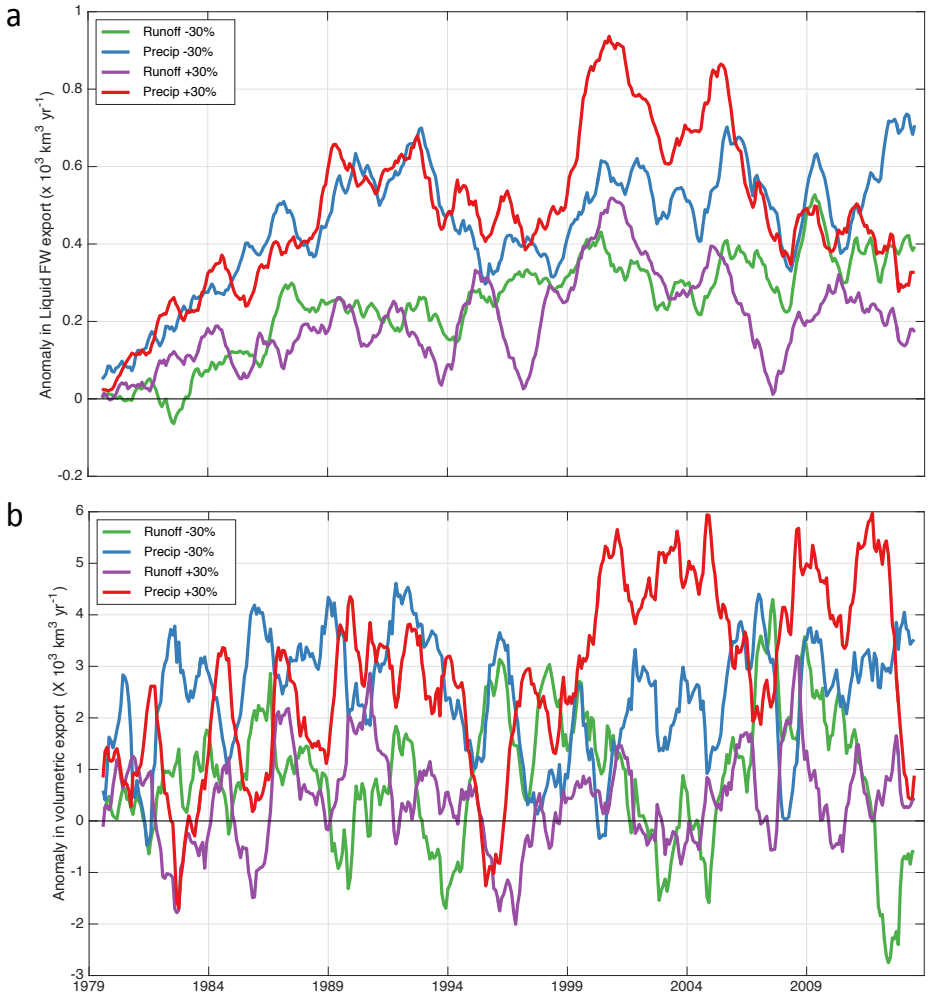

FIGURE 4.9: (a) Anomaly in net export through the straits shown in Figure 4.2 of liquid freshwater for the JRA-forced runoff and precipitation simulations, as marked. (b) As (a), but for net volumetric exports. Results for the negative simulations are reversed in all cases.

It is interesting to note how quickly the first effects of changed freshwater input are seen in the anomalies of freshwater export (Figure 4.9). A purely exponential CRF would require freshwater export to respond immediately to changes in input, but in the real ocean we would of course expect a delay to allow a signal to be transmitted from the main input regions - the Siberian and Mackenzie River outflows in the case of runoff - to the export straits many hundreds of kilometres away. Estimates of the minimum time required for water of altered salinity to be advected from the Siberian

shelf to the Fram Strait, made by tracking salinity anomalies in the model along the Transpolar Drift, the most direct route and one along which higher than average current speeds are typically seen (see for example Pemberton and Nilsson (2016) Figure 3), average around four years. Inspection of the transient FWC anomalies shown in Figure 4.5a, however, reveals some curvature, implying that freshwater exports start to respond and partially offset the perturbation of freshwater input, within the first four years of the simulations. An early evolution of export anomalies is also apparent in Figure 4.6, particularly for the simulation involving increasing runoff. It is not possible to attribute these early export anomalies conclusively to a response to changing freshwater input, in view of the natural variability in exports caused by factors such as winds in the vicinity of the export straits, but our results do provide an indication of a response in exports triggered faster than an advection signal could be transmitted. Enhancements in freshwater export can have two possible causes: either anomalously low salinity in the water flowing out through the straits, or an increase in the volumetric export of water of unchanged salinity; the first cannot explain the early changes in export, but the second could, if changes in freshwater input in the basin generated a dynamical signal which changed the outflow velocity at the borders of the Arctic. This might propagate as a baroclinic Kelvin wave. Assuming a mode 1 baroclinic Rossby radius, a_1, of 10 km (Nurser and Bacon, 2014) and a Coriolis parameter, f, of 1.4×10^{-4} s^{-1}, the propagation speed of such a wave, given by $c_1 = a_1 f$ (Gill, 1982), would be 1.4 m s^{-1}, allowing it to circumnavigate the Arctic basin in approximately 60 days.

We turn now to consideration of possible causes of the deviations from the first order exponential form seen in the CRFs. While the underlying form of the transient responses to changing runoff and precipitation is the same, there are also some differences which could offer some pointers to the processes responsible. A seasonality signal in FWC anomaly due to changes to sea ice growth is apparent only in the precipitation simulations, which exhibit more marked variability over decadal scales than those involving perturbation of runoff. Could it be, therefore, that variability in liquid freshwater storage is linked to changing storage of freshwater in sea ice form? Analysis of the sea ice volumes in the precipitation experiments shown in Figure 4.8 demonstrates that this is not the case. After rapid adjustment over the first two to three years, anomalies in seasonally-averaged sea ice freshwater storage remain largely constant over the simulation period, and the annual mean anomalies do not increase at any point beyond 700 km^3 in magnitude for an increase in precipitation and 800 km^3 for a decrease. This is some way short of the 1300 km^3 by which the anomaly in liquid freshwater storage decreases between 1999 and 2006 in the simulation of increasing precipitation, indicating that the temporary shortfall in liquid freshwater cannot be accounted for by storage in sea ice.

The influence of changing wind patterns on FWC in the control simulation (Figure

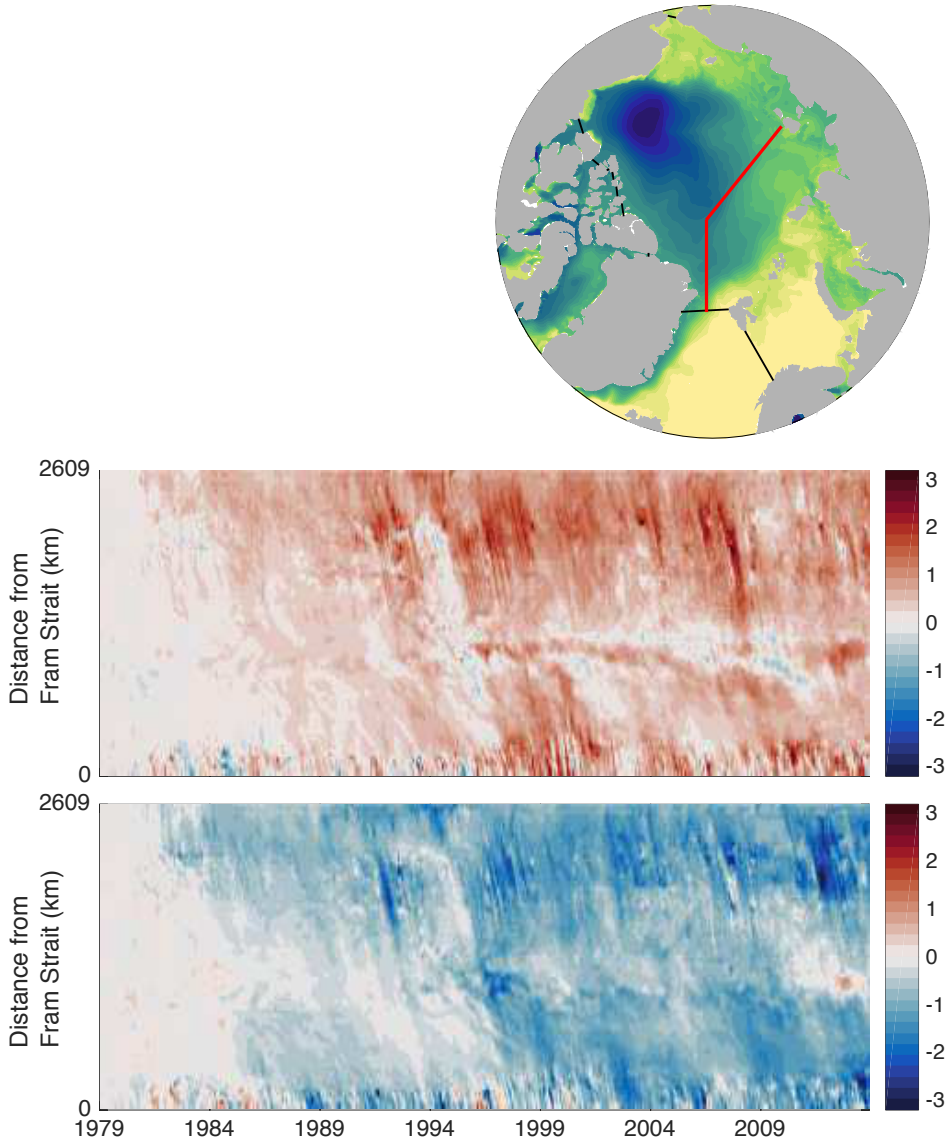

FIGURE 4.10: Hofmöller plots of anomaly in H_F in m for the 30% runoff simulations. The y-axis represents distance from the Fram Strait along the transect marked in the map at upper right.

4.4) leads us to consider whether, alternatively, the variation in freshwater anomalies could be wind-driven. We note that the greatest deviations from exponential form between 1999 and 2009 coincide with the period of recovery of reference case FWC following its rapid wind-driven discharge in the previous decade. However, comparison of our results from the different precipitation simulations indicates that winds are not the cause of the variability either. The fact that the same pronounced departure from an essentially exponential evolution is apparent after 15-20 years in the simulations forced with the repeating CORE-II climatological wind fields as well as those employing the more realistic JRA-25 forcing demonstrates that an effect other than wind variability must be the cause.

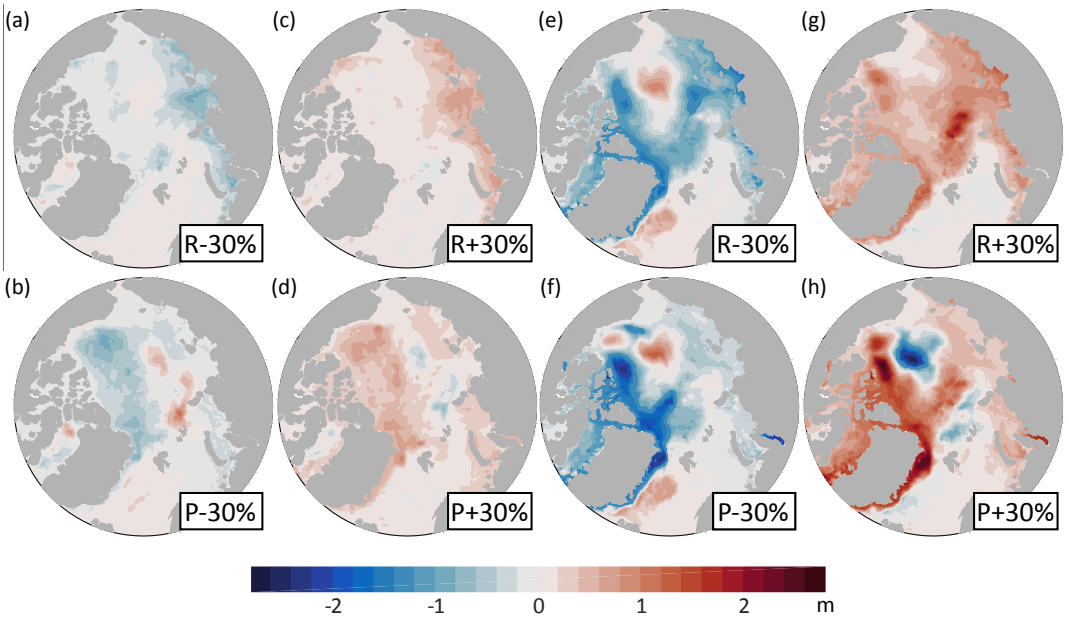

FIGURE 4.11: Anomaly in freshwater height for simulations involving increases and decreases of river runoff and precipitation of 30%. (a) to (d) show time means for the period 1979 - 1988; (e) to (h) show time means for the period 2004 - 2013. (Colourmap from cmocean (Thyng et al., 2016).)

We have already noted in Section 4.4.3 above that enhanced export of freshwater through the Fram Strait in the positive precipitation experiment during the period 1998 to 2002 was accompanied by the appearance of a region of enhanced H_F just upstream of the strait. This leads us to consider a final hypothesis for the cause of the second order form of the FWC responses, which is suggestive of a secondary timescale: that it is due to the advection of salinity anomalies from source regions to the borders of the Arctic, where they lead to variability in freshwater export. Some further insight may be gained by inspection of the evolving spatial variability in FWC. Figure 4.11 shows time mean freshwater height anomaly for the first (1979 - 1988) and last (2004 - 2013) decades of the JRA-25-forced simulations. Pemberton and Nilsson (2016) noted both the profound effect on freshwater height north of the CAA and Greenland, and the changes in the circulation and location of the Beaufort Gyre, that perturbation of freshwater input could generate. We observe from Figure 4.11 that these effects arise with differing timescales.

In the early stages of the runoff simulations, we see an increase and decrease in freshwater height in response to increasing and decreasing runoff respectively that are largely confined to the Siberian shelves where the bulk of the freshwater input occurs, after which a salinity signal is seen to spread along the main advection pathways. Marshall et al. (2017) had observed that the FWC of the Beaufort Gyre is insensitive to an increase in river runoff three times the size of the largest we have introduced

here. Their conclusion, that most of the extra freshwater, rather than being accumulated in the Gyre, is transported via the Transpolar Drift to the Fram and Canadian straits, is lent weight by our simulation (Figure 4.11(g)) showing that ultimately much of the increase in freshwater height is seen upstream of these straits. In contrast, in computing the CRF for the FWC of the Arctic basin as a whole, we find that sufficient freshwater is retained in other areas of the Arctic Ocean not subject to large variability in storage conditions to show exponential relaxation towards a new, elevated level of FWC.

This finding has implications for predictions of the effect on freshwater storage of future changes to wind patterns, either those driving Ekman pumping in the Beaufort Gyre region or those in the vicinity of the Arctic straits which control the local currents exporting freshwater from the Arctic. If the redistribution of freshwater away from the Gyre and towards the main export straits that we envisage will be brought about by increased freshwater input is not taken into account, the potential effect of changing winds on freshwater exports may not be captured fully.

As an aside, the reader may recall that the largest future change of the Arctic Ocean freshwater budget is reduced sea ice export (Holland et al., 2007). Although we have not perturbed sea ice formation directly in the current simulations, we note that observed reduction in new ice formation has a large signal over the Siberian shelf (Comiso, 2011). We would expect, therefore, that the response in terms of spatial distribution of liquid freshwater to declining sea ice formation will have a footprint similar to that of river runoff.

In contrast to runoff, in the precipitation simulations, although anomalies in freshwater height are seen in the early years in the Barents and Kara Seas where precipitation is highest and the perturbations thus have greatest magnitude, more pronounced changes are apparent across much of the Canada Basin and the region to the north of Greenland, areas where less precipitation occurs but sea ice tends to be thickest. This accords with the finding of Pemberton and Nilsson (2016) that a decrease in precipitation ultimately leads to an increase in sea ice thickness north of Greenland. Accumulation of salinity anomalies in these regions would be expected to lead to the variability in freshwater exports visible in Figure 4.6 as they are advected through the various export straits just to the south, and can thus explain several of the features seen in the CRFs, including the slight decline in FWC anomalies after 10-15 years in Figure 4.5b and the more pronounced declines in the latter part of the simulation period.

A further potential source of complexity in the response is the timescale associated with alteration of the major Arctic circulation pathways. Pemberton and Nilsson (2016) found that increasing freshwater input leads to a decrease in the strength of the Beaufort Gyre circulation and a shift in export from the CAA to the Fram Strait; we

see from Figure 4.11 that indications of these changes in the form of altered freshwater storage in the region of the Gyre are apparent only in the later years of the simulations.

4.6 Conclusions

We have investigated here for the first time the transient response of freshwater content in the Arctic Ocean to changing freshwater input, comparing the effects of perturbation of river runoff and precipitation. We offer a CRF for river runoff, which takes the form of a simple exponential relaxation with a timescale of approximately ten years. This accords with the predictions of a simple two-layer conceptual model for rotationally-controlled export of freshwater. Although to first order sharing the exponential form of the runoff response, albeit with a timescale closer to 5 years, the response to changing precipitation shows additional complexity consistent with a secondary timescale. We suggest that this is due in part to the greater importance of ocean-ice interactions in the precipitation case; these give rise to localised salinity anomalies which cause variability in freshwater exports when they are advected through the straits at the boundaries of the Arctic. Our results suggest that the fate of enhanced freshwater input to the Arctic and the proportion of extra freshwater stored within the Arctic rather than being discharged immediately to the sub-polar seas depends on the mode and footprint of this input. Although river runoff is projected to contribute the greater share of future increases in freshwater input than is precipitation, we find that runoff produces a more predictable response in terms of storage and export of freshwater. In the case of precipitation, a greater proportion of the extra freshwater is found in regions of the Arctic where it is subject to less predictable storage and discharge. In addition, such is the importance of non-linear interactions between the ocean and sea ice in the precipitation response that accurate projections of the effect of future increases in precipitation will require models that can capture ice-ocean interactions well.

Chapter 5

Summary and Conclusions

We summarise here the key findings of the earlier chapters, and then discuss their implications for our understanding of the changing Arctic Ocean and its influence on the global circulation.

5.1 Summary of key results

Previous studies have suggested that the Arctic Ocean supports a double overturning (Eldevik and Nilsen, 2013; Lambert et al., 2016), with some inflowing Atlantic Water made fresher and less dense, and some cooler and denser (Pemberton et al., 2015). However, the hypothesis had not so far been tested with reference to observations. In Chapter 2 we presented the first integrated view of the diapycnal overturning circulation and its drivers in terms of surface buoyancy forcing and interior mixing. We have made use of a quasi-synoptic series of ship-borne and mooring-based hydrographic measurements which together span the straits bounding the Arctic Ocean (Tsubouchi et al., 2012). Taking the Arctic Ocean as a control volume, assuming an advection/ diffusion balance and computing volume and density budgets, we have established that the double overturning does exist. We see a lower limb underpinned by densification through heat loss in the Barents Sea, and an upper limb driven by enhanced levels of diapycnal mixing at the upper surface of the AW layer, which loses density to fresher water coming off the continental shelves. We calculate that of 3.3 Sv of AW entering the Arctic Ocean, 1.8 Sv is made less dense and 1.5 Sv more dense, with the potential density (σ_0) at which the bifurcation occurs and diapycnal volume transport is zero being 1027.75 kg m^{-3}. Our quantified estimates will serve as a baseline for assessing the scale of future change.

The density budgets we have presented suggest that the transformations of water masses are controlled as much by interior mixing as they are by surface buoyancy

fluxes. To balance the budgets, basin-mean turbulent diffusivities of $1.0 - 1.2 \times 10^{-5}$ $m^2\ s^{-1}$ are required across the upper part of the Atlantic Water and Upper Atlantic Water classes that constitute the upper limb of the overturning. These are in line with those given by microstructure observations around the continental slopes and in areas known to be relatively energetic such as the Yermak Plateau, but an order of magnitude higher than those typical of the less turbulent regimes seen in the deeper regions of the Arctic Ocean. The diffusivities indicated for the lower limb are smaller – as low as 3.0×10^{-6} $m^2\ s^{-1}$ towards the base of the AW layer – and potentially indicate that water in this class is less affected by mechanical mixing, or that other physical processes oppose the mixing.

In Chapter 3 we considered the potential source of the energy to drive the upwelling in the upper limb that we infer from density budgets. Over the densities between 26.70 and 27.75 kg m^{-3}, we calculate that an energy input of 1.3 GW is required to overcome stratification through diapycnal mixing. This is not accounted for by double diffusive processes, because these lead instead to downwelling. In previously reported observations of mixing driving enhanced turbulent heat fluxes (Rippeth et al., 2015), turbulent intensity has been seen not to depend on sea ice cover, leading us to conclude that surface stress from winds is also unlikely to be the cause. We have therefore considered whether tides might offer a plausible energy source. Estimates of the rate of conversion of energy from the barotropic tide (Rippeth et al., 2015), integrated over the Arctic basin, are two orders of magnitude higher than the rate of conversion to potential energy required by our estimates of diapycnal mixing. We have investigated whether the spatial distribution of the energy supply is such that it is available to overcome stratification in the areas of the Arctic occupied by water in the relevant density classes. By mapping the estimates of tidal conversion onto the Arctic density field we find that the energy supply is, within the bounds of error, sufficient. We note, however, that the extent to which available energy meets the energy requirement depends quite heavily on the assumed mixing efficiency, indicating that an improved understanding of how mixing efficiency varies according to factors such as turbulent intensity would be beneficial. We cannot conclude from the current study that tidal conversion is the only source of energy for the diapycnal mixing inferred from Chapter 2, but it clearly has the potential to be a major contributor.

We noted that estimates of turbulent mixing intensity derived from previous microstructure observations (Rippeth et al., 2015) were on average an order of magnitude smaller than would be consistent with the turbulent buoyancy fluxes calculated here. A comparison of the locations where the measurements were made with the modelled areas of enhanced rates of tidal energy conversion reveals, however, that few of the observations coincided with the predicted mixing hotspots. The mechanism that Rippeth et al. (2017) propose for tidal conversion suggests that its incidence is heavily dependent on both topography and flow conditions. Consequently,

conversion might be expected to be highly variable both spatially and temporally. There is a need, therefore, for further observations to be made in those locations where tidal conversion is expected to be concentrated in order that the contribution that tidal energy makes to supporting the Arctic Ocean overturning may be better understood. Such measurements will also need to provide sufficient temporal coverage to allow for the variation of internal wave generation over the tidal cycle. Tidal energy has often been dismissed as a major driver of Arctic mixing: we show here that it deserves closer investigation in future.

We investigated the effect of changing freshwater input in Chapter 4. This is an important area of investigation not only because freshwater exported from the Arctic could affect stratification and hence deep convection in the Nordic and Labrador Seas but, as is clear from the work presented here, in consequence of its potential effect on stratification within the Arctic Ocean. Previous studies of controls on Arctic freshwater content have focused on the effect of atmospheric forcing at the expense of freshwater input because it has been assumed that if freshwater input is increased excess freshwater is exported directly from the Arctic (e.g. Marshall et al. (2017)). We have shown here that the picture is more complex. How the Arctic Ocean responds depends on the source of the freshwater input. If it is delivered as runoff from the rivers surrounding the Arctic domain, much of the additional freshwater enters the Transpolar Drift when it leaves the Siberian shelves and does exit the Arctic relatively quickly. The proportion which remains changes the stratification predictably. Freshwater storage within the Ocean adjusts with a timescale of 8.9 $\pm$ 0.6 years. If, on the contrary, the freshwater enters in the form of precipitation, the response timescale is shorter (4.9 $\pm$ 0.5 years) and the response of ocean stratification is more complicated. A higher proportion of freshwater input than is the case with runoff is advected to areas such as the region to the north of Greenland where it may experience complex interactions with sea ice. Because of the formation and subsequent export of salinity anomalies resulting from these interactions, storage within the Arctic Ocean is much more difficult to predict. There has been a tendency in the past to see freshwater as a passive tracer of ocean circulation: our work here shows that it plays a more active role.

5.2 Discussion and implications

How might the picture of Arctic Ocean circulation that we describe here develop in response to the extensive changes that are taking place there? AW inflow is warming (Polyakov et al., 2017). Sea ice cover is thinning and retreating (Comiso, 2011). Freshwater input is increasing (Vavrus et al., 2012; Bintanja and Selten, 2014). All of these changes can be expected to affect ocean stratification. We first consider the lower limb of the overturning. Warmer inflowing AW will need to lose more heat to reach the

same density as the Deep Water currently formed in the Arctic, but atmospheric temperatures in the Arctic are also expected to rise so the temperature differential between the sea surface and atmosphere is not expected to increase in parallel. Since the densification of AW due to heat loss to the atmosphere occurs in the winter, it is concentrated in those regions which are ice-free all year round. Currently, these are confined to the south-western part of the Barents Sea. If, as is expected, the remainder of the Barents Sea becomes ice-free in future, the surface area over which the AW can lose heat will be extended. In addition, our simulations of freshwater input in Chapter 4 suggest that increased precipitation will have the effect of reducing freshwater content in the Nansen Basin, perhaps because the volume of sea ice advected in from other regions and melted there is reduced, which would reduce stratification and facilitate an enhancement in heat loss from the AW.

We turn now to consideration of the upwelling limb of the overturning. As this study shows, this is dependent on highly localised diapycnal mixing, which is probably also bottom-intensified. The barotropic tidal flows which appear ultimately to supply much of the energy that drives the mixing are unlikely to be much changed in the new Arctic, but the particular conditions of stratification which allow for the conversion of energy from the barotropic tide will depend on the stratification at the generation sites. Propagation of the resulting internal waves will in addition be affected by changes in ice cover close to these locations, since internal wave energy is seen to be absorbed in areas covered by ice. The Arctic Front is predicted to retreat northwards in response to warming AW inflow (Polyakov et al., 2017), leading to pronounced changes in stratification in the region comprising the Barents Sea and shelf area north of Svalbard which is thought to contain the major mixing hotspots contributing to the upwelling. If the effect of Arctic change on upwelling of AW is to be predicted with any confidence, a clearer picture is required of where the bulk of the mixing actually takes place.

In conclusion, we note that several physical processes can be expected to affect Arctic stratification in the coming years. These include increasing freshwater input from runoff, precipitation and melting sea ice; changes to the ocean circulation resulting from the changing freshwater balance; increase in ocean heat flux from the Atlantic; and reduction in sea ice cover and consequent changes in transfer of momentum from the atmosphere to the ocean and exposure of the sea surface to ocean:atmosphere heat fluxes. All of these have received attention to a greater or lesser extent individually in the literature, but the studies we present here indicate that the interactions between them are complex and a more integrated understanding of their likely effects is required.

Bibliography

Y. Aksenov, S. Bacon, A. C. Coward, and A. J. G. Nurser. The North Atlantic inflow to the Arctic Ocean: High-resolution model study. *Journal of Marine Systems*, 79 (1-2):1–22, 2010. ISSN 0924-7963.

Y. Aksenov, V. V. Ivanov, A. J. G. Nurser, S. Bacon, I. V. Polyakov, A. C. Coward, A. C. Naveira Garabato, and A. Beszczynska-Moeller. The Arctic Circumpolar Boundary Current. *Journal of Geophysical Research: Oceans*, 116(C9):C09017, 2011. ISSN 2156-2202.

M. Arthun, R. B. Ingvaldsen, L. H. Smedsrud, and C. Schrum. Dense water formation and circulation in the Barents Sea. *Deep-Sea Research Part I-Oceanographic Research Papers*, 58(8):801–817, 2011. ISSN 0967-0637.

A. Beszczynska-Möller, R. A. Woodgate, C. Lee, H. Melling, and M. Karcher. A synthesis of exchanges through the main oceanic gateways to the Arctic Ocean. *Oceanography*, 24(3):82–99, 2011. ISSN 1042-8275.

R. Bintanja and F. M. Selten. Future increases in Arctic precipitation linked to local evaporation and sea-ice retreat. *Nature*, 509(7501):479–+, 2014. ISSN 0028-0836.

R. H. Bourke, A. M. Weigel, and R. G. Paquette. The westward turning branch of the West Spitsbergen Current. *Journal of Geophysical Research-Oceans*, 93(C11): 14065–14077, 1988.

E. C. Carmack. The alpha/beta ocean distinction: A perspective on freshwater fluxes, convection, nutrients and productivity in high-latitude seas. *Deep-Sea Research Part Ii-Topical Studies in Oceanography*, 54(23-26):2578–2598, 2007. ISSN 0967-0645.

J. C. Comiso. Large decadal decline of the Arctic multiyear ice cover. *Journal of Climate*, 25(4):1176–1193, 2011. ISSN 0894-8755.

K. Cowtan and R. G. Way. Coverage bias in the HadCRUT4 temperature series and its impact on recent temperature trends. *Quarterly Journal of the Royal Meteorological Society*, 140(683):1935–1944, 2014. ISSN 0035-9009.

E. A. d'Asaro and J. H. Morison. Internal waves and mixing in the Arctic Ocean. *Deep-Sea Research Part A: Oceanographic Research Papers*, 39(2a):S459–S484, 1992. ISSN 0198-0149.

C. de Lavergne, G. Madec, J. Le Sommer, A. J. G. Nurser, and A. C. N. Garabato. The impact of a variable mixing efficiency on the abyssal overturning. *Journal of Physical Oceanography*, 46(2):663–681, 2016. ISSN 0022-3670.

S. Dewey, J. Morison, R. Kwok, S. Dickinson, D. Morison, and R. Andersen. Arctic ice-ocean coupling and gyre equilibration observed with remote sensing. *Geophysical Research Letters*, 45(3):1499–1508, 2018. ISSN 0094-8276.

G. D. Egbert and S. Y. Erofeeva. Efficient inverse modeling of barotropic ocean tides. *Journal of Atmospheric and Oceanic Technology*, 19(2):183–204, 2002. ISSN 0739-0572.

G. D. Egbert and R. D. Ray. Estimates of M-2 tidal energy dissipation from TOPEX/ Poseidon altimeter data. *Journal of Geophysical Research-Oceans*, 106(C10): 22475–22502, 2001. ISSN 2169-9275.

T. Eldevik and J. E. O. Nilsen. The Arctic-Atlantic thermohaline circulation. *Journal of Climate*, 26(21):8698–8705, 2013. ISSN 0894-8755.

E. Fahrbach, J. Meincke, S. Osterhus, G. Rohardt, U. Schauer, V. Tverberg, and J. Verduin. Direct measurements of volume transports through Fram Strait. *Polar Research*, 20(2):217–224, 2001. ISSN 0800-0395.

I. Fer, M. Muller, and A. K. Peterson. Tidal forcing, energetics, and mixing near the Yermak Plateau. *Ocean Science*, 11(2):287–304, 2015. ISSN 1812-0784.

I. Fer, R. Skogseth, and F. Geyer. Internal waves and mixing in the marginal ice zone near the Yermak Plateau. *Journal of Physical Oceanography*, 40(7):1613–1630, 2010. ISSN 0022-3670.

K. A. Giles, S. W. Laxon, A. L. Ridout, D. J. Wingham, and S. Bacon. Western Arctic Ocean freshwater storage increased by wind-driven spin-up of the Beaufort Gyre. *Nature Geoscience*, 5(3):194–197, 2012. ISSN 1752-0894.

A. E. Gill. *Atmosphere-Ocean Dynamics*. Academic Press, 1982. ISBN 9780122835223.

S. M. Griffies, A. Biastoch, C. Boning, F. Bryan, G. Danabasoglu, E. P. Chassignet, M. H. England, R. Gerdes, H. Haak, R. W. Hallberg, W. Hazeleger, J. Jungclaus, W. G. Large, G. Madec, A. Pirani, B. L. Samuels, M. Scheinert, A. Sen Gupta, C. A. Severijns, H. L. Simmons, A. M. Treguier, M. Winton, S. Yeager, and J. J. Yin. Coordinated Ocean-Ice Reference Experiments (COREs). *Ocean Modelling*, 26 (1-2):1–46, 2009. ISSN 1463-5003.

J. D. Guthrie, I. Fer, and J. H. Morison. Thermohaline staircases in the Amundsen Basin: Possible disruption by shear and mixing. *Journal of Geophysical Research-Oceans*, 122(10):7767–7782, 2017. ISSN 2169-9275.

J. D. Guthrie, J. H. Morison, and I. Fer. Revisiting internal waves and mixing in the Arctic Ocean. *Journal of Geophysical Research-Oceans*, 118(8):3966–3977, 2013. ISSN 2169-9275.

T. W. N. Haine, B. Curry, R. Gerdes, E. Hansen, M. Karcher, C. Lee, B. Rudels, G. Spreen, L. de Steur, K. D. Stewart, and R. Woodgate. Arctic freshwater export: Status, mechanisms, and prospects. *Global and Planetary Change*, 125:13–35, 2015. ISSN 0921-8181.

I. M. Held and B. J. Soden. Robust responses of the hydrological cycle to global warming. *Journal of Climate*, 19(21):5686–5699, 2006. ISSN 0894-8755.

M. M. Holland, J. Finnis, A. P. Barrett, and M. C. Serreze. Projected changes in Arctic Ocean freshwater budgets. *Journal of Geophysical Research-Biogeosciences*, 112(G4), 2007. ISSN 2169-8953.

T. N. Huussen, A. C. Naveira Garabato, H. L. Bryden, and E. L. McDonagh. Is the deep Indian Ocean MOC sustained by breaking internal waves? *Journal of Geophysical Research-Oceans*, 117, 2012. ISSN 0148-0227.

P. E. Isachsen, C. Mauritzen, and H. Svendsen. Dense water formation in the Nordic Seas diagnosed from sea surface buoyancy fluxes. *Deep-Sea Research Part I-Oceanographic Research Papers*, 54(1):22–41, 2007. ISSN 0967-0637.

A. Jahn, L. B. Tremblay, R. Newton, M. M. Holland, L. A. Mysak, and I. A. Dmitrenko. A tracer study of the Arctic Ocean's liquid freshwater export variability. *Journal of Geophysical Research-Oceans*, 115, 2010. ISSN 0148-0227.

M. Jakobsson. Hypsometry and volume of the Arctic Ocean and its constituent seas. *Geochemistry Geophysics Geosystems*, 3, 2002. ISSN 1525-2027.

H. L. Johnson, S. B. Cornish, Y. Kostov, E. Beer, and C. Lique. Arctic Ocean freshwater content and its decadal memory of sea-level pressure. *Geophysical Research Letters*, 45(10):4991–5001, 2018. ISSN 0094-8276.

L. Jullion, K. J. Heywood, A. C. N. Garabato, and D. P. Stevens. Circulation and water mass modification in the Brazil-Malvinas Confluence. *Journal of Physical Oceanography*, 40(5):845–864, 2010. ISSN 0022-3670.

V. M. Kattsov and J. E. Walsh. Twentieth-century trends of Arctic precipitation from observational data and a climate model simulation. *Journal of Climate*, 13(8): 1362–1370, 2000. ISSN 0894-8755.

V. M. Kattsov, J. E. Walsh, W. L. Chapman, V. A. Govorkova, T. V. Pavlova, and X. D. Zhang. Simulation and projection of Arctic freshwater budget components by the IPCC AR4 global climate models. *Journal of Hydrometeorology*, 8(3):571–589, 2007. ISSN 1525-755x.

R. Kwok, G. F. Cunningham, M. Wensnahan, I. Rigor, H. J. Zwally, and D. Yi. Thinning and volume loss of the Arctic Ocean sea ice cover: 2003-2008. *Journal of Geophysical Research-Oceans*, 114, 2009. ISSN 2169-9275.

E. Lambert, T. Eldevik, and P. M. Haugan. How northern freshwater input can stabilise thermohaline circulation. *Tellus Series A-Dynamic Meteorology and Oceanography*, 68, 2016. ISSN 1600-0870.

Y. D. Lenn, T. P. Rippeth, C. P. Old, S. Bacon, I. Polyakov, V. Ivanov, and J. Holemann. Intermittent intense turbulent mixing under ice in the Laptev Sea continental shelf. *Journal of Physical Oceanography*, 41(3):531–547, 2011. ISSN 0022-3670.

Y. D. Lenn, P. J. Wiles, S. Torres-Valdes, E. P. Abrahamsen, T. P. Rippeth, J. H. Simpson, S. Bacon, S. W. Laxon, I. Polyakov, V. Ivanov, and S. Kirillov. Vertical mixing at intermediate depths in the Arctic boundary current. *Geophysical Research Letters*, 36, 2009. ISSN 0094-8276.

B. Lincoln, T. P. Rippeth, Y. D. Lenn, M. L. Timmermans, W. J. Williams, and S. Bacon. Wind-driven mixing at intermediate depths in an ice-free Arctic Ocean. *Geophysical Research Letters*, 43(18):9749–9756, 2016. ISSN 0094-8276.

R. Lindsay, M. Wensnahan, A. Schweiger, and J. Zhang. Evaluation of seven different atmospheric reanalysis products in the Arctic. *Journal of Climate*, 27(7):2588–2606, 2014. ISSN 0894-8755.

G. A. MacGilchrist, A. C. Naveira Garabato, T. Tsubouchi, S. Bacon, S. Torres-Valdes, and K. Azetsu-Scott. The Arctic Ocean carbon sink. *Deep-Sea Research Part I-Oceanographic Research Papers*, 86:39–55, 2014. ISSN 0967-0637.

G. E. Manucharyan and M. A. Spall. Wind-driven freshwater buildup and release in the Beaufort Gyre constrained by mesoscale eddies. *Geophysical Research Letters*, 43 (1):273–282, 2016. ISSN 0094-8276.

R. Marsh. Cabbeling due to isopycnal mixing in isopycnic coordinate models. *Journal of Physical Oceanography*, 30(7):1757–1775, 2000. ISSN 0022-3670.

J. Marshall, J. Scott, and A. Proshutinsky. "Climate response functions" for the Arctic Ocean: a proposed coordinated modelling experiment. *Geoscientific Model Development*, 10(7):2833–2848, 2017. ISSN 1991-959x.

C. Mauritzen. Production of dense overflow waters feeding the North Atlantic across the Greenland-Scotland Ridge. Part 1. Evidence for a revised circulation scheme. *Deep-Sea Research Part I-Oceanographic Research Papers*, 43(6):769–806, 1996. ISSN 0967-0637.

G. Meneghello, J. Marshall, S. T. Cole, and M. L. Timmermans. Observational inferences of lateral eddy diffusivity in the halocline of the Beaufort Gyre. *Geophysical Research Letters*, 44(24):12331–12338, 2017. ISSN 0094-8276.

J. Morison, R. Kwok, C. Peralta-Ferriz, M. Alkire, I. Rigor, R. Andersen, and M. Steele. Changing Arctic Ocean freshwater pathways. *Nature*, 481(7379):66–70, 2012. ISSN 0028-0836.

A. T. Nguyen, D. Menemenlis, and R. Kwok. Arctic ice-ocean simulation with optimized model parameters: Approach and assessment. *Journal of Geophysical Research-Oceans*, 116, 2011. ISSN 2169-9275.

J. Nilsson and G. Walin. Salinity-dominated thermohaline circulation in sill basins: can two stable equilibria exist? *Tellus Series a-Dynamic Meteorology and Oceanography*, 62(2):123–133, 2010. ISSN 0280-6495.

D. Notz. The future of ice sheets and sea ice: Between reversible retreat and unstoppable loss. *Proceedings of the National Academy of Sciences of the United States of America*, 106(49):20590–20595, 2009. ISSN 0027-8424.

A. Nummelin, M. Ilicak, C. Li, and L. H. Smedsrud. Consequences of future increased Arctic runoff on Arctic Ocean stratification, circulation, and sea ice cover. *Journal of Geophysical Research-Oceans*, 121(1):617–637, 2016. ISSN 2169-9275.

A. J. G. Nurser and S. Bacon. The Rossby radius in the Arctic Ocean. *Ocean Science*, 10(6):967–975, 2014. ISSN 1812-0784.

K. Onogi, J. Tslttsui, H. Koide, M. Sakamoto, S. Kobayashi, H. Hatsushika, T. Matsumoto, N. Yamazaki, H. Kaalhori, K. Takahashi, S. Kadokura, K. Wada, K. Kato, R. Oyama, T. Ose, N. Mannoji, and R. Taira. The JRA-25 reanalysis. *Journal of the Meteorological Society of Japan*, 85(3):369–432, 2007. ISSN 0026-1165.

L. Padman and T. M. Dillon. Turbulent mixing near the Yermak Plateau during the Coordinated Eastern Arctic Experiment. *Journal of Geophysical Research-Oceans*, 96(C3):4769–4782, 1991. ISSN 0148-0227.

L. Padman and S. Erofeeva. A barotropic inverse tidal model for the Arctic Ocean. *Geophysical Research Letters*, 31(2), 2004. ISSN 0094-8276.

L. Padman, A. J. Plueddemann, R. D. Muench, and R. Pinkel. Diurnal tides near the Yermak Plateau. *Journal of Geophysical Research-Oceans*, 97(C8):12639–12652, 1992. ISSN 2169-9275.

V. Pavlov, O. Pavlova, and R. Korsnes. Sea ice fluxes and drift trajectories from potential pollution sources, computed with a statistical sea ice model of the Arctic Ocean. *Journal of Marine Systems*, 48(1-4):133–157, 2004. ISSN 0924-7963.

P. Pemberton and J. Nilsson. The response of the central Arctic Ocean stratification to freshwater perturbations. *Journal of Geophysical Research-Oceans*, 121(1): 792–817, 2016. ISSN 2169-9275.

P. Pemberton, J. Nilsson, M. Hieronymus, and H. E. M. Meier. Arctic Ocean water mass transformation in S-T coordinates. *Journal of Physical Oceanography*, 45(4): 1025–1050, 2015. ISSN 0022-3670.

P. Pemberton, J. Nilsson, and H. E. M. Meier. Arctic Ocean freshwater composition, pathways and transformations from a passive tracer simulation. *Tellus Series a-Dynamic Meteorology and Oceanography*, 66, 2014. ISSN 0280-6495.

I. V. Polyakov, V. A. Alexeev, G. I. Belchansky, I. A. Dmitrenko, V. V. Ivanov, S. A. Kirillov, A. A. Korablev, M. Steele, L. A. Timokhov, and I. Yashayaev. Arctic Ocean freshwater changes over the past 100 years and their causes. *Journal of Climate*, 21(2):364–384, 2008. ISSN 0894-8755.

I. V. Polyakov, L. Padman, Y. D. Lenn, A. Pnyushkov, R. Rember, and V. V. Ivanov. Eastern Arctic Ocean diapycnal heat fluxes through large double-diffusive steps. *Journal of Physical Oceanography*, 49(1):227–246, 2019. ISSN 0022-3670.

I. V. Polyakov, A. V. Pnyushkov, M. B. Alkire, I. M. Ashik, T. M. Baumann, E. C. Carmack, I. Goszczko, J. Guthrie, V. V. Ivanov, T. Kanzow, R. Krishfield, R. Kwok, A. Sundfjord, J. Morison, R. Rember, and A. Yulin. Greater role for Atlantic inflows on sea-ice loss in the Eurasian Basin of the Arctic Ocean. *Science*, 356(6335): 285–291, 2017. ISSN 0036-8075.

A. Proshutinsky, R. Krishfield, M. L. Timmermans, J. Toole, E. Carmack, F. McLaughlin, W. J. Williams, S. Zimmermann, M. Itoh, and K. Shimada. Beaufort Gyre freshwater reservoir: State and variability from observations. *Journal of Geophysical Research-Oceans*, 114, 2009. ISSN 2169-9275.

L. Rainville and P. Winsor. Mixing across the Arctic Ocean: Microstructure observations during the Beringia 2005 expedition. *Geophysical Research Letters*, 35 (8), 2008. ISSN 0094-8276.

L. Rainville and R. A. Woodgate. Observations of internal wave generation in the seasonally ice-free Arctic. *Geophysical Research Letters*, 36, 2009. ISSN 0094-8276.

A. Randelhoff, I. Fer, and A. Sundfjord. Turbulent upper-ocean mixing affected by meltwater layers during Arctic summer. *Journal of Physical Oceanography*, 47(4): 835–853, 2017. ISSN 0022-3670.

T. P. Rippeth, B. J. Lincoln, Y. D. Lenn, J. A. M. Green, A. Sundfjord, and S. Bacon. Tide-mediated warming of Arctic halocline by Atlantic heat fluxes over rough topography. *Nature Geoscience*, 8(3):191–194, 2015. ISSN 1752-0894.

T. P. Rippeth, V. Vlasenko, N. Stashchuk, B. D. Scannell, J. A. M. Green, B. J. Lincoln, and S. Bacon. Tidal conversion and mixing poleward of the critical latitude (an Arctic case study). *Geophysical Research Letters*, 44(24):12349–12357, 2017. ISSN 0094-8276.

B. Rudels. Constraints on exchanges in the Arctic mediterranean - do they exist and can they be of use? *Tellus Series A - Dynamic Meteorology and Oceanography*, 62 (2):109–122, 2010. ISSN 0280-6495.

B. Rudels. Arctic Ocean stability: The effects of local cooling, oceanic heat transport, freshwater input, and sea ice melt with special emphasis on the Nansen Basin. *Journal of Geophysical Research-Oceans*, 121(7):4450–4473, 2016. ISSN 2169-9275.

B. Rudels and H. J. Friedrich. The transformations of Atlantic Water in the Arctic Ocean and their significance for the freshwater budget. *Freshwater Budget of the Arctic Ocean*, 70:503–532, 2000.

B. Rudels, H. J. Friedrich, and D. Quadfasel. The Arctic Circumpolar Boundary Current. *Deep-Sea Research Part Ii-Topical Studies in Oceanography*, 46(6-7): 1023–1062, 1999. ISSN 0967-0645.

B. Rudels, E. P. Jones, U. Schauer, and P. Eriksson. Atlantic sources of the Arctic Ocean surface and halocline waters. *Polar Research*, 23(2):181–208, 2004. ISSN 0800-0395.

B. Rudels, N. Kuzmina, U. Schauer, T. Stipa, and V. Zhurbas. Double-diffusive convection and interleaving in the Arctic Ocean - distribution and importance. *Geophysica*, 45(1-2):199–213, 2009.

B. Rudels, U. Schauer, G. Bjork, M. Korhonen, S. Pisarev, B. Rabe, and A. Wisotzki. Observations of water masses and circulation with focus on the Eurasian Basin of the Arctic Ocean from the 1990s to the late 2000s. *Ocean Science*, 9(1):147–169, 2013. ISSN 1812-0784.

L. H. Smedsrud, R. Ingvaldsen, J. E. O. Nilsen, and O. Skagseth. Heat in the Barents Sea: transport, storage, and surface fluxes. *Ocean Science*, 6(1):219–234, 2010. ISSN 1812-0784.

M. A. Spall. On the circulation of Atlantic Water in the Arctic Ocean. *Journal of Physical Oceanography*, 43(11):2352–2371, 2013. ISSN 0022-3670.

G. Spreen, S. Kern, D. Stammer, and E. Hansen. Fram Strait sea ice volume export estimated between 2003 and 2008 from satellite data. *Geophysical Research Letters*, 36, 2009. ISSN 0094-8276.

L. St. Laurent and H. Simmons. Estimates of power consumed by mixing in the ocean interior. *Journal of Climate*, 19(19):4877–4890, 2006. ISSN 0894-8755.

L. C. St. Laurent, H. L. Simmons, and S. R. Jayne. Estimating tidally driven mixing in the deep ocean. *Geophysical Research Letters*, 29(23), 2002. ISSN 0094-8276.

L. C. St. Laurent, J. M. Toole, and R. W. Schmitt. Buoyancy forcing by turbulence above rough topography in the abyssal Brazil Basin. *Journal of Physical Oceanography*, 31(12):3476–3495, 2001. ISSN 0022-3670.

M. Steele, R. Morley, and W. Ermold. PHC: A global ocean hydrography with a high-quality Arctic Ocean. *Journal of Climate*, 14(9):2079–2087, 2001. ISSN 0894-8755.

A. Stigebrandt. A model for the thickness and salinity of the upper layer in the Arctic Ocean and the relationship between the ice thickness and some external parameters. *Journal of Physical Oceanography*, 11(10):1407–1422, 1981. ISSN 0022-3670.

A. Stigebrandt. On the hydrographic and ice conditions in the northern North-Atlantic during different phases of a glaciation cycle. *Palaeogeography, Palaeoclimatology, Palaeoecology*, 50(2-3):303–321, 1985. ISSN 0031-0182.

D. W. J. Thompson and J. M. Wallace. The Arctic Oscillation signature in the wintertime geopotential height and temperature fields. *Geophysical Research Letters*, 25(9):1297–1300, 1998. ISSN 0094-8276.

K. M. Thyng, C. A. Greene, R. D. Hetland, H. M. Zimmerle, and S. F. DiMarco. True colors of oceanography: Guidelines for effective and accurate colormap selection. *Oceanography*, 29(3):9–13, 2016. ISSN 1042-8275.

M. L. Timmermans and C. Garrett. Evolution of the deep water in the Canadian Basin in the Arctic Ocean. *Journal of Physical Oceanography*, 36(5):866–874, 2006. ISSN 0022-3670.

M. L. Timmermans, A. Proshutinsky, E. Golubeva, J. M. Jackson, R. Krishfield, M. McCall, G. Platov, J. Toole, W. Williams, T. Kikuchi, and S. Nishino. Mechanisms of Pacific Summer Water variability in the Arctic's central Canada Basin. *Journal of Geophysical Research-Oceans*, 119(11):7523–7548, 2014. ISSN 2169-9275.

M. L. Timmermans, J. Toole, R. Krishfield, and P. Winsor. Ice-tethered profiler observations of the double-diffusive staircase in the Canada Basin thermocline. *Journal of Geophysical Research-Oceans*, 113, 2008. ISSN 2169-9275.

S. Torres-Valdes, T. Tsubouchi, S. Bacon, A. C. Naveira Garabato, R. Sanders, F. A. McLaughlin, B. Petrie, G. Kattner, K. Azetsu-Scott, and T. E. Whitledge. Export

of nutrients from the Arctic Ocean. *Journal of Geophysical Research-Oceans*, 118(4): 1625–1644, 2013. ISSN 2169-9275.

S. Torres-Valdes, T. Tsubouchi, E. Davey, I. Yashayaev, and S. Bacon. Relevance of dissolved organic nutrients for the Arctic Ocean nutrient budget. *Geophysical Research Letters*, 43(12):6418–6426, 2016. ISSN 0094-8276.

T. Tsubouchi, S. Bacon, Y. Aksenov, A. C. Naveira Garabato, A. Beszczynska-Moller, E. Hansen, L. de Steur, B. Curry, and C. M. Lee. The Arctic Ocean seasonal cycles of heat and freshwater fluxes: Observation-based inverse estimates. *Journal of Physical Oceanography*, 48(9):2029–2055, 2018. ISSN 0022-3670.

T. Tsubouchi, S. Bacon, A. C. N. Garabato, Y. Aksenov, S. W. Laxon, E. Fahrbach, A. Beszczynska-Moller, E. Hansen, C. M. Lee, and R. B. Ingvaldsen. The Arctic Ocean in summer: A quasi-synoptic inverse estimate of boundary fluxes and water mass transformation. *Journal of Geophysical Research-Oceans*, 117:28, 2012. ISSN 2169-9275.

J. S. Turner. The melting of ice in the Arctic Ocean: The influence of double-diffusive transport of heat from below. *Journal of Physical Oceanography*, 40(1):249–256, 2010. ISSN 0022-3670.

S. J. Vavrus, M. M. Holland, A. Jahn, D. A. Bailey, and B. A. Blazey. Twenty-first-century Arctic climate change in CCSM4. *Journal of Climate*, 25(8): 2696–2710, 2012. ISSN 0894-8755.

W. J. von Appen, U. Schauer, T. Hattermann, and A. Beszczynska-Moller. Seasonal cycle of mesoscale instability of the West Spitsbergen Current. *Journal of Physical Oceanography*, 46(4):1231–1254, 2016. ISSN 0022-3670.

G. Walin. On the relation between sea-surface heat-flow and thermal circulation in the ocean. *Tellus*, 34(2):187–195, 1982. ISSN 0040-2826.

W. Werenskiold. Coastal currents. *Geofysiske Publikasjoner*, 10(13), 1935.

R. A. Woodgate, K. Aagaard, J. H. Swift, K. K. Falkner, and W. M. Smethie. Pacific ventilation of the Arctic Ocean's lower halocline by upwelling and diapycnal mixing over the continental margin. *Geophysical Research Letters*, 32(18), 2005. ISSN 0094-8276.

Q. Yang, T. H. Dixon, P. G. Myers, J. Bonin, D. Chambers, M. R. van den Broeke, M. H. Ribergaard, and J. Mortensen. Recent increases in Arctic freshwater flux affects Labrador Sea convection and Atlantic overturning circulation. *Nature Communications*, 7, 2016. ISSN 2041-1723.

J. L. Zhang and D. A. Rothrock. Modeling global sea ice with a thickness and enthalpy distribution model in generalized curvilinear coordinates. *Monthly Weather Review*, 131(5):845–861, 2003. ISSN 0027-0644.

M. N. Zhao, M. L. Timmermans, S. Cole, R. Krishfield, A. Proshutinsky, and J. Toole. Characterizing the eddy field in the Arctic Ocean halocline. *Journal of Geophysical Research-Oceans*, 119(12):8800–8817, 2014. ISSN 2169-9275.